Sensing, Modeling, Control and Evaluation of Soft Robots for Wearable Applications

by

Emiliano Quiñones Yumbla

A Dissertation Presented in Partial Fulfillment
of the Requirements for the Degree
Doctor of Philosophy

Approved July 2023 by the
Graduate Supervisory Committee:

Wenlong Zhang, Chair
Spring Berman
Hyunglae Lee
Hamid Marvi
Thomas Sugar

ARIZONA STATE UNIVERSITY

August 2023

ABSTRACT

While wearable soft robots have successfully addressed many inherent design limitations faced by wearable rigid robots, they possess a unique set of challenges due to their soft and compliant nature. Some of these challenges are present in the sensing, modeling, control and evaluation of wearable soft robots. Machine learning algorithms have shown promising results for sensor fusion with wearable robots, however, they require extensive data to train models for different users and experimental conditions. Modeling soft sensors and actuators require characterizing non-linearity and hysteresis, which complicates deriving an analytical model. Experimental characterization can capture the characteristics of non-linearity and hysteresis but requires developing a synthesized model for real-time control. Controllers for wearable soft robots must be robust to compensate for unknown disturbances that arise from the soft robot and its interaction with the user. Since developing dynamic models for soft robots is complex, inaccuracies that arise from the unmodeled dynamics lead to significant disturbances that the controller needs to compensate for. In addition, obtaining a physical model of the human-robot interaction is complex due to unknown human dynamics during walking. Finally, the performance of soft robots for wearable applications requires extensive experimental evaluation to analyze the benefits for the user.

To address these challenges, this dissertation focuses on the sensing, modeling, control and evaluation of soft robots for wearable applications. A model-based sensor fusion algorithm is proposed to improve the estimation of human joint kinematics, with a soft flexible robot that requires compact and lightweight sensors. To overcome limitations with rigid sensors, an inflatable soft haptic sensor is developed to enable gait sensing and haptic feedback. Through experimental characterization, a mathematical

model is derived to quantify the user's ground reaction forces and the delivered haptic force. Lastly, the performance of a wearable soft exosuit in assisting human users during lifting tasks is evaluated, and the benefits obtained from the soft robot assistance are analyzed.

Para mi madre, Gerardina, mi padre, Rey, mi hermano, Camilo y mi novia, Yocasta, les dedico este trabajo, porque ustedes son mi mayor motivación para haberme embarcado en esta hazaña. Todos ustedes son mi mayor fuente de inspiración como modelo de personas y profesionales.

ACKNOWLEDGMENTS

I would like to express my deepest gratitude to my Research Advisor, Dr. Wenlong Zhang, for his guidance and invaluable insight throughout my research journey. I am thankful to my Graduate Committee members, Dr. Spring Berman, Dr. Hyunglae Lee, Dr. Hamid Marvi, and Dr. Thomas Sugar, for their constructive feedback and support. I am also indebted to Dr. Daniel Aukes, Dr. Panagiotis Artemiadis, and Dr. Jennie Si, who served as research mentors and provided valuable guidance during various research projects.

My heartfelt appreciation goes to the members of the RISE Lab and the IDEA Lab for their endless support and collaborative spirit. Their insightful conversations and technical expertise were instrumental in resolving numerous challenges and brainstorming innovative research ideas. I would like to extend special acknowledgment to Zhi Qiao, Karishma Patnaik, Saivimal Sridar, Dongting Li, Jahnav Rokalaboina, Weijia Tao, Ibrahim Hasan, Tolemy Nibi, Yousef Soltanian, and Junmin Zhong, who closely collaborated with me and contributed significantly to our shared accomplishments.

I am profoundly grateful to my family and friends, whose support sustained me throughout this arduous journey. I dedicate this work to my mother, Gerardina Yumbla and my father, Rey Quiñones, who have been my constant source of inspiration to pursue education and research.

To my beloved Yocasta Lopez, I offer my most profound gratitude for creating a warm and loving home that reminded me of the importance of cherishing life's joys. Your support, companionship, and love have been a source of immense strength. I will forever be grateful for your understanding and for sharing both the struggles

and triumphs of my academic pursuits. Words can never express the depth of my gratitude for accompanying me on this journey.

Lastly, I would like to extend my heartfelt appreciation to my feline companions, Ares and Draco. Their presence during late-night work sessions and their interest in reviewing my manuscripts brought a sense of comfort and companionship to my solitary endeavors.

TABLE OF CONTENTS

CHAPTER Page

LIST OF TABLES

LIST OF FIGURES

Figure Page

Chapter 1

INTRODUCTION

Over the past decades, research and development of robot technology have been on the rise, allowing it to become more common and widely available. Consequently, there has been an increasing interest in wearable technology with even multiple devices becoming commercially available. Wearable robots have been studied over several decades for rehabilitation and physical therapy, mobility assistance and sports training. Traditional wearable robots consist of rigid links, motors and transmissions that can be worn by a human user and allow assisting motion, also known as exoskeletons. While exoskeleton applications have demonstrated promising results, they still possess challenges and limitations for daily use applications. Some inherent limitations of exoskeletons are mainly contributed to the heavy and rigid nature of the materials and components, which pose as a load burden for the user and a risk to safety. As such, there has been a growing interest, research and development in using soft, compliant and lightweight materials for wearable robots. This has led to the development of a new type of wearable technology that uses soft robotics to address these challenges, also known as exosuits.

Wearable soft robots consist of lightweight, soft and compliant materials for the design of actuators and the interface with the human user. While wearable soft robots have successfully addressed some inherent design limitations faced by rigid wearable robots, they possess a unique set of challenges due to their soft and compliant nature. Some of these challenges are present in the sensing, modeling, control and evaluation of wearable soft robots.

Sensing in wearable soft robotics deals with the design of sensors and fusion algorithms that utilize sensors that are compatible with the human and the soft robot, both of which limit the implementation of more common sensors used in traditional rigid robots, such as joint encoders and strain gauges. Modeling and characterization of soft robots face the challenges of developing representational models that deal with complex actuation and non-linear systems, such as fluidic, pneumatic and cable-driven systems. Control and evaluation of soft exosuits require investigating the effects of wearable soft robots on humans and evaluating what are the most appropriate control strategies that maximize the benefit obtained.

To address these challenges, this dissertation will introduce the sensing, modeling, control and evaluation of soft robots for wearable applications. This dissertation demonstrates how sensor fusion algorithms with compatible sensors for a soft flexible robot can improve estimation of human joint kinematics. A soft haptic sensor was developed and characterized to estimate the user's ground reaction forces and provide haptic feedback to the foot. Finally, we evaluate the performance of a wearable soft exosuit to assist the human user during lifting tasks and analyze the benefits obtained from the soft robot assistance.

1.1 Wearable Soft Robots

Wearable robots are advanced human symbiotic robotic systems characterized by suitable shape, kinematic, and weight factors to be worn on the human body with the function of either augmenting and assisting or restoring human limb function (Frisoli 2019; Pons 2008). Over the past decades, wearable robots have been applied to facilitate neuro-rehabilitation (Channa, Popescu, and Ciobanu 2020), prevent work-

related injuries (Theurel and Desbrosses 2019), enhance the performance of sports training (*Elevate Ski, Roam Robotics*), and augment human capabilities in labor-intensive tasks (B. Chen et al. 2016). For example, there are approximately 6.6 million stroke patients in the USA, and at least 65% of them suffer from gait impairment (Cirstea 2019). Wearable robotics provides a promising solution to meet this increased demand for physical therapy and enable in-home rehabilitation (Kubota et al. 2013).

Currently the actuators, sensors, transmission, and braces of wearable robots are mostly made of rigid materials. Rigid exoskeletons are often composed of heavy motors and bulky structures that could cause fatigue to the users and restrict their natural motions. Furthermore, rigid wearable robots require precise mounting and adjustment for users, and any misalignment with the human joint can jeopardize the robot's performance and even pose safety risks to the users (Zanotto et al. 2015).

To address these challenges, there has been a growing interest in introducing soft materials (e.g., silicone and textiles) into wearable sensors and actuators (Banerjee, Tse, and Ren 2018). Fluids, cables, and shape-memory-alloy actuators are among the most popular actuation mechanisms (Thalman and Artemiadis 2020; Lee et al. 2017). In the meantime, soft sensors have been designed to measure strains and curvatures of the soft robots using flexible electronics, liquid metals, optical fibers (Saggio et al. 2016; Chossat et al. 2013; Leal-Junior, Frizera, et al. 2018). Wearable soft robots have demonstrated many advantages over their rigid counterparts, as they are generally inexpensive to make, safe to use, lightweight, highly customizable, and able to generate versatile motion profiles (Agarwal et al. 2016). As a result, research in the field of wearable soft robotics has been fast expanding in the past decade and has become a highly prominent sub-topic in the wearable robotics field. Examining the quantity of

published research articles in the overall wearable robotics field reveals that 27% of them are about soft robots in 2010 and it increased to 41% in 2020.

Wearable soft robotics is a highly interdisciplinary research topic that requires the integration of knowledge from material science, solid and fluid mechanics, mechanical design and manufacturing, modeling and control, and human systems engineering, to name a few. Wearable soft robots have been integrated with human users as exosuits to assist various human joints (Alan T. Asbeck et al. 2014), robot manipulators to augment human capabilities (Nguyen, Mohd, et al. 2019), and haptic devices to provide cues and feedback to the users (Kanjanapas et al. 2019). While earlier work in wearable soft robots focused on identifying the appropriate materials and actuation mechanisms (El-Atab et al. 2020), a large number of recent research in wearable soft robots focus on integrating these robots with human users by developing novel soft sensors (Heikenfeld et al. 2018), designing autonomous control algorithms for the soft robots (Park, Jeong, and Park 2021), and conducting tests with healthy and impaired users (Alan T Asbeck et al. 2015; S. Sridar et al. 2020). A few wearable soft robots have been productized to make these new technologies available to the public (*HeroWear; Roam Robotics; ReStore, ReWalk Robotics*).

1.2 Sensing in Wearable Soft Robots

Sensing in wearable robotics is vital to obtain crucial information about the users, actuator states, and environments. Existing wearable sensors, such as inertial measurement units (IMU), goniometers, load cells, and strain gauges, have been integrated with rigid exoskeletons. However, these rigid sensors are often incompatible with soft robots as they compromise the inherent compliance and safety, and also lead

to misalignment. This motivates the design of soft and flexible sensors that can be seamlessly integrated with wearable soft robots. This section will discuss the recent development in wearable soft sensor design and fusion algorithms.

1.2.1 Design of Soft Sensors

The design of soft sensors aims to achieve the sensing capabilities found in biological systems (Qiu et al. 2020). Wearable soft sensors are capable of measuring strain, force, curvature, joint angle and a combination of these properties through multimodal sensing. An overview of soft sensor designs can be observed in Fig. 1.1.

Strain sensing: Common principles employed to measure strain include liquid eutectic gallium–indium (eGaIn) (Yong-Lae Park, Bor-Rong Chen, and Wood 2012), biphasic gallium-indium alloy (bGaIn) (Liu, Shah, and Kramer-Bottiglio 2021), aqueous ionic solution (Chossat et al. 2013), ionic conductive liquid (Chossat et al. 2015; Frutiger et al. 2015), capacitive sensing (Atalay, Atalay, Gafford, et al. 2017) and polymer optical fiber (POF) threads (Harnett, Zhao, and Shepherd 2017). Soft strain

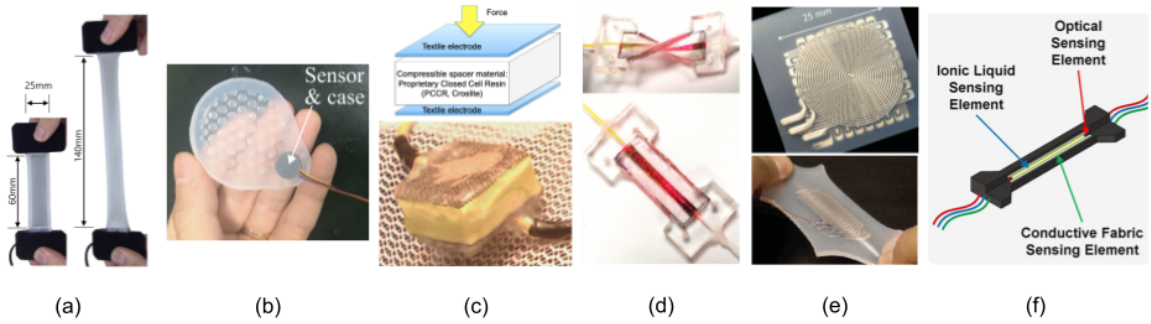

Figure 1.1. Examples of wearable soft sensor designs: (a) eGaIn strain sensor (Kim, Kwon, et al. 2019). (b) Pneumatic force sensor (Kim, Shin, and Kong 2018). (c) Conductive textile capacitive force sensor (Holleczek et al. 2010. (d) Polymer optical fiber strain and pressure sensor (To et al. 2018). (e) eGaIn multimode strain and force sensor (Yong-Lae Park, Bor-Rong Chen, and Wood 2012). (f) Multimode multifunctional sensor consisting of ionic liquid, conductive fabric and an optical element for bend, force and strain sensing (T. Kim et al. 2020).

sensors commonly consist of a conductive material incorporated into stretchable supporting materials such as silicone elastomers (Souri et al. 2020). The conductive filling serves as the active sensing material that responds to the strain of the encasing. When the microchannels filled with liquid conductive materials are deformed by stretching, the electrical resistance of the microchannels increases due to reduced cross-sectional area, increased channel length, or both (Chossat et al. 2013; Yong-Lae Park, Bor-Rong Chen, and Wood 2012; Chossat et al. 2015). Recently, bGaIn was developed with improved stable conductivity over large strains and extreme stretchability, compared to the commonly used eGaIn (Liu, Shah, and Kramer-Bottiglio 2021).

Sensing strain with soft capacitive sensors is usually achieved by stacking flat or concentric layers of conductive plates with inter-layers of silicone elastomer, such that when undergoing strain the distance between the conductive plates changes and induces a change in the capacitance measurement (Frutiger et al. 2015; Atalay, Atalay, Gafford, et al. 2017). The conductive layers can be composed of ionically conductive fluid (Frutiger et al. 2015) or solid metal plates such as aluminum and silver (Atalay, Atalay, Gafford, et al. 2017). In (Harnett, Zhao, and Shepherd 2017), the POF was utilized as a light-guiding thread for strain sensing. In POF strain sensors the intensity of the transmitted light drops along the length of the fiber. As the sensor is stretched the length of the sensor changes which induces a change in the light intensity.

Soft strain sensors usually demonstrate hyperelastic characteristics, with some studies reporting stretching twice their original length (Chossat et al. 2013). However, the viscoelasticity of the material has been shown to create hysteresis in dynamic stretching (D. Kim et al. 2020). Two independent studies reported a maximum hysteresis of 26.45% (Lu et al. 2019) and 21.34% (Russo et al. 2015) of the respective sensor measuring resistance. Furthermore, some have reported drift in the sensor

measurements over time and as a transient response to fixed strain conditions (Atalay, Atalay, Gafford, et al. 2017; D. Kim et al. 2020). Overall, capacitance strain sensors exhibit lower hysteresis and faster response times compared to resistance sensors (Souri et al. 2020; Atalay, Sanchez, et al. 2017).

Force sensing: To measure force, common mechanisms employed in soft sensors include pneumatic chambers (Kim, Shin, and Kong 2018), liquid eGaIn (Park et al. 2010; Vogt, Park, and Wood 2013), conductive textiles (Holleczek et al. 2010; Atalay et al. 2018), carbon fiber composite (Araromi, Walsh, and Wood 2017; Araromi et al. 2018), and POF (Leal-Junior, Frizera, et al. 2018). Pneumatic chamber soft sensors consist of sealed air-tight chambers that demonstrate a change in internal pressure to applied loads and are commonly manufactured from elastomeric materials or heat-sealable thermoplastic polyurethane (Kim, Shin, and Kong 2018), similar to Fig. 1.1b. In dynamic loading, the viscoelastic characteristics influence the measurements and cause hysteresis (Choi and Kong 2019), which implies that the dynamic characteristics of the air bladder cannot be neglected (Kyoungchul Kong and Tomizuka 2009). A hyperelastic pressure transducer was fabricated by embedding silicone rubber with microchannels of conductive liquid eGaIn (Park et al. 2010). Pressing the surface of the elastomer with pressure loads deforms the cross-section of the underlying channels and changes their electric resistance. Circular patterned microchannels with eGaIn allow sensing surface pressure and exhibit insensitiveness to strains along any axis (Yong-Lae Park, Bor-Rong Chen, and Wood 2012). Multi-axis force sensing was achieved in (Vogt, Park, and Wood 2013) by arranging three star-patterned microchannels filled with liquid eGaIn.

Force sensing with conductive fabrics is achieved by stacking two conductive layers with an inter-layer of a compressible spacer material such that when the sensor is

compressed the distance between the layers change and the capacitance measured between the conductive fabric also changes (Holleczek et al. 2010) (see Fig. 1.1c). Carbon fiber composites can be used as a conductive structure material that exhibits changes in electrical resistance when the structure geometry undergoes deformation. In (Araromi, Walsh, and Wood 2017), tensile loads of the sensor induce changes in electrical resistance between the carbon fiber composite structures as the layers of the U-shaped sensor design were deformed closer together or further apart. Multi-axis force sensing was performed with a set of carbon fiber composite conductors in the shape of a meander and positioned radially, such that forces on the sensor change the electrical resistance between the carbon fiber structures (Araromi et al. 2018). The POF was used in (Leal-Junior, Frizera, et al. 2018) for the detection of insole contact forces. When the POF sensor is pressed, the sensor bends and induces a variation in the refractive index due to the deformation of the fiber and stress-optic effect leading to a change in the light intensity (Leal-Junior, Frizera, et al. 2018).

Curvature and angle sensing: Common principles to measure curvature include resistive flex sensors (Saggio et al. 2016), liquid eGaIn (Majidi, Kramer, and Wood 2011; Kramer et al. 2011), and POF. Curvature resistive flex sensor designs consist of electrically conductive materials embedded within a flexible substrate (Saggio et al. 2016). When undergoing bending the substrate causes a mechanical stress of the conductive pattern that leads to a change in its electrical resistance. Curvature sensing with liquid eGaIn can be achieved by stacking two layers interconnected through the edges and a middle strut that induces compression loads on the liquid microchannel when the sensor is bent (Majidi, Kramer, and Wood 2011). Furthermore, when this design is embedded with a serpentine pattern microchannel simultaneous sensing of curvature and strain is possible (Kramer et al. 2011). Resistive flex sensors are

commercially available, although they exhibit drift in the sensor measurements over time, even in mechanically stationary conditions (Saggio et al. 2016).

Soft sensor designs employing wearable inductive coils (Mishra and Kiourti 2019), POF (Leal-Junior, Frizera, et al. 2018) and piezoresistive sensors (Sun et al. 2015) have shown the capability to measure the relative angle between segments. Wearable inductive coils were implemented in (Mishra and Kiourti 2019) to measure the relative angle between two segments. Relying on Faraday's Law of Induction, wearable wrap-around coils were designed to transmit and receive signals from one another through inductance. As the relative angle between the coils changes, the transmission coefficient will change due to the misalignment of the coils. This property allows for a sensing principle that directly reacts to the joint angle state. In (Sun et al. 2015), a piezoresistive hinge sensor was fabricated which during bending the carbon particles are pulled apart or closer changing the sensor's resistance. Inductance-based sensors have reported robustness to variation in human tissue dielectric properties (Mishra and Kiourti 2019) and immunity to electromagnetic interference (Sabri et al. 2015).

Multimodal sensing: Recent work has introduced single sensor designs to simultaneously sense multiple deformation modes (Yong-Lae Park, Bor-Rong Chen, and Wood 2012; T. Kim et al. 2020; Van Meerbeek, De Sa, and Shepherd 2018). An early work (Yong-Lae Park, Bor-Rong Chen, and Wood 2012) achieved sensing vertical force, and strain in two directions, by stacking two strain sensor layers and one force sensor layer with microchannels filled with liquid eGaIn (see Fig. 1.1e). A POF was used in (Van Meerbeek, De Sa, and Shepherd 2018) to measure twisting and bending. In (T. Kim et al. 2020) (Fig. 1.1f) ionic liquid, conductive fabric and optical sensing elements were integrated into a single sensor design to allow sensing and decoupling combined deformation modes of stretching, bending and compression.

1.2.2 Algorithms for Soft Sensor Fusion

Fusion algorithms in soft sensors allow compensating limitations in individual sensors and improve the overall measurement accuracy. Kalman Filter (KF) (Ponraj and Ren 2018; Tognetti et al. 2015; Leal-Junior, Vargas-Valencia, et al. 2018), Multiplicative Extended Kalman Filter (MEKF) Vargas-Valencia et al. 2021 and machine learning techniques (Kim, Kwon, et al. 2019; Jin et al. 2020; Tavassolian et al. 2020) have been implemented to fuse readings from soft sensors and other sensing approaches. In (Ponraj and Ren 2018), a KF was implemented to fuse soft resistive flex sensors with two infrared cameras to improve the accuracy and reliability of finger-tip position tracking when occlusion is encountered in the camera system. The KF was also implemented with soft resistance-based textiles (Tognetti et al. 2015) and POF curvature sensors (Leal-Junior, Vargas-Valencia, et al. 2018) for fusion with IMU data to improve knee joint angle estimation. This work was extended to quaternion-based MEKF, which showed further improved accuracy and repeatability for knee joint angle estimation in the sagittal plane (Vargas-Valencia et al. 2021). Compared to the KF, MEKF has demonstrated improved estimation results since it is applicable to non-linear dynamic systems. A limitation of both fusion methods in wearable applications is that obtaining a model of the human joint dynamics is often challenging.

To overcome this limitation, machine learning methods have been implemented to fuse sensor information without requiring a precise model of the human body dynamics (Kim, Kwon, et al. 2019; Jin et al. 2020; Tavassolian et al. 2020; Yang and Yin 2021). A long short-term memory (LSTM) model was employed in (Z. Chen et al. 2020) to fuse multiple soft strain sensors distributed through the human body

for the reconstruction of the 3D motion of the upper body. LSTM is a deep learning method effective for capturing long-term temporal dependencies (Greff et al. 2017). A semi-supervised deep learning architecture was proposed in (Kim, Kim, et al. 2019), consisting of a sequential encoder network, an alignment network, and a motion representation network, to estimate 3D position of the lower limb joints based on information from two soft strain sensors. Artificial Neural Networks (ANN) were employed in multimodal soft sensors to identify combined deformations of stretching, bending and compression (T. Kim et al. 2020). ANN (Prado et al. 2020), fuzzy logic (Kyoungchul Kong and Tomizuka 2009; González et al. 2015), and segmental regression approach based on a hidden logistic process (RHLP) (Mohammed et al. 2016) have been implemented to estimate the gait phases upon GCF measured from the soft force sensors.

Machine learning methods have demonstrated the successful fusion of different sensors without requiring knowledge of the sensor dynamics. However, they require a considerable amount of data to train the models. For example, 1000 cycles of sensor stretching were required to build the training data set for one sensor (Z. Chen et al. 2020). In many wearable applications, a machine learning model has to be retrained for each human subject since the anthropometric information significantly affects the training data. This can be inconvenient for the users. In addition, wearable soft sensors can slide over the human body with human movement, which may invalidate the learned model and require frequent modeling retraining.

1.3 Modeling and Characterization of Soft Sensors and Actuators

Modeling and characterization in wearable robotics are crucial for real-time robust control and estimation with soft robots and sensors. However, analytically deriving a dynamic model of inflatable soft robots and sensors is a complicated task due to complex geometrical deformations, material nonlinearities and hysteresis, and air compressibility (Xavier et al. 2022). In soft robots, softness is not concentrated at the joint level but instead, it is typically distributed across the complete structure, resulting in a continuously deformable structure (Della Santina, Duriez, and Rus 2023).

Although deriving an analytical model for soft robots and sensors is highly complex, several studies have successfully derived and validated analytical models under certain conditions and assumptions. For example, in (Nesler, Swift, and Rouse 2018) an analytical torque model of an inflatable actuator is derived. This model utilizes the geometry of the actuator and the internal pressure to estimate the torque generated. Since these models are based on the geometrical state of the actuator, the accuracy of the model ultimately depends on the manufacturing quality of the actuators. However, many soft actuators and sensors are hand manufactured and assembled (Nguyen and Zhang 2020), and the inherent imperfections of the process lead to a mismatch between the estimated and the actual geometry of the actuator. This ultimately complicates achieving precise torque control of such actuators, which is crucial for optimal control and estimation of assistive devices. In addition, typical analytical models do not capture some of the complex characteristics of soft actuators and sensors such as nonlinearities and hysteresis.

Finite Element Models (FEM) are a typical tool employed to derive an approximate

model of soft actuators and sensors. FEM has been successfully implemented to predict the kinematics and force output of fabric soft pneumatic actuators (Nguyen and Zhang 2020). However, the vast majority of FEM implementations employ quasi-static simulations with pressure changes being incremented in small time steps (Xavier et al. 2022). This leads to inaccuracies in dynamic applications, such as those involved with wearable assistive devices, in which the quasi-static assumption is no longer valid.

Mechanical characterization has been an alternative to analytical and computational models, given the advantage that this method directly collects the response of soft sensors and actuators. A clear advantage of mechanical characterization is that it captures the nonlinearities and hysteresis characteristics. Mechanical characterization has been employed to derive quasi-static models of torque for soft inflatable actuators (O'Neill et al. 2022). However, as with FEM, these quasi-static models become unreliable in dynamic conditions, which makes them unreliable for real-time precise control and estimation of soft wearable devices.

1.4 Evaluation of Wearable Soft Robots

Wearable soft robots have been tested on both healthy users and impaired users with slightly different goals. During healthy participant testing, the primary goals are to justify the design requirements, evaluate the overall benefit for healthy users, and provide preliminary evidence for the potential benefit on impaired users. Metabolic cost (Alan T Asbeck et al. 2015; Cao et al. 2020; Ding et al. 2016) and muscle effort (Saivimal Sridar et al. 2018; W. Kim et al. 2020; Al-Fahaam et al. 2018; Masia et al. 2018; Shuangyue Yu et al. 2019) are the two primary evaluation criteria for healthy users. For impaired user studies, the goal is concentrated on evaluating the

user's potential benefit when wearing the device and improvements in functional evaluation tasks are another main criterion for impaired users (Hussain et al. 2017; Tang et al. 2019; Ciullo et al. 2020; Zhou et al. 2019; Siviy et al. 2020; Hussain et al. 2016).

The metabolic cost reflects the overall energy changes when a wearable robot actively assists a user. In (Alan T Asbeck et al. 2015), a preliminary study was conducted on four healthy users to determine the gross benefit (device active versus device worn but inactive). A statistically significant reduction of the averaged metabolic was observed with the device being active. In (Cao et al. 2020), a study was conducted on three healthy users to evaluate the benefit of an untethered soft hip exosuit. The metabolic cost was reduced by 15.28% when full gait cycle assisted was compared with no device condition. Compared to the case without a soft robot, a minimal increase in the metabolic cost is expected with a passive soft wearable robot, and a reduction in metabolic cost is expected when the device is active. The metabolic cost can provide an overview of the benefits of a soft wearable robot, but it cannot provide details on the kinematic and kinetic changes of the assisted joint(s).

The muscle effort, in contrast to the metabolic cost, indicates the changes in a specific muscle or muscle group's activity when the attached device is active versus inactive (Theurel et al. 2018). Electromyography (EMG) sensors are the most commonly used non-invasive tools to estimate muscle force. In (Saivimal Sridar et al. 2018), a soft inflatable knee exosuit was tested on one healthy participant to assist the knee extension during the swing phase. Five EMG sensors were attached to the lower limb to evaluate the muscle efforts (device active versus inactive). A reduction was observed for the quadriceps when the device was active. Similarly, in (Li and Hashimoto 2017), a polyvinyl chloride gel soft hip actuator was tested on one

stroke patient with EMG sensors attached to the lower limb. It was demonstrated that the device could reduce the burden on the lower limbs' muscles during walking with an approximate reduction of 17% for the *rectus femoris* muscle, 11% for the *Sartorius*, and 5% for the hamstring. Similar to the metabolic cost, wearing a passive soft wearable robot may not significantly increase the muscle effort and a reduction is also expected when the robot is active. Although EMG sensors provide reliable muscle force estimation, their performance is quite sensitive to factors like skin conditions, and external load on the sensing area.

The improvements in functional evaluation tasks reflect the impaired user's performance changes in a specific functional task when a soft wearable robot is turned on. In (Hussain et al. 2017), a soft supernumerary finger was attached to one impaired user to regain the grasping function. The Box and Block Test and the Franchy Arm Test were performed on the participant, and improvements were observed in both cases. In (S. Sridar et al. 2020), a soft knee exosuit was applied to three impaired participants. A timed up-and-go test was performed to evaluate the device's performance during overground waking and a reduction in execution time was observed. In (Awad, Kudzia, et al. 2020), a cable-driven soft exosuit was tested on six participants in the chronic phase after the stroke. Both 10-meter walk and six-minute walk tests were conducted for all impaired users. Compared to the inactive case, the user walked 0.14 m/s during the first test and traveled 32 m farther during the second test on average. Similarly, in (Awad, Esquenazi, et al. 2020), the cable-driven soft exosuits were mounted on 44 post-stroke users for treadmill and over-ground training. After a 5 days training session with the device active, the average maximum walking speed for both device-assisted and unassisted was increased by 0.1 m/s and 0.07 m/s. The functional evaluation

task is specifically selected for each class of the impaired user and the assistance from the soft robots.

It should be noted that while both soft and rigid wearable robots have been tested on healthy or impaired users, limited research directly compares the performance of rigid and soft robots (Chiaradia et al. 2018), which presents an exciting topic for future research. In general, soft wearable robots have a great potential for assisting activities of daily living without close supervision by medical professionals because of their advantages in safety (Pang et al. 2020) and comfort (Koizumi et al. 2020). Due to the use of soft materials, human users will be at a lower risk even when the actuators malfunction or misalign with the human joints, compared to their rigid counterparts. While both active rigid and soft robots have been shown to be effective for healthy and impaired users, only soft robots can be worn passively without significantly increasing metabolic costs (Cao et al. 2020) or muscle efforts (Li and Hashimoto 2017). Hence, a user can wear these soft robots for a long time without feeling uncomfortable. Despite many advantages, there are still inherent problems yet to be resolved in soft wearable robots, such as friction in cable-driven systems (X. Yang et al. 2019) and slow response in fluid-driven systems (Saivimal Sridar et al. 2018).

1.5 Contributions

While wearable soft robots have successfully addressed some inherent design limitations faced by rigid wearable robots, they possess a unique set of challenges due to their soft and compliant nature. Some of these challenges are present in the sensing, modeling, control and evaluation of wearable soft robots.

Sensing in wearable soft robotics deals with the design of sensors and fusion

algorithms that utilize sensors that are compatible with the human and the soft robot, both of which limit the implementation of more common sensors used in traditional rigid robots, such as joint encoders and strain gauges. Modeling and characterization of soft robots face the challenges of developing representational models that deal with complex actuation and non-linear systems, such as fluidic, pneumatic and cable-driven systems. The evaluation of soft exosuits requires investigating the effects of wearable soft robots on humans and evaluating what are the most appropriate control and evaluation strategies that maximize the benefit obtained.

To address the unique challenges in wearable soft robots, this dissertation studies the sensing, modeling, control and evaluation of soft robots for wearable applications. Through three different case studies, this dissertation will aim at advancing the state-of-the-art in wearable technology by addressing individual challenges in the sensing, modeling and evaluation of soft robots.

In Chapter 2, a model-based sensor fusion algorithm in a flexible origami robot is developed for the expedited deployment and estimation of different users in diverse conditions. This is an advantage to machine learning estimation algorithms that require extensive data sets for model training. The efficacy of the proposed algorithm for human state estimation is tested through comprehensive human evaluations.

Chapter 3 addresses inherent limitations with rigid sensors and haptic actuators through the development of an inflatable soft haptic sensor. One of the main novelties of this device is that it enables gait sensing and provides haptic feedback to the user with a single compact instrument, a characteristic that is uncommon for rigid sensors and haptic motors. Models for soft sensors and haptic actuators are developed through mechanical characterization in quasi-static and dynamic conditions. The efficiency of

the developed device for gait sensing and haptic feedback is evaluated through human subject evaluations.

Lastly, in Chapter 4, comprehensive human testing is performed to study the neuromuscular and biomechanical effects of a wearable soft assistive device. A soft inflatable exosuit is utilized to assist the knee extension during a manual lifting task and the effects on the back and lower-limb muscles are analyzed. A reduction in the effort of muscle groups indicates the feasibility of reducing the risk of injury during a lifting task. This study exemplifies the need for comprehensive human evaluations in order to fully understand the benefit of wearable assistive devices.

Chapter 2

A KINEMATICALLY CONSTRAINED KALMAN FILTER FOR SENSOR FUSION IN A WEARABLE ORIGAMI ROBOT

2.1 Abstract

Sensing for wearable robots is an ongoing challenge, especially given the recent trend of soft and compliant robots. Recently, a wearable origami exoshell has been designed to sense the user's torso motion and provide mobility assistance. The materials of the exoshell contribute to a lightweight design with compliant joints, which are ideal characteristics for a wearable device. Common sensors are not ideal for the exoshell as they compromise these design characteristics. Rotary encoders are often rigid metal devices that add considerable weight and compromise the flexibility of the joints. IMU sensors are affected by environments with variable electromagnetic fields, and therefore not ideal for wearable applications. Hall effect sensors and gyroscopes are utilized as alternative compatible sensors, which introduce their own set of challenges: noisy measurements and drift due to sensor bias. To mitigate this, we designed the Kinematically Constrained Kalman Filter for sensor fusion of gyroscopes and Hall effect sensors, with the goal of estimating the human's torso and robot joint angles. We augmented the states to consider bias related to the torso angle in order to compensate for drift. The forward kinematics of the robot are incorporated into the Kalman Filter as state constraints to address the unobservability of the torso angle and its related bias. The proposed algorithm improved the estimation performance of the torso angle and its bias, compared to the individual sensors and the standard

Kalman Filter, as demonstrated through bench tests and experiments with a human user.

2.2 Introduction

Recently, a new trend for wearable devices referred to as wearable origami exoshell has been designed, which consists of origami modular structures that combine rigid and flexible materials (Li et al. 2023). The exoshell is fabricated with layers of cardboard and flexible polyester film, contributing to a lightweight and compliant device, which are ideal characteristics for a wearable design. The origami exoshell robot consists of triangular origami links that together form a serial link robot with flexible joints. This device was designed to be worn on the back of a human, as shown in Fig. 2.1, to sense the user's torso motion and provide mobility assistance.

Sensing for wearable robots is an ongoing challenge, especially given the recent trend of soft and compliant robots (E. Q. Yumbla et al. 2021). While placing rotary encoders at the robot's joints has been a common solution (Tiboni et al. 2022), our origami exoshell design is not ideal for traditional encoders. Rotary encoders are often rigid metal devices that add considerable weight to the design. Furthermore, the rigidness of typical encoders affects the robot's structural compliance, compromising the flexibility of the layer and therefore the mobility of the joint (F. Yumbla et al. 2022).

As an alternative, inertial measurement units (IMU) are used to measure the robot and human kinematics (Filippeschi et al. 2017). IMUs consist of a gyroscope, an accelerometer and a magnetometer. Although some studies have achieved good performance with IMU sensors, they often rely on using the magnetometer for drift correction (Wittmann, Lambercy, and Gassert 2019). This method is not ideal for

long-term wearable applications as it has been commonly reported that changes in the environment's magnetic field affect the magnetometer's reliability (Ahmad et al. 2013). Furthermore, it is often required to embed electronic hardware within the robot, which will inflict even more disturbances due to the magnetic field generated by these electronic components.

To overcome limitations in individual sensors, many studies have utilized sensor fusion algorithms, such as the Kalman Filter (KF). Several studies have been successful at improving estimation performance with the KF using a serial link robot similar to our origami exoshell. For example, in several studies (Lee and Choi 2019; Jeon, Tomizuka, and Katou 2009), a KF was designed to fuse multiple sensors in a rigid and fixed serial link robot. While performance was improved, the algorithms have the underlying assumption that the base coordinate frame is fixed, and therefore cannot be applied when the robot is in free motion while worn by a human user. Some studies have in fact focused on KF for wearable applications (Xu et al. 2018; Ponraj and Ren 2018), but they are commonly designed for estimating the human alone and do not take into account integration with a wearable robot system which introduces electromechanical disturbances to the sensors. In (Xu et al. 2018), the authors fuse the information from multiple IMU, but they do not take into account magnetic disturbances from either the environment or a wearable robot system.

The sensor hardware limitations discussed are hard constraints of our origami robot due to its design characteristics. Since placing an encoder is not possible and using magnetometers is not ideal, in this study we aim at encoder- and magnetometer-free sensor configurations. We utilize Hall effect sensors and gyroscopes as these sensors are lightweight, compact, and do not affect the flexibility of the joints. This introduces

additional challenges such as noisy measurements from the Hall sensor and drift due to gyroscope bias.

To mitigate the limitations of each individual sensor, we design a KF for sensor fusion of the gyroscopes and Hall effect sensors, to attenuate Hall effect sensor noise and compensate for drift due to gyroscope bias, which are the primary limitations of these sensors. The KF design is tailored towards our specific application: to estimate the human's torso and robot joint angles with a wearable serial link robot (with no fixed base frame). To compensate for drift, the bias related to the kinematics of each joint was included as a state estimate. Introducing these additional state estimates leads to the unobservability of the KF, specifically of the bias related to the torso kinematics. To handle this issue, we incorporate the forward kinematics of the robot into the KF as state constraints. Previous theoretical studies have noted the possibility of utilizing the state constraints to increase the observability of the KF (Alouani, Blair, and Watson 1991), and through this study, we demonstrate this approach for improving estimation performance with a wearable serial link robot. The proposed algorithm was evaluated on the origami exoshell through bench tests and with human participants wearing the device. Our formulation is a general approach that can be applicable to many wearable robots that contain a kinematic chain, such as lower-limb exoskeletons (Esquenazi et al. 2012; Zoss, Kazerooni, and Chu 2006; Tsukahara et al. 2010), back spine robots (X. Yang et al. 2019; Song et al. 2021; Roveda et al. 2020), and many other devices similar to our origami exoshell.

The remainder of this chapter is organized as follows. Section 2.3 discusses the exoshell robot design and sensor hardware, and Section 2.4 presents the formulation of our proposed algorithm: the Kinematically Constrained Kalman Filter (KCKF). Section 2.5 describes the experiments to evaluate the algorithm and presents the

results along with a discussion. Finally, the conclusions and future work are discussed in Section 2.6.

2.3 System Hardware

The system consists of an origami exoshell robot with embedded sensors throughout the structure of the robot, as presented in Fig. 2.1. The origami robot design and the sensors will be described in the following sections.

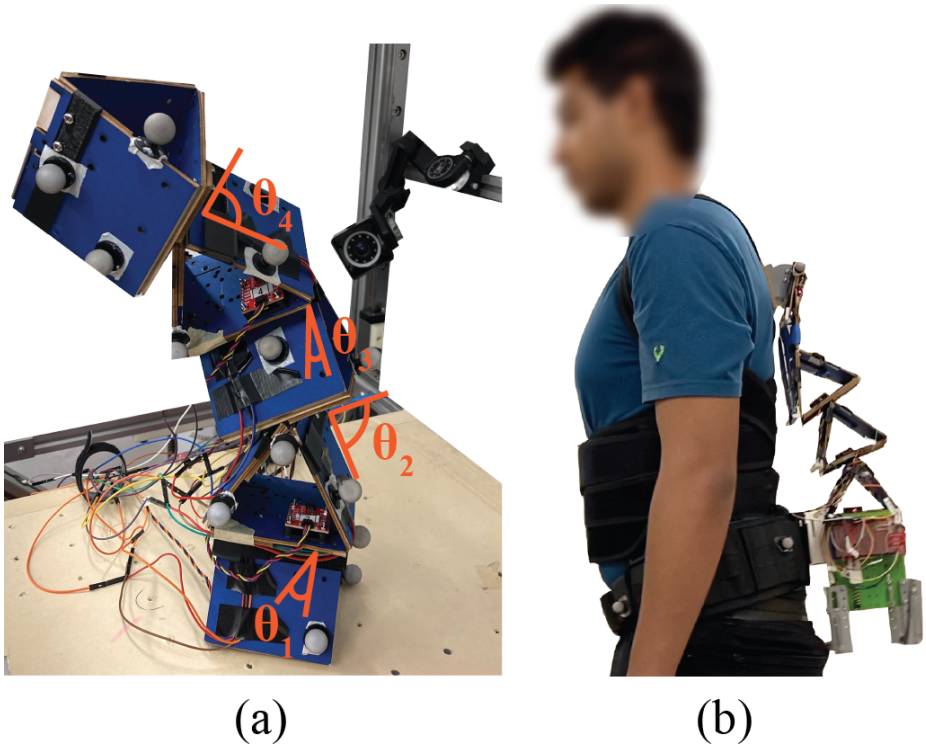

Figure 2.1. Origami exoshell and experimental setup to evaluate the kinematic estimation of the fusion algorithm: (a) bench test setup, and (b) test with the human user wearing the origami exoshell.

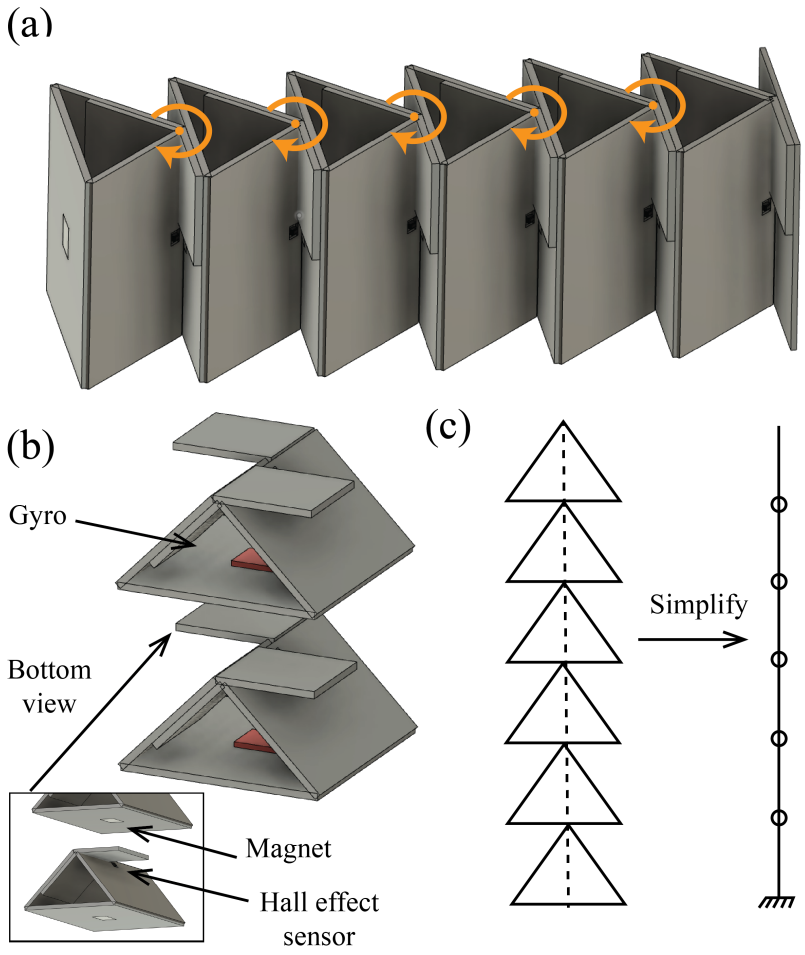

Figure 2.2. (a) Origami exoshell design; arrows indicate direction of rotation. (b) Hall effect sensors are mounted at each joint, and gyroscopes are mounted within each link. (c) The exoshell consists of triangular origami modules that form a serial link robot with discrete joints when connected together.

2.3.1 Origami Robot Design

The basic building module of the origami exoshell is a triangular origami link that enables one degree of freedom (DOF) rotational motion with a 60 deg range of motion (ROM). The triangular modules are connected next to each other to form a serial link robot, as depicted in Fig. 2.2. The modularity of this design allows the assembly of wearable serial link robots with multiple DOF that are capable of achieving rotational orientation in three dimensions (3D). The origami exoshell was designed to be worn

on the back of the human, as shown in Fig. 2.1, in order to estimate and assist the user's torso motion. More details on the origami exoshell design can be found in (Li et al. 2023).

The triangular modules are fabricated with two outer rigid layers of cardboard and a middle flexible polyester layer that forms a living hinge. The flexibility of the layer is the fundamental mechanism that allows 1-DOF rotational motion of the origami. The selected materials are lightweight and have inherent compliance, ideal for wearable devices. As shown, the origami exoshell design avoids the use of heavy and rigid metal elements that could compromise the robot's lightweight and compliant characteristics. Rotary encoders are typically rigid and bulky metal devices. Therefore, embedding rotary encoders within the origami exoshell is not possible as it adds considerable weight and because there is limited area for mounting. Furthermore, the rigidness of typical encoders affects the robot's structural compliance, compromising the flexibility of the layer and therefore the mobility of the joint. As a solution, the origami robot was embedded with Hall effect sensors as an alternative to rotary encoders. Gyroscopes were also mounted at each module to obtain angular rate measurements of each link.

2.3.2 Hall Effect Sensors

Hall effect sensors (DRV5053, Texas Instrument, Dallas, TX, USA) were used on the origami robot to measure the relative angle of the joint. These sensors do not compromise the exoshell design as they are compact and lightweight, with a size of 4 mm by 3 mm, and a weight of 0.1 g. In contrast, a typical rotary encoder weighs approximately 100 g.

Hall effect sensors have the capability to sense the magnetic flux density. A pair of

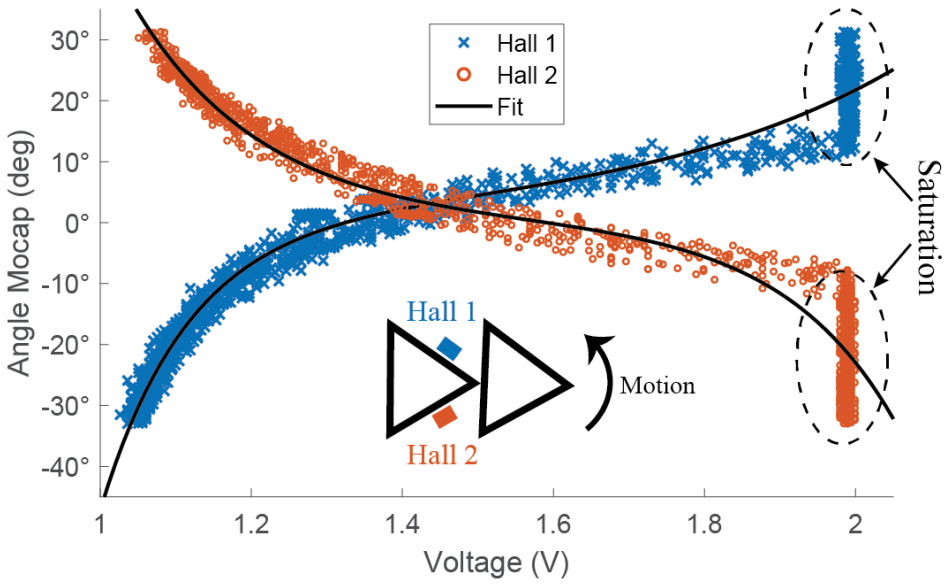

Figure 2.3. Hall effect sensors characterization plot. Two Hall effect sensors are placed on opposite sides of the origami joint, depicted as colored boxes in the illustration.

magnets and Hall effect sensors were mounted on the joints of the origami robot, as depicted in Fig 2.2. In this scenario, changes in the joint angle lead to changes in the magnetic flux density measured by the Hall effect sensor, due to changes in alignment and proximity between the magnetic field and the sensor. As such, the Hall effect sensor exhibits a response to the joint angle state. This working principle allows using a Hall effect sensor for 1-DOF joint angle estimation.

A sensor characterization was performed to analyze the sensor response to joint angle state. A cyclic motion was performed on a single origami hinge while recording Hall effect sensor measurements and ground truth measurements of the origami's joint angle obtained from a Motion Capture system (T40s, VICON Inc., Los Angeles, CA). The sensor response is presented in Fig. 2.3. An exponential curve fitting was performed over the Hall effect sensor characterization data to obtain a mathematical model that allows estimating the origami's joint angle. The model for one sensor is

summarized in (2.1) in which V is the voltage measured from the sensor and θ_h is the estimated angle measurement of the Hall effect sensor.

$$\theta_h(V) = 0.07e^{2.87V} - (2.22 \times 10^5)e^{-8.43V} \tag{2.1}$$

The sensor characterization in Fig. 2.3 demonstrates a significant saturation for one side of the origami's joint angle (e.g., $\theta > 0$) which considerably affects the estimation performance for this region. As such, two Hall effect sensors were mounted on opposite sides of each joint in order to measure the complete ROM by operating simultaneously, as illustrated in Fig. 2.3.

2.3.3 Gyroscope Sensor

Gyroscope sensors (LSM6DSO, STMicroelectronics, Geneva, Switzerland) were used on the origami robot to measure the angular rate of the links and estimate the joint angular position. The gyroscopes were mounted on each link of the origami exoshell robot as demonstrated in Fig. 2.2. The relative orientation between each gyroscope was physically aligned to one another by means of design constraints, and as such allowed the assumption that in the neutral position the inertial frames of the gyroscopes are aligned. With this assumption, the angular rate of each joint can be computed by measuring the neighboring gyroscopes as follows,

$$\dot{\boldsymbol{\theta}}_{\boldsymbol{i}} = \boldsymbol{\omega}_{\boldsymbol{i}} - \boldsymbol{\omega}_{\boldsymbol{i-1}} \tag{2.2}$$

where $\dot{\boldsymbol{\theta}}_{\boldsymbol{i}} = [\dot{\theta}_x \ \dot{\theta}_y \ \dot{\theta}_z]_i$ is the 3D angular speed of joint i with respect to the x-, y-

and z-axis, and $\boldsymbol{\omega_i} = [\omega_x\ \omega_y\ \omega_z]_i$ is the gyroscope 3D angular rate measurement of link l_i with respect to the x-, y- and z-axis.

The joint angle can be estimated by integration of the joint's angular rate (2.2) obtained through the gyroscope measurements. However, a major disadvantage is that integration of the gyroscope signal leads to a drift in the joint angle estimate that decays performance over extended use.

2.4 Sensor Fusion With Kalman Filter

The origami robot was integrated with two different types of sensors: gyroscopes and Hall effect sensors. Both types of sensors have different sensing capabilities but complementary qualities for joint angle estimation. The Hall effect sensors are able to directly measure the joint angle state but provide a significantly noisier measurement. In contrast, gyroscopes provide a less noisy estimate of the joint angle but they suffer from bias which significantly affects the estimation performance over time. The limitations and advantages of each sensor have complementary properties to one another, as the Hall effect sensor can be used to compensate for the drift in the gyroscopes measurements, and the gyroscope provides a significantly less noisy measurement input. These complementary properties make sensor fusion an ideal method to overcome the individual limitations of each sensor and improve joint angle estimation performance.

2.4.1 Kalman Filter Algorithm Formulation

The KF was selected as the method to fuse the sensor information from the gyroscopes and the Hall effect sensors. The formulation of our KF will consider the general case of a serial link origami robot with n joints and three DOF at each joint. This formulation aims to estimate the 3D kinematics of the robot and the human.

The standard form of the KF for the discrete domain in state space consists of the state transition equation (2.3) and the measurement equation (2.4).

$$\boldsymbol{x}(k+1) = A\boldsymbol{x}(k) + B\boldsymbol{u}(k) + \boldsymbol{\nu}(k), \tag{2.3}$$

$$\boldsymbol{y}(k) = C\boldsymbol{x}(k) + \boldsymbol{\upsilon}(k), \tag{2.4}$$

where $\boldsymbol{x}(k) \in \mathbb{R}^{(6n+6)\times 1}$ and $\boldsymbol{y}(k) \in \mathbb{R}^{(6n+3)\times 1}$ are the system state and measurement vectors at time k; $\boldsymbol{\nu}(k)$ and $\boldsymbol{\upsilon}(k)$ are the process noise and measurement noise with covariances $Q \in \mathbb{R}^{(6n+6)\times(6n+6)}$ and $R \in \mathbb{R}^{(6n+3)\times(6n+3)}$.

Considering a serial link robot with n joints, and two Hall effect sensors per joint, the system measurement is given by (2.5),

$$\boldsymbol{y}(k) = [\boldsymbol{\theta}^{\boldsymbol{l}}_{\boldsymbol{h_1}}(k)\ \ \boldsymbol{\theta}^{\boldsymbol{r}}_{\boldsymbol{h_1}}(k)\ \cdots\ \boldsymbol{\theta}^{\boldsymbol{l}}_{\boldsymbol{h_n}}(k)\ \ \boldsymbol{\theta}^{\boldsymbol{r}}_{\boldsymbol{h_n}}(k)\ ]^T, \tag{2.5}$$

where $\boldsymbol{\theta}^{\boldsymbol{l}}_{\boldsymbol{h_i}} = [\theta^l_{hx}\ \theta^l_{hy}\ \theta^l_{hz}]_i$ and $\boldsymbol{\theta}^{\boldsymbol{r}}_{\boldsymbol{h_i}} = [\theta^r_{hx}\ \theta^r_{hy}\ \theta^r_{hz}]_i$ are the left side ($\boldsymbol{\theta}^{\boldsymbol{l}}_{\boldsymbol{h_i}}$) and right side ($\boldsymbol{\theta}^{\boldsymbol{r}}_{\boldsymbol{h_i}}$) Hall effect sensor angle measurements of joint i with respect to the x-, y-, and z-axis.

The input to the system is the angular rate, as it is imposed by the human's

movement.

$$\boldsymbol{u}(k) = [\boldsymbol{\omega_1}(k)\ \ \boldsymbol{\omega_2}(k)\ \cdots\ \boldsymbol{\omega_{n+1}}(k)\ ]^T. \tag{2.6}$$

The system states $\boldsymbol{x}(k)$ include the robot joint angles $\boldsymbol{\theta_i} = [\theta_x\ \theta_y\ \theta_z]_i$ and the human torso angles $\boldsymbol{\phi_i} = [\phi_x\ \phi_y\ \phi_z]_i$ with respect to the x-, y- and z-axis, as depicted in Fig. 2.4. The human torso angle $\boldsymbol{\phi}$ corresponds to the robot's end-effector orientation with respect to the base frame, as shown in Fig. 2.4(b). To compensate for gyroscope drift, the system state of the standard KF was augmented to include an estimation of the gyroscope sensor bias $\boldsymbol{b_i}$. The system states are given by (2.7), where $\boldsymbol{b_i} = [b_x\ b_y\ b_z]_i$ are the gyroscope bias corresponding to joint i, and $\boldsymbol{b_\phi} = [b_x\ b_y\ b_z]_\phi$ is the bias corresponding to $\boldsymbol{\phi}$.

$$\begin{aligned}\boldsymbol{x}(k) = [&\boldsymbol{\theta_1}(k)\ \ \boldsymbol{\theta_2}(k) \cdots \boldsymbol{\theta_n}(k)\ \ \boldsymbol{\phi}(k)\\ &\boldsymbol{b_1}(k)\ \ \boldsymbol{b_2}(k) \cdots \boldsymbol{b_n}(k)\ \ \boldsymbol{b_\phi}(k)\ ]^T\end{aligned} \tag{2.7}$$

With this formulation, the measurement matrix C is,

$$C = \begin{bmatrix} I_3 & 0_3 & \cdots & 0_3 & 0_3 & \cdots & 0_3 \\ I_3 & 0_3 & \cdots & 0_3 & 0_3 & \cdots & 0_3 \\ 0_3 & I_3 & \cdots & 0_3 & 0_3 & \cdots & 0_3 \\ 0_3 & I_3 & \cdots & 0_3 & 0_3 & \cdots & 0_3 \\ \vdots & \vdots & \ddots & \vdots & \vdots & \ddots & \vdots \\ 0_3 & 0_3 & \cdots & I_3 & 0_3 & \cdots & 0_3 \\ 0_3 & 0_3 & \cdots & I_3 & 0_3 & \cdots & 0_3 \end{bmatrix}, \tag{2.8}$$

where I_n is a $n \times n$ identity matrix, and 0_n represents a $n \times n$ matrix with all elements being zero. The structure of the measurement matrix C shows that for each joint two

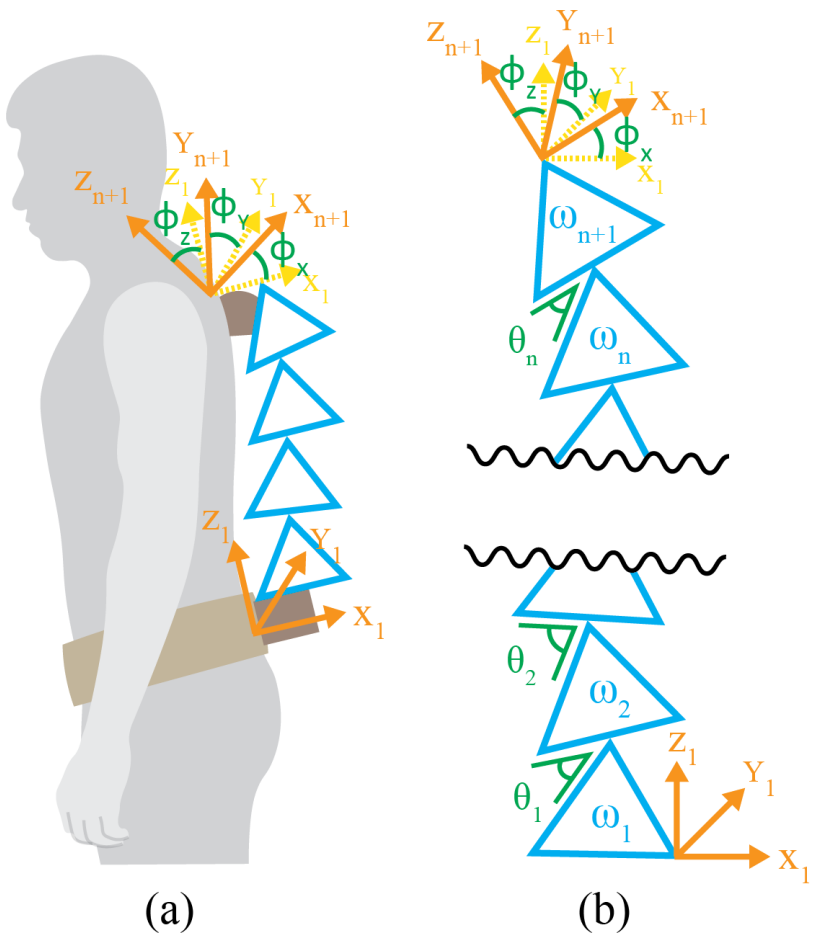

Figure 2.4. (a) Human wearing the origami exoshell robot; torso angles $\boldsymbol{\phi}$ correspond to the relative orientation between the coordinate frames of the top and bottom body segments. (b) Illustration of the origami exoshell robot with state variables; the torso angles $\boldsymbol{\phi}$ correspond to the relative orientation between the coordinate frames of the base and the end-effector links of the origami robot.

Hall effect sensors measure simultaneously the angle state to avoid loss of information due to sensor saturation.

For the process model of the system, we assume the following discrete first-order dynamic model,

$$\boldsymbol{\theta_i}(k+1) = \boldsymbol{\theta_i}(k) + (\boldsymbol{\omega_{i+1}}(k) - \boldsymbol{\omega_i}(k) - \boldsymbol{b_i}(k))t_s, \tag{2.9}$$

where t_s is the time between sampled measurements. The process model in (2.9) describes the evolution of the joint angle state and incorporates the gyroscope measurement and its related drift due to sensor bias.

Similarly, the process model for the human's torso angle is given by (2.10). The human torso angle $\boldsymbol{\phi}$ corresponds to the robot's end-effector orientation with respect to the base, as depicted in Fig. 2.4, and therefore utilizes the gyroscope measurements of the base ($\boldsymbol{\omega_1}$) and the end-effector link ($\boldsymbol{\omega_{n+1}}$) to simulate a virtual joint. To compensate for the combined bias effect of the two gyroscopes at the distal ends of the robot, a bias of the virtual joint $\boldsymbol{b_\phi}$ is incorporated into the process model.

$$\boldsymbol{\phi}(k+1) = \boldsymbol{\phi_i}(k) + (\boldsymbol{\omega_{n+1}}(k) - \boldsymbol{\omega_1}(k) - \boldsymbol{b_\phi}(k))t_s \tag{2.10}$$

According to this process model, the transition matrix A is given by (2.11).

$$A = \begin{bmatrix} I_3 & 0_3 & \cdots & 0_3 & 0_3 & -I_3 t_s & 0_3 & \cdots & 0_3 & 0_3 \\ 0_3 & I_3 & \cdots & 0_3 & 0_3 & 0_3 & -I_3 t_s & \cdots & 0_3 & 0_3 \\ \vdots & \vdots & \ddots & \vdots & \vdots & \vdots & \vdots & \ddots & \vdots & \vdots \\ 0_3 & 0_3 & \cdots & I_3 & 0_3 & 0_3 & 0_3 & \cdots & -I_3 t_s & 0_3 \\ 0_3 & 0_3 & \cdots & 0_3 & I_3 & 0_3 & 0_3 & \cdots & 0_3 & -I_3 t_s \\ 0_3 & 0_3 & \cdots & 0_3 & 0_3 & I_3 & 0_3 & \cdots & 0_3 & 0_3 \\ 0_3 & 0_3 & \cdots & 0_3 & 0_3 & 0_3 & I_3 & \cdots & 0_3 & 0_3 \\ \vdots & \vdots & \ddots & \vdots & \vdots & \vdots & \vdots & \ddots & \vdots & \vdots \\ 0_3 & 0_3 & \cdots & 0_3 & 0_3 & 0_3 & 0_3 & \cdots & I_3 & 0_3 \\ 0_3 & 0_3 & \cdots & 0_3 & 0_3 & 0_3 & 0_3 & \cdots & 0_3 & I_3 \end{bmatrix} \tag{2.11}$$

The input model is given by the matrix in (2.12) according to the process model.

$$B = \begin{bmatrix} -I_3 t_s & I_3 t_s & 0_3 & \cdots & 0_3 & 0_3 \\ 0_3 & -I_3 t_s & I_3 t_s & \cdots & 0_3 & 0_3 \\ 0_3 & 0_3 & -I_3 t_s & \cdots & 0_3 & 0_3 \\ \vdots & \vdots & \vdots & \ddots & \vdots & \vdots \\ 0_3 & 0_3 & 0_3 & \cdots & -I_3 t_s & I_3 t_s \\ -I_3 t_s & 0_3 & 0_3 & \cdots & 0_3 & I_3 t_s \\ & & 0_{3n+3} & & & \end{bmatrix} \tag{2.12}$$

Then, the process noise covariance for this model is,

$$Q = \begin{bmatrix} \frac{{t_s}^4}{4} I_{(3n+3)} & \frac{{t_s}^3}{2} I_{(3n+3)} \\ \frac{{t_s}^3}{2} I_{(3n+3)} & {t_s}^2 I_{(3n+3)} \end{bmatrix} \tag{2.13}$$

In the next section, the standard formulation of the KF will be augmented to incorporate state constraints over the joint kinematics.

2.4.2 State Constraints in the Kalman Filter

Since the origami robot consists of a series of interconnected links, there exists a kinematic chain that imposes state dependencies between a particular joint and the subsequent joints. Examining the illustration in Fig. 2.4, we can identify that the human torso angle corresponds to the end-effector orientation, which can also be obtained through the forward kinematics of the robot. For a serial link robot, the equation of the forward kinematics F depends on the states of all the robot joints. In our case, the forward kinematics that relates to the human torso angle are given by

(2.14).

$$\boldsymbol{\phi} = F(\boldsymbol{\theta}) = \Sigma\boldsymbol{\theta_i} = \boldsymbol{\theta_1} + \boldsymbol{\theta_2} + \cdots + \boldsymbol{\theta_n}. \tag{2.14}$$

The forward kinematics equation provides an equality state constraint in the form of (2.15), which can be implemented into the KF.

$$D\boldsymbol{x}(k) = \boldsymbol{d} \tag{2.15}$$

The KF measurement equation can be augmented to include equality state constraints by treating it as a perfect measurement as shown in (2.16), where $\mathbf{0_{3,1}}$ represents a 3×1 vector with all elements being zero.

$$\begin{bmatrix} \boldsymbol{y}(k) \\ \boldsymbol{d} \end{bmatrix} = \begin{bmatrix} C \\ D \end{bmatrix} \boldsymbol{x}(k) + \begin{bmatrix} \boldsymbol{v}(k) \\ \mathbf{0_{3,1}} \end{bmatrix} \tag{2.16}$$

In this context, the corresponding values for the variables of the state constraints are $\boldsymbol{d} = [0 \;\; 0 \;\; 0]^T$, and

$$D = \begin{bmatrix} I_3 & I_3 \cdots I_3 & -I_3 & 0_3 & 0_3 & 0_3 \cdots 0_3 & 0_3 \end{bmatrix}. \tag{2.17}$$

To incorporate the kinematic state constraints into the KF formulation, the measurement vector and the measurement matrix were augmented as shown below.

$$\boldsymbol{y}(k)_{KCKF} = [\boldsymbol{\theta}^{\boldsymbol{l}}_{\boldsymbol{h_1}}(k) \;\; \boldsymbol{\theta}^{\boldsymbol{r}}_{\boldsymbol{h_1}}(k) \cdots \boldsymbol{\theta}^{\boldsymbol{l}}_{\boldsymbol{h_n}}(k) \;\; \boldsymbol{\theta}^{\boldsymbol{r}}_{\boldsymbol{h_n}}(k) \;\; \mathbf{0_{1,3}} \;]^T \tag{2.18}$$

$$C_{KCKF} = \begin{bmatrix} I_3 & 0_3 & \cdots & 0_3 & 0_3 & 0_3 & 0_3 & \cdots & 0_3 & 0_3 \\ I_3 & 0_3 & \cdots & 0_3 & 0_3 & 0_3 & 0_3 & \cdots & 0_3 & 0_3 \\ 0_3 & I_3 & \cdots & 0_3 & 0_3 & 0_3 & 0_3 & \cdots & 0_3 & 0_3 \\ 0_3 & I_3 & \cdots & 0_3 & 0_3 & 0_3 & 0_3 & \cdots & 0_3 & 0_3 \\ \vdots & \vdots & \ddots & \vdots & \vdots & \vdots & \vdots & \ddots & \vdots & \vdots \\ 0_3 & 0_3 & \cdots & I_3 & 0_3 & 0_3 & 0_3 & \cdots & 0_3 & 0_3 \\ 0_3 & 0_3 & \cdots & I_3 & 0_3 & 0_3 & 0_3 & \cdots & 0_3 & 0_3 \\ I_3 & I_3 & \cdots & I_3 & -I_3 & 0_3 & 0_3 & \cdots & 0_3 & 0_3 \end{bmatrix} \tag{2.19}$$

Now, according to the modified measurement equation, the measurement noise covariance R is given by,

$$R = \begin{bmatrix} {\sigma_{hall}}^2 I_{6n} & 0_{6n\times 3} \\ 0_{3\times(6n+3)} \end{bmatrix}, \tag{2.20}$$

where $0_{n\times m}$ represents a $n \times m$ matrix with all elements being zero, and σ_{hall} is the standard deviation of the Hall effect sensor noise which was obtained experimentally ($\sigma_{hall} = 3.2$ deg).

2.4.3 Observability of the Kalman Filter

A KF with a system of unobservable states will not converge to a meaningful solution, since by definition, an unobservable state is one in which no information may be obtained through the measurement equations (Southall, Buxton, and Marchant 1998). The observability of the KCKF was analyzed, which takes into account the process model (2.3) and measurement equation (2.4). A system with a state vector

$\boldsymbol{x}(k)$ of dimension N is observable if the observability matrix O defined in (2.21), has a row rank N.

$$O = \begin{bmatrix} C \\ CA \\ \vdots \\ CA^{i} \\ \vdots \\ CA^{N-1} \end{bmatrix} \tag{2.21}$$

We computed the observability matrix O and analyzed the observability of each state variable by inspecting that the corresponding column vector of O is linearly independent. The observability matrix of the KCKF, defined by (2.11) and (2.19), has row rank N, which implies that the system has full observability of all the states. In contrast, the observability matrix of the standard KF, defined by (2.11) and (2.8), which does not incorporate the kinematic state constraints, has a row rank $N - 6$, which reveals that the system is unobservable. Specifically, the state variables that are unobservable are the 3D torso angle $\boldsymbol{\phi}$ and its related bias $\boldsymbol{b}_{\boldsymbol{\phi}}$.

The observability analysis reveals that incorporating forward kinematics as state constraints contribute to achieving the observability of the system. This is because the KCKF treats the forward kinematics of the robot as measurements and provides information of the torso angle state $\boldsymbol{\phi}$ in (2.10), which combined with (2.9) permits observability of the related bias state $\boldsymbol{b}_{\boldsymbol{\phi}}$.

2.5 Experiments, Results and Discussion of Fusion Algorithm Performance

The estimation performance of the sensor fusion algorithm was verified with the origami exoshell design presented in Fig. 2.1. The joint kinematics of the origami robot were estimated with the sensor fusion algorithm and compared to ground truth measurements obtained from a motion capture system. Three types of experiments were performed to evaluate the performance of the algorithm: cyclic motion test, extended use test, and evaluation with a human user. Through the experiments we will demonstrate the capability of our fusion algorithm to: 1) attenuate sensor noise, 2) compensate drift due to sensor bias, 3) be robust for extended use, and 4) be capable of improving kinematic estimation performance.

2.5.1 Cyclic Motion Experiments

The motion performed on the origami robot was aimed to mimic the human's motion during gait. A cyclic motion, similar to the motion of the human's torso during walking, was manually induced on the origami robot.

The experimental setup can be seen in Fig. 2.1(a). For this experiment, the origami robot consisted of five links, and four joints ($n = 4$). Two of the joints allowed rotation about the x-axis (θ_1 and θ_3) and the other two about the y-axis (θ_2 and θ_4). With this configuration, the origami robot can perform rotational motion in two dimensions (2D). Therefore, the KCKF will estimate the robot's and the human's 2D joint kinematics.

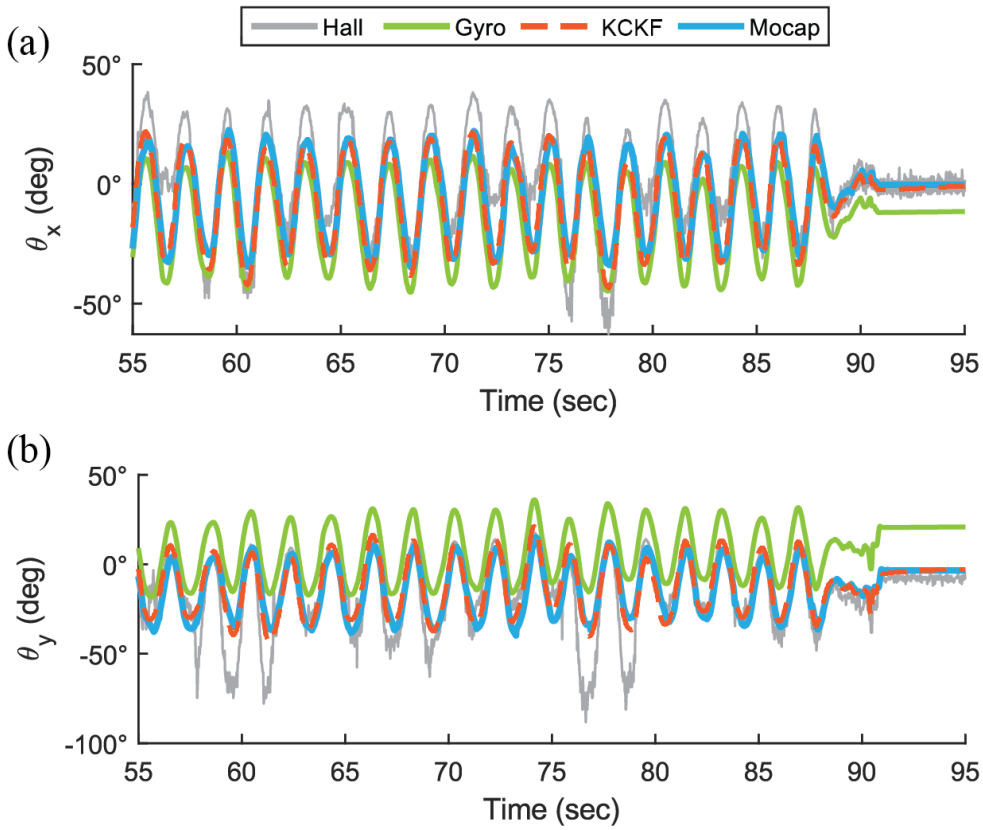

Figure 2.5. Joint kinematic estimation of individual sensors and the KCKF sensor fusion algorithm. Included are the robot kinematics of: (a) θ_3 (x-axis rotation), and (b) θ_4 (y-axis rotation).

2.5.1.1 Results of Sensor Fusion and Individual Sensors

The results of the sensor fusion estimation and the individual's sensor estimation through the experiment for two robot joints (θ_{3x} and θ_{4y}) are presented in Fig. 2.5. This figure compares the kinematics estimation obtained from each individual sensor and the estimation from the proposed KCKF. In this figure, it can be observed that the Hall effect sensor produces noisy estimates that deviate from the true value, especially at high joint angles. In addition, the angle estimation obtained from the gyroscope integration demonstrates significant drift, which can be easily visualized at the end of the experiment, approximately after 90 sec. The proposed KCKF sensor fusion

algorithm provided a smooth and drift-free joint angle estimate, compared to Hall sensor measurements and gyroscope integration, respectively.

The root-mean-square errors (RMSE) for the complete trial were computed using the motion capture data as ground truth. The joint angle RMSE of the individual sensors and the fusion algorithm are summarized in Table 2.1. The overall results reveal that the sensor fusion algorithm is capable of significantly reducing the RMSE compared to the estimates obtained from individual sensors. Our proposed fusion algorithm achieves a maximum RMSE reduction of approximately 87% compared to the estimate of the lowest performing sensor. Furthermore, the fusion algorithm was consistent in improving the kinematic estimate for each joint of the complete robot with overall better performance than the baseline sensor estimation.

The results of this experiment demonstrated that the proposed KCKF has the capability to overcome individual sensor limitations, as the fusion estimate attenuated noise-related error from the Hall sensor and compensated drift due to gyroscope sensor bias. Compared to the estimation from each individual sensor, our proposed algorithm provides a joint angle estimate that is closer to ground truth.

Table 2.1. RMSE (deg) of Kinematic Estimation

Joint	Gyro	Hall 1	Hall 2	Std KF	KCKF
θ_{1x}	31.66	20.96	14.33	5.29	5.07
θ_{2y}	9.78	14.74	10.06	6.12	6.11
θ_{3x}	3.70	6.62	6.04	3.41	3.46
θ_{4y}	20.25	12.13	7.44	6.11	6.00
ϕ_x	11.41	-	-	50.27	5.14
ϕ_y	44.01	-	-	17.98	5.94

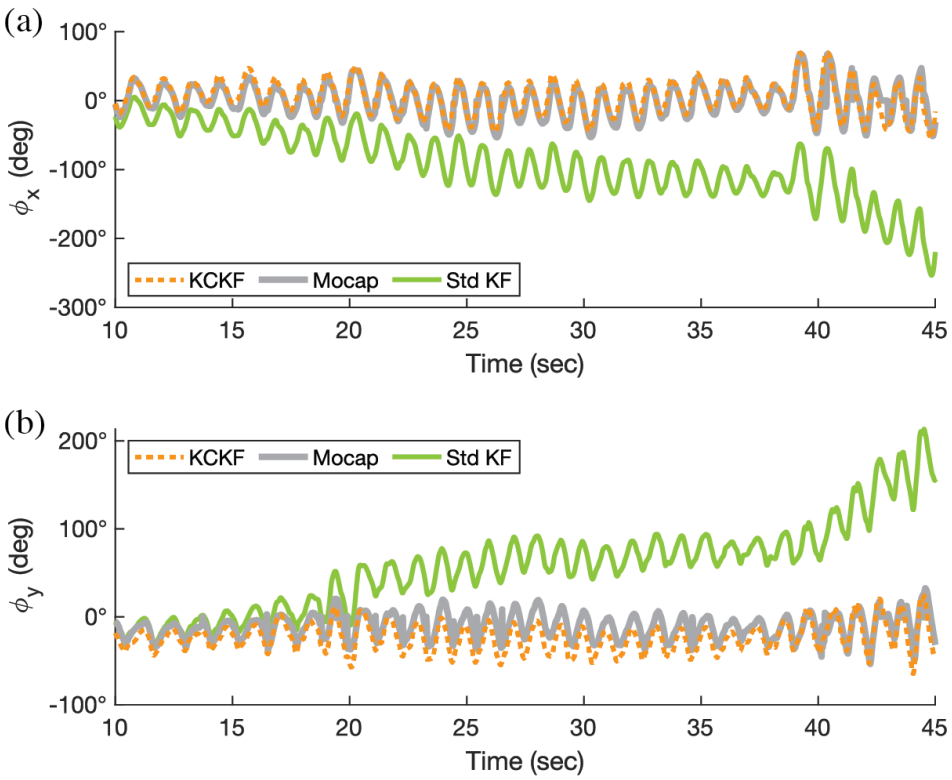

Figure 2.6. Comparison of the KCKF and the standard KF. The results include the torso angle: (a) in the sagittal plane (x-axis), and (b) in the lateral plane (y-axis).

2.5.1.2 Results of Kinematic State Constraints in KF

The results of the torso kinematic estimation from the fusion algorithm and the motion capture are presented in Fig. 2.6. This figure includes a comparison of the KCKF and the standard KF without state constraints. The RMSE for the KCKF and the standard KF are summarized in Table 2.1. The results reveal that incorporating state constraints improves the overall estimation performance compared to the standard KF, with a maximum RMSE reduction of approximately 90% for the torso angle ($\boldsymbol{\phi}$) estimation. The difference in performance is due to the fact that the state constraints contribute to having full observability of the system and enable estimating the state of the torso angle and its related bias, as discussed in

Section 2.4.3. Without the state constraints, it is challenging to achieve acceptable performance with the standard KF as it is unable to compensate for the sensor bias that leads to drift. This result demonstrates the implications of incorporating the robot's forward kinematics into the KF as state constraints on the estimation performance of unobservable states.

2.5.2 Extended Use Test

As a wearable device, one requirement for the algorithm is that it is robust through the use of a complete day. Long-duration tests were performed to verify that the algorithm's performance does not decay significantly through extended use. The test protocol consisted of introducing an initial movement on the origami robot and then fixing the position for an extended period of time to analyze the drift. To verify extended performance, the KCKF was tested on the origami robot for a duration of one hour and the drift was compared with the standard KF. The drift of the kinematic estimate for one joint throughout the experiment is plotted in Fig. 2.7.

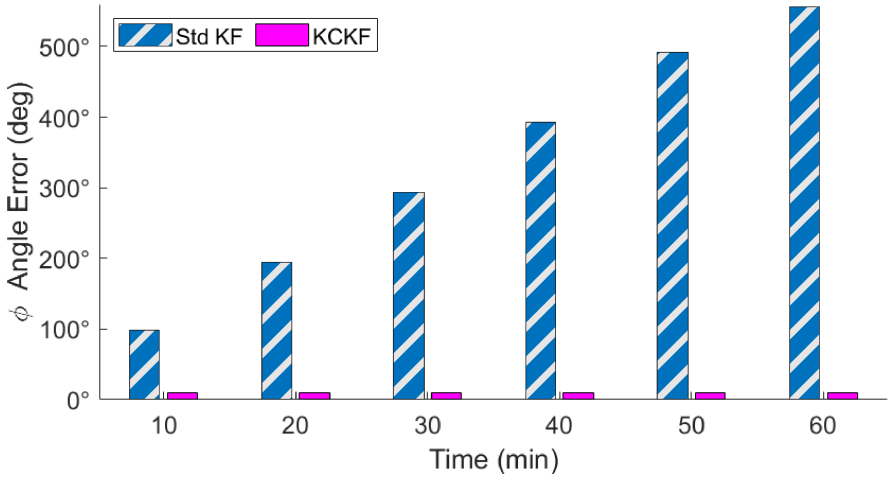

Figure 2.7. Drift of kinematic estimation over one hour

Over the extension of one hour, it is visible that the proposed KCKF is capable of accurately estimating joint kinematics and compensates for the significant drift that the gyroscope bias induces. By the end of the one-hour trial, the standard KF had drifted by approximately 550 deg, while our proposed KCKF algorithm was still within 7 deg of the true value. The results demonstrate that the KCKF maintains estimation performance through extended use and that our proposed formulation exceeds the standard KF performance.

2.5.3 Testing with Human Subject

The performance of the KCKF was evaluated with a human user for estimating the torso kinematics while performing activities of daily living. One healthy participant (28 years, 86 kg, 1.7 m) was recruited for this study. The experimental setup with the human user wearing the origami robot can be seen in Fig. 2.1(b). In this experiment, the subject performed a bending and extension motion (with 30 deg ROM) of the upper torso that mimics the cyclic movement in activities such as walking or repetitive lifting.

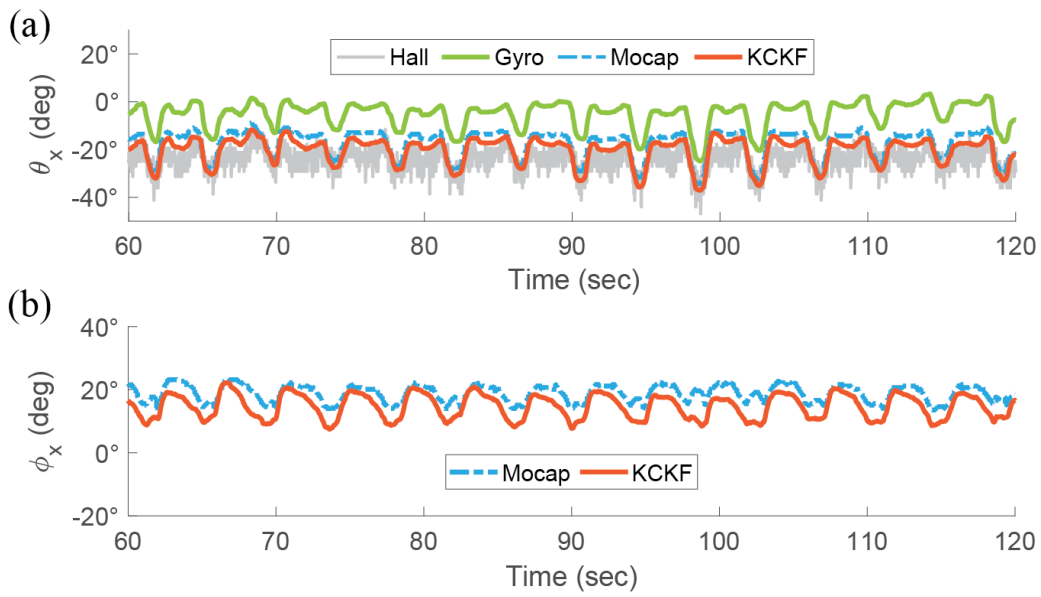

Figure 2.8. Kinematic estimation while wearing the origami exoshell robot. The plots include: (a) the robot kinematics for θ_2, and (b) the human's torso kinematics ϕ.

The human torso kinematics estimated by the KCKF are presented in Fig. 2.8. The results reveal that when the exoshell is worn, the KCKF can accurately estimate the torso joint angle, with 4.85 deg RMSE. Figure 2.8(b) shows that the kinematic estimation captures the cyclic profile of the torso's movement, which is required for control of the origami robot. This experiment revealed the existence of interaction forces between the robot and the user that cause sensor misalignment. We observed that sensor placement shifted when there was compression and over-extension of the robot. Compression occurred when the torso was straight (i.e., when ϕ is close to 0 deg) and over-extension when the torso was bending (i.e., when ϕ reaches its maximum), both of which cause estimation error during those instances, as seen in Fig. 2.8(b).

2.6 Conclusions

In this Chapter, we presented the formulation of the KCKF, a sensor fusion algorithm tailored for a wearable origami serial link robot. Our unique origami exoshell design has inherent constraints that require an encoder- and magnetometer-free sensor configuration. We developed a sensor fusion algorithm that uses gyroscopes and Hall effect sensors, as they are compatible sensors, but are affected by noise and sensor bias. Building upon early theory in KF, this Chapter demonstrated through experiments the benefits of incorporating the robot's forward kinematics as state constraints in order to address the unobservability of the system. The results demonstrated that our proposed KCKF improved state estimation performance, compared to the individual sensor measurements and the standard KF. Future work includes implementing the KCKF for real-time control of the origami exoshell robot. We plan to expand the formulation of our KCKF algorithm to incorporate dynamics of the origami exoshell to estimate interaction forces between the robot and the user for more precise control of the robot.

Chapter 3

GAIT SENSING AND HAPTIC FEEDBACK USING AN INFLATABLE SOFT HAPTIC SENSOR

3.1 Abstract

Collecting gait data and providing haptic feedback are essential for the safety and efficiency of robot-based rehabilitation. However, readily available devices that can perform both are scarce. This Chapter presents a novel method for mutual sensing and haptic feedback, through the development of an Inflatable Soft Haptic Sensor (ISHASE). The design, modeling and characterization of ISHASE are discussed. Four ISHASE are embedded in the insole of a shoe to measure ground reaction forces and provide haptic feedback. Four participants were recruited to evaluate the performance of ISHASE as a sensor and haptic device. Experimental results indicate that ISHASE can accurately estimate the user's ground reaction forces while walking, with a maximum and a minimum accuracy of 91% and 85% respectively. Haptic feedback was delivered to four different locations under the foot and the users could identify the location with an average 92% accuracy. A case study, that exemplifies a rehabilitation scenario, is presented to demonstrate the ISHASE's usefulness for mutual sensing and haptic feedback.

3.2 Introduction

Gait sensing and haptic feedback are essential for robot-based rehabilitation. Both rigid exoskeletons and soft exosuits have been developed to provide physical assistance during rehabilitation training (E. Q. Yumbla et al. 2021). Gait sensing is required to monitor the user's state and determine when to provide assistance. Commonly paired with gait sensors and gait retraining, haptic feedback is a common method used to adjust and improve the gait of participants and recovering patients (Shull et al. 2011; Chen, Haller, and Besier 2017; Lurie et al. 2011). However, most wearable devices require individual instruments for the sensor and the haptic actuator. Realizing the benefit of mutually sensing and providing haptic feedback to the users, there is a need to develop compact devices with the capability to perform both.

One popular approach for gait sensing is by measuring the ground reaction forces (GRF) on the foot through embedded sensors in a shoe insole. Gait sensors can be categorized based on the sensing mechanism used, namely resistive, capacitive, inductive, optical and soft pneumatic sensors (J.-L. Chen et al. 2022). Among all these sensing mechanisms, only soft pneumatic sensors have the mechanical capability to generate force. In addition, soft pneumatic devices have the advantages of high compliance, simple fabrication, and low cost.

Soft pneumatic sensors have been used for sensing curvature (H. Yang et al. 2017), size of objects (Y. Chen et al. 2018), and external forces (Navarro et al. 2019). Despite many applications of soft inflatable sensors, their use in insole sensing is limited. A previous work explored the use of coiled silicone tubing to measure GRF for gait sensing (Kong and Tomizuka 2009). Fabrication of such sensors is complex and requires re-calibration prior to use.

The most common form of haptic feedback is through vibration motors. These motors can relay commands through physical sensations that a user can understand and execute, such as commands from a therapist to a patient during rehabilitation training. Several studies have demonstrated that using vibration motors has important implications in the recovery of patients (Shull et al. 2011; Chen, Haller, and Besier 2017; Lurie et al. 2011). However, vibration motors are typically manufactured with metal rigid materials, which leads to a heavy and bulky design. This is a significant limitation, as patients with neuro-muscular disorders have weakened muscles and diminished volitional control (Balaban and Tok 2014).

Recently a new form of haptic feedback has been introduced through soft pneumatic actuators. Using laminated bladders and a textile shell, soft pneumatic actuators were created to provide haptic feedback to a participant's lower limb (Afzal et al. 2016). Like with vibration motors, participants were able to identify when the haptic feedback was provided. However, this implementation required additional hardware (footswitches and motion sensors), which increases the complexity of the system.

While studies have shown the necessity for gait sensing and haptic feedback in rehabilitation, there does not exist an integrated and adjustable wearable device which can perform both functions. In order to advance the research in robot-based rehabilitation, more availability of low-cost, lightweight and safe sensor-actuator devices is required. Motivated by the needs of such devices in neurorehabilitation, this Chapter proposes a fabric-based Inflatable Soft Haptic Sensor (ISHASE) to measure GRFs and provide haptic feedback to the foot. The foot was chosen as the target location since the GRFs directly relate to gait, and the foot has a comparable haptic identification performance to more commonly use locations such as the hand (Gurari et al. 2009). Through experiments, we demonstrate that our device is capable of

performing both actions: sensing the user's gait and providing haptic feedback during gait training. This is a unique feature that has significant implications in a physical rehabilitation scenario, as demonstrated through a case study.

3.3 Working Principle

3.3.1 Sensor Working Principle

The working principle of the sensors is based on the property that a change in the volume of a sealed inflated chamber causes a change in internal pressure, according to Boyle's law (3.1), where P is pressure and V is volume.

$$PV = constant \tag{3.1}$$

Therefore, an inflated chamber exhibits a change in internal pressure when it is subjected to an external force that causes deformation and change in volume, as depicted in Fig. 3.1. The change in internal pressure can be used to estimate the external force exerted over the chamber.

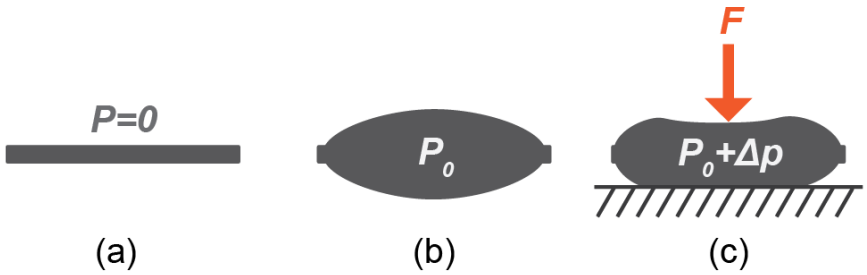

Figure 3.1. Working principle of inflatable sensor. (a) Deflated sensor. (b) Sensor is inflated to P_0. (c) An external force F causes the pressure to increase to $P_0 + \Delta P$.

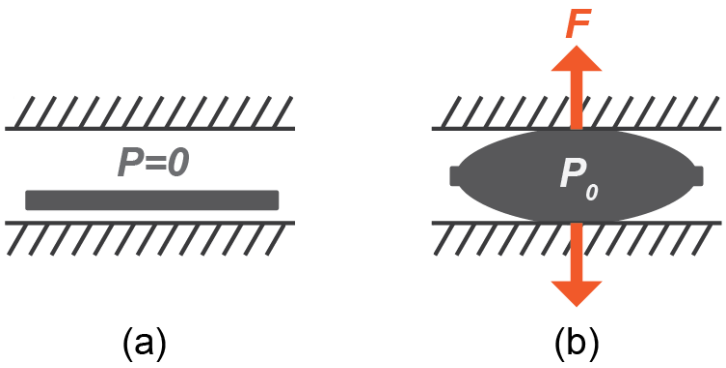

Figure 3.2. Working principle of the inflatable actuator. (a) Deflated actuator. (b) When the actuator is inflated to P_0 it generates a force F.

3.3.2 Haptic Actuator Working Principle

The working principle of the haptic actuator is based on the capability of an inflatable actuator to generate axial force when it is compressed, such as within the insole of a shoe. Consider a deflated balloon that is compressed on both sides, as shown in Fig. 3.2. When the balloon is inflated at pressure P_0, the actuator generates a force F. However, the actual haptic force depends on the compression forces, the distance between the compressing surfaces and the contact area, which are highly variable in soft actuators and therefore require characterization.

Table 3.1. Functional requirements for GRF sensing and haptic feedback.

Maximum Payload	900 N
Dimensions of Sensor	$\leq$ 50 mm $\times$ 50 mm
Height of Insole	$\leq$ 15 mm
Haptic Pressure Intensity	$<$ 50 N/cm^2

3.4 Design and Fabrication

3.4.1 Functional Requirements

The design of the ISHASE is driven by the functional requirements for insole sensing and haptic feedback that are outlined in Table 3.1. The average GRF exerted by a human foot while walking is 900 N (Pollard, Le Quesne, and Tappin 1983). Therefore, the ISHASE is designed with the capacity to measure normal forces up to 900 N. Considering the dimensions of a standard size 9 insole, the maximum length and width of the insole ISHASE are limited to 50 mm. The maximum height of the ISHASE is constrained to match the standard height of a shoe insole, which is approximately 15 mm. (Graven-Nielsen, Mense, and Arendt-Nielsen 2004) identified that the maximum pressure intensity before causing pain is approximately 50 N/cm^2, which sets the requirement for the haptic actuator's maximum force.

Table 3.2. Design Iterations.

W (mm)	L (mm)	H (mm)	chambers	F_{max} (N)
20	20	≥23 *	1	≤450 *
25	25	≥23 *	1	≤450 *
30	30	≥23 *	1	≤450 *
35	35	≥23 *	1	≤450 *
16	70 *	12	1	200 *
16	35	12	2	600 *
16	35	12	3	1000

* indicates functional requirement is not satisfied.

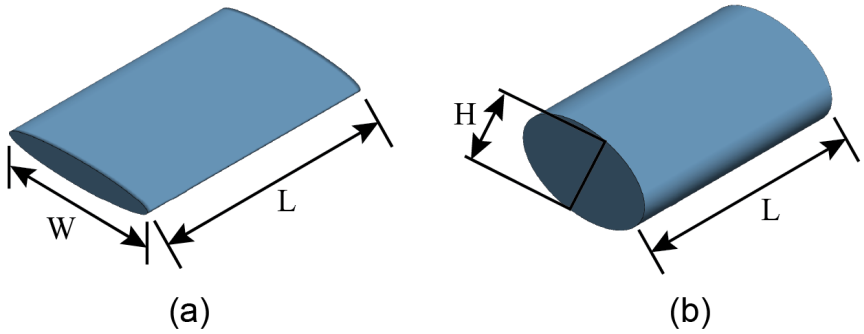

Figure 3.3. Design parameters. (a) Deflated ISHASE with width W and length L. (b) Inflated ISHASE reaches height H.

3.4.2 Sensor and Haptic Actuator Design

The ISHASE was developed through an iterative process. The design parameters are illustrated in Fig. 3.3, and the design iterations are summarized in Table 3.2. To start with, square ISHASE of dimensions 20 mm, 25 mm, 30 mm and 35 mm were manufactured and inflated to an internal pressure of 240 kPa. These designs achieved a minimum height of 23 mm, which did not meet the insole height requirement. To reduce the height to less than 15 mm, the length and width were modified, following a procedure similar to (Nguyen, Sridar, et al. 2019). Through this procedure, we obtained an ISHASE design with 70 mm length and 16 mm width, which failed to

satisfy the dimension requirement. To keep the same height and decrease the length, the ISHASE's length was cut in half (35 mm).

To verify the design satisfies the range of force measurement, compression tests were performed on the ISHASE using a Universal Testing Machine (UTM) (Instron 5944, Instron Corp., High Wycombe, United Kingdom), as shown in Fig. 3.4. A chamber size of 35 mm by 16 mm was used for this test. Different ISHASE configurations were tested with a single chamber, double chambers, and triple chambers, as summarized in Table 3.2. The compression test results, shown in Fig. 3.4, reveal that the single and double chamber designs fail at approximately 200 N and 600 N loads, respectively. The triple chamber is the only configuration that demonstrated the capacity to withstand forces up to 900 N which satisfies the functional requirements.

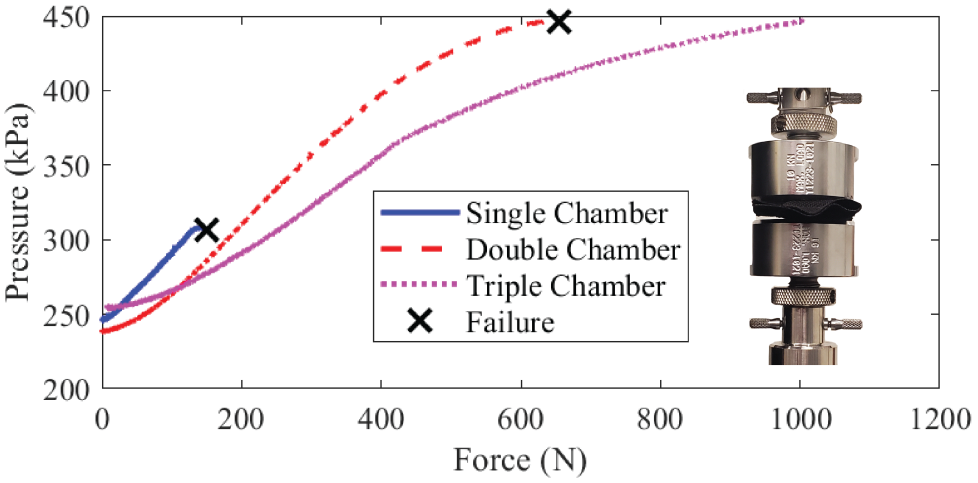

Figure 3.4. Force testing for multiple chambers. The picture shows the ISHASE between the UTM compression plates.

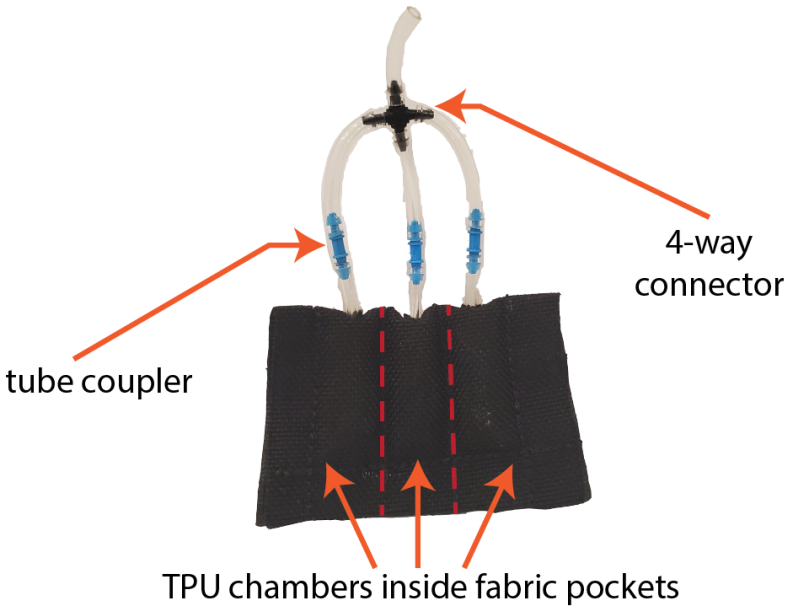

Figure 3.5. ISHASE design overview. The dashed lines depict the stitch line that separates the three chambers.

3.4.3 Fabrication

The fabrication methodology adopted for the ISHASE is as follows. First, the dimensions of each chamber are drawn on two thermoplastic polyurethane (TPU) layers. In the middle of each layer, a small orifice is created to insert a small plastic tube for airflow and pressure measurement. The tube is glued from both sides to create a leak-proof seal. The sides of the TPU layers are then heat-sealed to create a hollow inflatable chamber. Finally, the TPU chamber is placed inside a nylon fabric pocket, made by sewing together two layers of nylon fabric. The dimensions of each nylon pocket are 1 mm smaller than the TPU chamber to avoid stretching of the TPU layers when inflated. Adding the reinforcement nylon fabric increases the structural stiffness which allows the ISHASE to sustain high pressures. The fabrication process is similar to the methodology in (Nguyen and Zhang 2020).

The final ISHASE design is presented in Fig. 3.5. This design consists of three 16 mm-by-35 mm chambers that are sewn parallel to one another. The overall dimension of the ISHASE is 48 mm by 35 mm, and achieves a height of 12 mm when inflated. A four-way barbed connector is used to connect all three chambers to a pressure sensor and to a compressed air source for inflation. To create a leakproof sensor, a one-way valve was connected.

3.4.4 Shoe and Insole Design

The shoe design, presented in Fig. 3.6(a), contains the ISHASE that measures GRFs. Four ISHASE were placed under the insole of the shoe, and positioned at the heel, toe, between the first and second *metatarsophalangeal* joint (Meta12) and between the fourth and fifth *metatarsophalangeal* joint (Meta45), as depicted in Fig. 3.6(b). With this shoe design, the total GRF can be estimated by adding the readings of the four insole sensors. The ISHASE were packed between two thin acrylic sheets to minimize the effect of the unmodeled shear forces and the losses

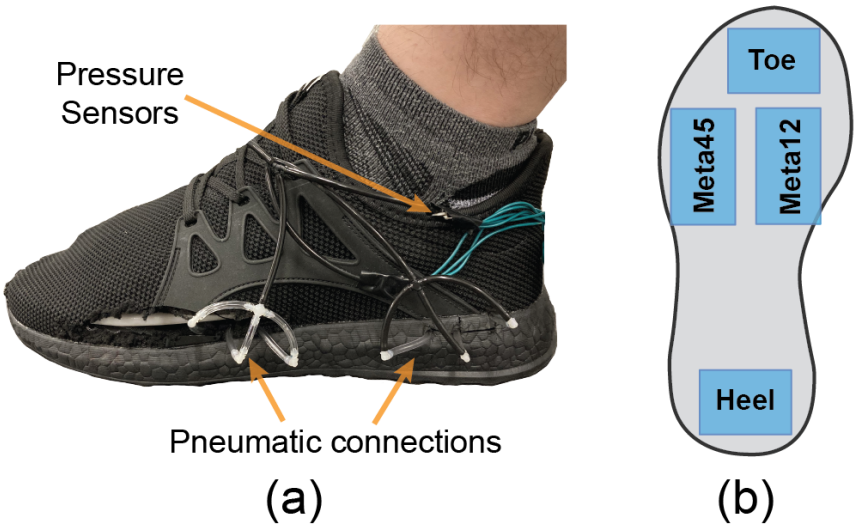

Figure 3.6. (a) Shoe with embedded inflatable sensors-actuators. (b) Sensor placement on the insole.

due to partial contact with the shoe (instead of the insoles). Holes were cut on the sides of the shoe for the sensor's tubing connections. An air compressor provides the pressure source to inflate the ISHASE. Pressure sensors (ABPDANN100PGAA5, Honeywell International Inc., Charlotte, NC) were connected to measure the ISHASE's internal pressure. Solenoid valves (MHE3-MS1H valves, Festo, Eatontown, NJ) were used to operate the inflation and deflation process. A microcontroller (Arduino Uno, Arduino) was used to record the sensor data and to control the haptic actuators. The microcontroller and electro-pneumatics were placed in an off-board unit that weighs less than 3 kg and measures $10 \times 10 \times 5$ cm. As a result, the majority of the system is designed to be wearable. However, due to the air compressors, the experiments are currently limited to a treadmill environment.

3.5 Modeling and Characterization

3.5.1 Sensor Modeling and Characterization

The sensor model, which maps the relationship between external forces and internal pressure, was built through experimental characterization. This model allows estimation of external forces by measuring the internal pressure. Dynamic characterization of the ISHASE's was performed through compression tests using a UTM. The ISHASE was pre-inflated to 200 kPa and then compressed in the UTM for 12 consecutive cycles while collecting data on the applied force and the internal pressure change. A pressure sensor was connected to the ISHASE to measure the internal pressure. Different loading rates were implemented in the UTM as it relates to variations in walking speed.

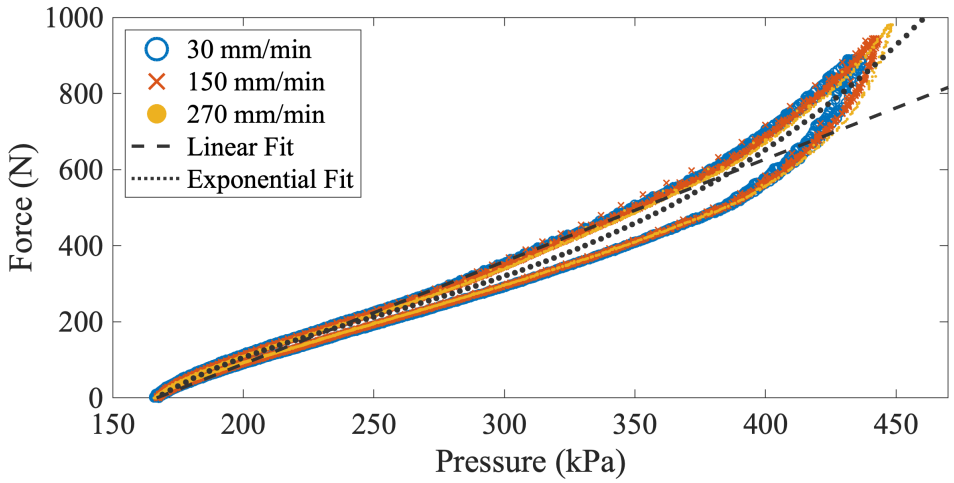

Figure 3.7. Sensor modeling and characterization.

The force-pressure curve in Fig. 3.7 reveals a proportional relationship with some linear or exponential trend. Variations in speed did not have a significant effect on the characterization curve, therefore, only the 150 mm/min data was used to build the model. A linear model (3.2) and an exponential model (3.3) were fitted (linear: R^2 = 0.976, RMSE = 28.4 N; exponential: R^2 = 0.988, RMSE = 19.75 N) between the applied force F and the internal pressure P. In these controlled experimental conditions, the exponential model (3.3) demonstrated better fit performance.

$$F = 2.688P - 448.3 \tag{3.2}$$

$$F = 39.7e^{(0.007P)} - 8686e^{(-0.0253P)} \tag{3.3}$$

An additional data set was collected at 150 mm/min for model validation. The validation for the linear model (3.2) and the exponential model (3.3) yielded a root mean square error (RMSE) of 35.3 N and 22.8 N respectively, which corresponds to a

maximum 3.9 % error of the full-scale range (900 N). Hysteresis between loading and unloading can be observed in Fig. 3.7, which could contribute to the modeling errors.

3.5.2 Sensor Repeatability

Repeatability demonstrates the capability of a sensor to maintain robustness through multiple cycles. The standard deviation of the ISHASE's force estimate will be used as the metric for repeatability. Cyclic compression of the ISHASE was performed in a UTM for 40 cycles while collecting force data. Different loading rates were implemented in the UTM as it relates to variations in walking speed. The peak force for each cycle was recorded and its standard deviation was computed, yielding 5.2 N, 2.8 N and 3.2 N for loading rates of 30 mm/min, 150 mm/min and 270 mm/min, respectively. Considering the ISHASE's full-scale measurement range (900 N), the standard deviation results imply that for the worst case (5.2 N) the ISHASE is repeatable within 99.4% of the sensor full-scale range. The results demonstrate that the ISHASE has exceptional repeatability that is robust to different speeds.

3.5.3 Haptic Actuator Characterization

The force output of the haptic actuator was characterized to quantify the amount of force delivered to the human and to verify that it is within a safe range that does not cause pain. The ISHASE was placed in a UTM between two compression plates, similar to the picture in Fig. 3.4. Different preload conditions were tested to represent the compression forces of the user's foot over the ISHASE while it provides haptic feedback. Preload conditions of 250 N, 350 N and 450 N were tested, which correspond

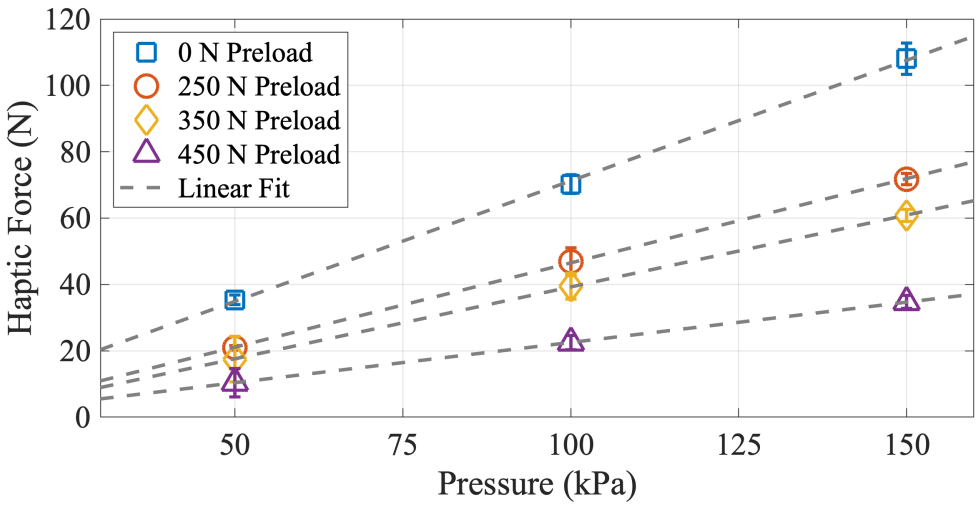

Figure 3.8. Haptic force characterization. For each case, the average and standard deviation of 40 samples is shown.

to subjects that weigh 500 N, 700 N and 900 N, respectively. The ISHASE was inflated at different pressures and the haptic force generated was recorded. Approximately 40 force samples were collected for each preload and pressure condition.

The average force data for each pressure and preload condition are shown in Fig. 3.8. The results corroborate that at the maximum pressure tested (150 kPa) the ISHASE generates sufficient force to be detected (110 N), and delivers a pressure intensity of 6.5 N/cm^2 which is below the pain threshold. In addition, the results reveal that an increase in the preload compression leads to a reduction in the delivered haptic force. This implies that for heavier subjects the delivered haptic force is diminished. However, the ISHASE exhibits the capability of providing sufficient force feedback to be detected by even the heaviest user tested (900 N).

3.6 Evaluation With Human Subjects

The ISHASE were tested with human participants to evaluate the capability for gait sensing and providing haptic feedback to a user. Four healthy participants (74.9 $\pm$ 16.1 kg, 1.73 $\pm$ 0.15 m, 26 $\pm$ 3.9 years, three male and one female) were recruited. The experimental protocol was approved by the Arizona State University Institutional Review Board (IRB ID: STUDY00011110).

3.6.1 Sensor Evaluation for Gait Sensing

The goal of this experiment is to use the ISHASE to estimate the total GRF of a human while walking. Each participant wore the ISHASE-embedded shoe, shown in Fig. 3.6, while walking on an instrumented split-belt treadmill (Bertec Inc., Columbus, OH) equipped with two force plates that measure the GRF at 1,000 Hz, which were used as ground truth. The participants walked for approximately 100 steps at a speed of 0.5 m/s and 0.75 m/s. The GRF data for each walking trial was segmented into individual gait cycles. The 100 segmented gait cycles were temporally normalized to gait cycle percent to compute the GRF average and standard deviation through the walking cycle.

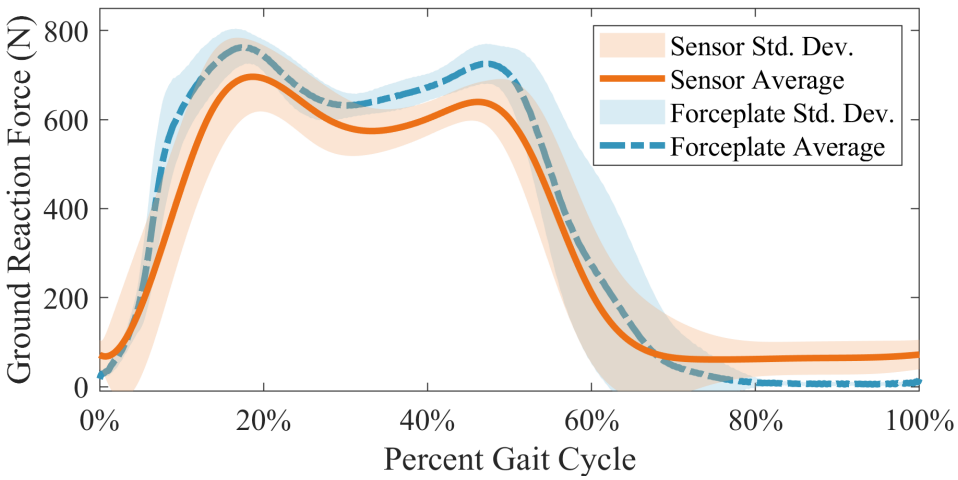

Figure 3.9. GRF of the human participant while walking. The sensor GRF was obtained with the linear model (3.2).

Table 3.3. RMSE of GRF estimation at different walking speeds.

		Linear Model (3.2)		Exponent Model (3.3)	
Subject	Weight	0.5 m/s	0.75 m/s	0.5 m/s	0.75 m/s
1	82.5 kg	94.9 N	100.9 N	135.5 N	114.8 N
2	88.1 kg	93.3 N	100.8 N	122.3 N	96.66 N
3	51.7 kg	64.9 N	74.28 N	71.60 N	107.7 N
4	77.3 kg	90.4 N	70.99 N	89.43 N	89.37 N

The GRF average and standard deviation for one participant while walking are shown in Fig. 3.9. The ISHASE's RMSE of the GRF estimation are presented in Table 3.3. The results demonstrate that ISHASE can accurately estimate GRF with a maximum of 91% accuracy (70.99 N RMSE corresponds to 9% of Subject 4's body weight) and a minimum of 85% accuracy (74.28 N RMSE corresponds to 15% of Subject 3's body weight). A possible source of error could be due to friction of the foot on the inner sides of the shoe, which suggests that not all forces are transmitted to the insole; this effect is most noticeable during the stance phase (0-60% gait cycle). In the swing phase, the error is because when the shoe is worn there is compression

pressure due to the tightening of the shoe laces, which is not accounted for in the individual sensor model.

The human subject experiments revealed that the linear model (3.2) achieves better estimation performance than the exponential model (3.3). Exponential fits can be highly sensitive to outliers in the data. In the subject experiments, there is a significant presence of unknown disturbances, such as shoe friction and compression forces, which introduce outliers. As such, the exponential model tends to amplify errors related to unknown disturbances that surfaced during the subject experiments. Lastly, the exponential model could be overfitting the undisturbed and noise-free data (Fig. 3.7), and as a result, it might not perform well for data with unknown disturbances and noise. In contrast, the linear model is simpler and makes fewer assumptions, and therefore can be more robust to variations caused by unknown disturbances and noise.

3.6.2 Haptic Feedback Evaluation

The goal of this experiment is to demonstrate that the human user can identify the sensation of the haptic feedback from ISHASE. Each participant wore, on the left foot only, the ISHASE-embedded shoe in Fig. 3.6(a), and was asked to identify where the haptic feedback was delivered under the foot. To provide haptic feedback, the ISHASE was inflated and deflated rapidly at a fixed frequency to induce a vibratory sensation. Different frequencies (10 Hz and 100 Hz) and different inflation pressure (50 kPa and 100 kPa) were tested. Each trial consisted of 50 rounds of feedback at randomized locations, and each round lasted 0.5 sec.

Table 3.4. Success Rate of Haptic Feedback Identification for Subject 4.

	100 kPa	50 kPa
10 Hz	98%	92%
100 Hz	96%	82%

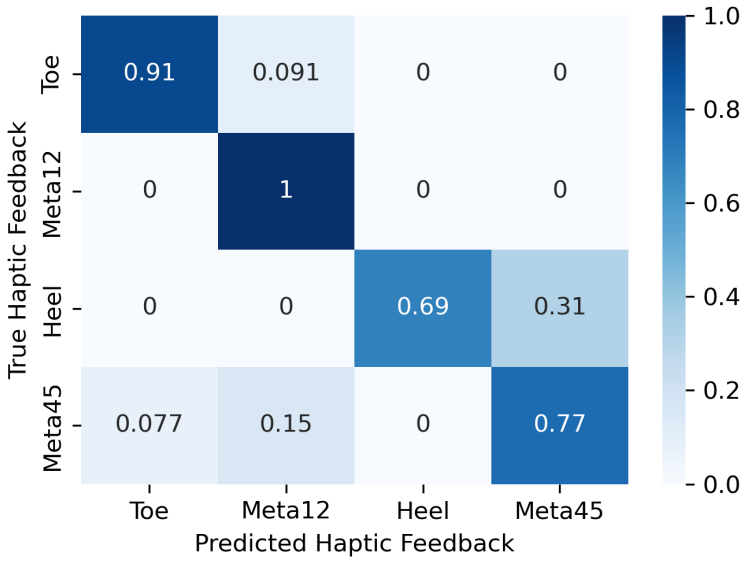

Figure 3.10. Confusion matrix of haptic feedback identification for trial with lowest performance (100 Hz and 50 kPa).

The haptic results presented correspond to a representative subject (Subject 4). The overall success rates for different frequencies and inflation pressures are summarized in Table 3.4. The confusion matrix of the lowest performing trial (100 Hz, 50 kPa) are shown in Fig. 3.10. The results demonstrate the user is capable of sensing the haptic feedback and even identifying its location. The results revealed that low frequencies contribute to an improvement in haptic feedback identification. One possible reason is that, at a lower frequency, the actuator can fully inflate and provide high force. Higher pressures also improved the haptic feedback identification, due to a similar reason.

3.6.3 Case Study for Sensing with Haptic Feedback

In this section, we present a case study that demonstrates the use of the ISHASE's dual capability for sensing and providing haptic feedback in a rehabilitation task. A common rehabilitation scenario involves a human performing physical activity while a therapist monitors and gives commands. In our case, the physical activity is sit-to-stand transition, and all commands from the therapist to the user will be provided through the shoes in Fig. 3.6(a). As such, this experiment focuses on using the ISHASE to simultaneously estimate the human states and provide the haptic feedback to guide the user.

The participants were guided to transition between sitting down and standing up when they feel the haptic feedback. The transitions between sitting down and standing up are monitored with the ISHASE's GRF measurements. The transitions to standing up are detected when the GRF measurement exceeds a threshold that is determined before the start of the experiment (GRF>325 N for Subject 1). Once a transition is detected, a randomized delay is introduced before the next haptic feedback (indication) is provided. The experiment had a duration of 7 min.

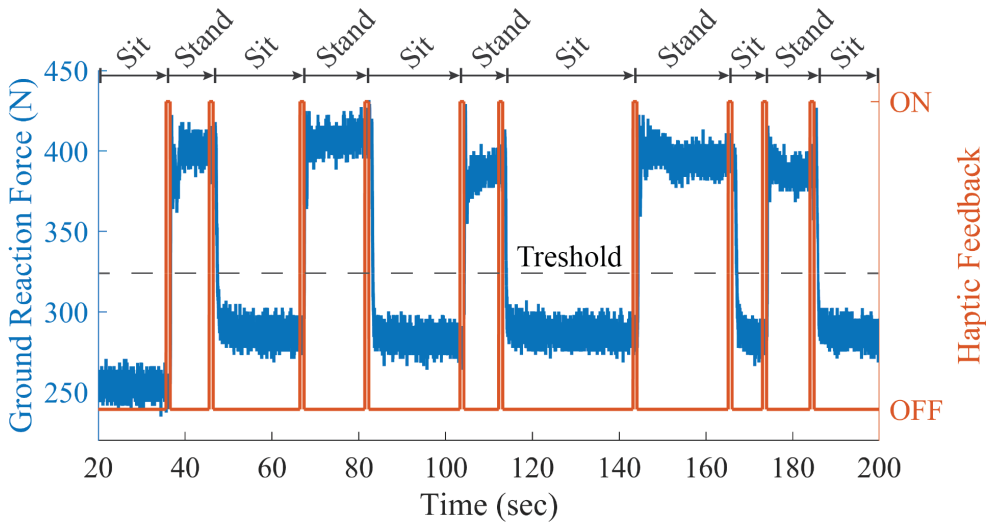

Figure 3.11. Sensor GRF measurements and haptic actuation signal through the case study experiment.

Fig. 3.11 shows the ISHASE's sensor and actuation signals for a representative subject (Subject 1). This plot shows that the ISHASE-embedded shoe is capable of accurately detecting the transitions between sitting down and standing up. In addition, the results show that every time haptic feedback is delivered, the user immediately captures and reacts to it. This serves as preliminary evidence that the therapist can send commands, through the shoe, to modify or engage in physical activity of the patient. This could allow the therapist to focus on adjusting gait or training parameters during rehabilitation since the developed ISHASE takes care of the real-time monitoring and signaling to the user.

3.7 Conclusion

This Chapter introduced a soft inflatable device to perform mutual gait sensing and haptic feedback. The development of the ISHASE addressed a gap in the availability of devices that can perform both actions. The ISHASE's design, fabrication, modeling and mechanical characterization were discussed in detail. Four ISHASE were embedded into a shoe insole to monitor gait and provide haptic feedback to the user's foot. The sensor model was developed with experimental data and achieves an accuracy of 35.3 N (3.9% error of the sensor's full-scale range). In practical applications, the ISHASE demonstrated the capacity to accurately estimate the GRF of a user while walking, with a maximum and minimum accuracy of 91% and 85% respectively. The ISHASE was also evaluated as a haptic device, and the results reveal that the users can identify the haptic feedback location. Furthermore, the application of the ISHASE as a mutual gait sensor and haptic actuator was explored through a case study that exemplifies a physical rehabilitation scenario. The case study demonstrated that the ISHASE can be used to autonomously monitor the state of the human while simultaneously provide indications to the user through haptic feedback.

Future work will include improving the design to ensure robustness for extended use. The sensor model will be improved to account for unmodeled compression forces within the shoe, and the unmodeled forces that are lost due to friction with the shoe. Furthermore, we aim at performing mutual sensing and haptic feedback by developing a dynamic estimation model that robustly estimates external forces in the presence of dynamic pressurization. Lastly, a detailed study with a greater number of participants will be conducted.

Chapter 4

EVALUATING THE BENEFITS OF A SOFT INFLATABLE KNEE EXOSUIT DURING SQUAT LIFTING

4.1 Abstract

This study aims to utilize a soft-inflatable exosuit to provide knee extension assistance during squat lifting and study the kinematics of the hip, knee, ankle, and lumbar joints as well as the surface electromyographic (EMG) activity of the muscles created around these joints. This work will provide preliminary data to refine the design, control, and evaluation of wearable soft robots to maximize their benefits in repetitive and labor-intensive tasks. We hypothesize that adding an external torque to the knee joint using a soft inflatable exosuit can potentially induce a reduction in the muscular effort that extends to the posterior chain muscles.

The functional requirements for lifting tasks were investigated to guide the design of the exosuit and the soft inflatable actuators. The soft actuators were characterized to corroborate that the design achieves the minimum torque requirements. A total of 8 healthy test participants are recruited and instructed to lift a weight equivalent to 10% of their bodyweight. The muscle activities of the left and right Vastus Lateralis, Biceps Femoris, Gluteus Maximus, Erector Spinae (Iliocostalis and Longissimus) and Multifidus muscle groups were studied for baseline, non-assisted, and assisted conditions. The majority of participants (6 out of 8) demonstrated consistent reduction in the muscular effort of at least one muscle group of the posterior chain. A maximum reduction of 55% in the average muscle activity of the Multifidus muscle group is

observed in one participant. Different neuromuscular adaptation mechanisms were observed among subjects that ultimately led to a reduction in lower-limb or back muscle activity. The results reveal that assisting knee extension during a lifting task has significant effects on muscle activity with benefits that extend to the posterior chain muscles. This study provides early evidence that the soft inflatable knee exosuit can be used in material handling tasks to reduce muscle effort and prevent work-related injuries.

4.2 Introduction

Manual material handling (MMH) involves lifting, carrying, and lowering heavy weights on a daily basis. These tasks put significant loads on the knees, hips, and

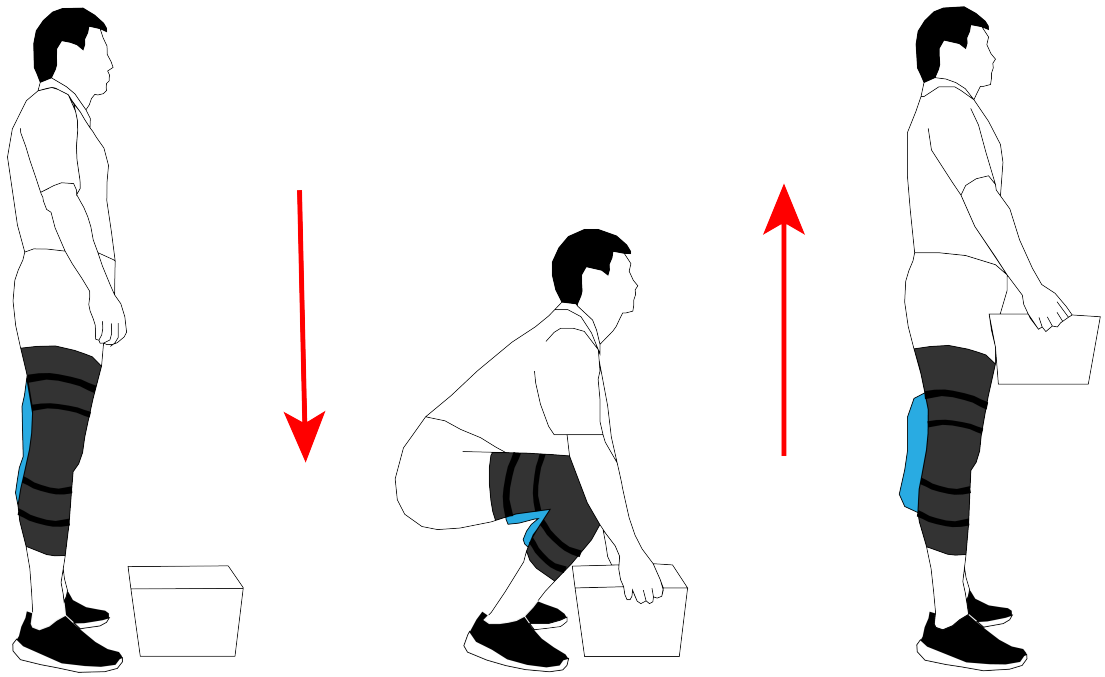

Figure 4.1. Illustration of the Study Concept: Investigate the Effects of Lower-Limb Assistance with an Inflatable Soft Exosuit During Squat Lifting Tasks.

lower backs of the workers, which may increase the risk of developing work-related musculoskeletal disorders (MSDs) (Antwi-Afari et al. 2017). In fact, more than 42% of lower-limb injuries in the physical workforce are caused by over-straining and exertion, and prior work has found significant correlations between knee osteoarthritis and prolonged squatting and lifting weights (Amin et al. 2008). As a result, a large number of self-reported sick leaves among these workers are due to MSDs (Hubertsson et al. 2014). Work-related injuries reduce the quality of life of workers and lead to increased costs of operation. It was reported that MSDs alone led to $1.5 billion direct cost in 2007 in the United States (Bhattacharya 2014).

In recent years, the use of wearable robotic systems to assist in physically strenuous tasks has been on the rise. Typically, these wearable devices can be divided into passive wearable devices (Maurice et al. 2019; Alemi et al. 2019; Lamers, Yang, and Zelik 2017) which utilize energy storage mechanisms such as springs and elastic bands to store and release energy, and active systems (Jeong, Woo, and Kong 2020; Sado et al. 2019; Toxiri et al. 2019) which generate force/torque to provide physical assistance. Passive systems have demonstrated the efficacy of use in MMH tasks by demonstrating reduced muscle activities and fatigue levels over several trials, but they can only provide pre-defined assistance profiles (Baltrusch et al. 2018). To overcome the aforementioned issue, several groups have developed wearable robots that provide active assistance to the knee, hip and lumbar joints during lifting (Jeong, Woo, and Kong 2020; Sado et al. 2019). Most wearable robots found in the literature are rigid exoskeleton systems that provide variable and controlled assistance, but they can be bulky, heavy, and expensive (Toxiri et al. 2019).

The recent development in wearable soft robots provides a novel solution to mitigate the challenges of their rigid counterpart. These robots are typically composed

of lightweight and compliant materials (e.g., textiles) to overcome the limitations of heavy and bulky exoskeletons (E. Q. Yumbla et al. 2021). Soft exosuits driven by cables (for the hip and lumbar joints) (Yao et al. 2019; S. Yu et al. 2019) and pneumatic artificial muscles (for the knee joint) (Mohri et al. 2016) have demonstrated reduced muscle efforts for the corresponding joints when assisting in a lifting task.

In our past work, a fabric-based soft-inflatable exosuit has been developed to provide knee extension assistance (Saivimal Sridar et al. 2018). The benefits of this soft exosuit have been demonstrated in assisting healthy individuals (Saivimal Sridar et al. 2018) and stroke survivors (S. Sridar et al. 2020) in walking experiments. However, these previous studies on healthy individuals focused only on walking tasks, restricted the analysis to muscles that interact directly with the knee joint, and did not include the muscles and kinematics of other joints involved in the task. The effect of adding an external torque to the knee joint during a closed-chain kinetic task on the adjacent joints is still unknown. During squat lifting, the knee, hip, and back muscles contract in order to raise the weight along with the center of mass of the human (Vakos et al. 1994). Since lifting heavy objects from the ground requires coordination and synergy of the back, hip, knee, and ankle muscles (Roozbazar 1974), assistance to the knee joint during squat lifting may also alter the activity of all the muscles involved in performing the task at hand. Therefore, it is important to understand how humans adapt to the assistive torque provided to a single joint during this complex movement and how this external torque impacts the muscle efforts of other joints. To the best of our knowledge, it is still unclear how knee joint assistance propagates to the posterior chain muscles in a closed kinematic task such as lifting.

This study aims to utilize the previously designed soft-inflatable exosuit to provide knee extension assistance during squat lifting and study the kinematics of the hip,

knee, ankle, and lumbar joints as well as the surface electromyographic (EMG) activity of the muscles around these joints. This study will provide preliminary data to refine the design, control, and evaluation of wearable soft robots to maximize their benefits in repetitive and labor-intensive tasks.

4.3 Development of the Soft Exosuit

4.3.1 Functional Requirements

The biomechanics during lifting tasks were investigated to determine the functional requirements for actuator design. A study by Hwang et. al. (Hwang, Kim, and Kim 2009) reported the human biomechanics when performing a squat down and lifting an object from the floor. Results showed that the knee extension peak torque for this task was 0.5 Nm/kg. As an assistive device, a partial support equivalent to 50% of this peak torque was selected as the target assistance. The required torque for each subject was computed using the results from this study and are presented in Table 4.1.

Table 4.1. Subject participants' anthropometric data and joint torque requirement.

Subject	Gender	Age	Weight (kg)	Height (m)	Torque (Nm)
S1	F	23	65.7	1.57	16.43
S2	M	27	78	1.65	19.50
S3	F	27	55	1.54	13.75
S4	M	31	75.4	1.70	18.85
S5	M	25	78	1.72	19.50
S6	M	22	75.5	1.70	18.88
S7	F	27	55	1.58	13.75
S8	M	22	74.5	1.80	18.63
Mean		25.5	69.6	1.66	17.41
Standard deviation		3.12	9.82	0.09	2.46

This study also defined the timing of knee joint peak torque as the instance when the human is in the lowest position of the squat, during maximum joint flexion with knee angles greater than 90°.

4.3.2 Design of the exosuit

To generate torque to assist the human knee joints, soft pneumatic inflatable actuators were designed to satisfy the requirement in Section 4.3.1. The actuators are fabricated using heat-sealed thermoplastic polyurethane (TPU) films encased in an inelastic nylon fabric reinforcement, presented in Fig. 4.2. When deflated, the actuator is completely compliant and exerts no torque on the wearer. When the

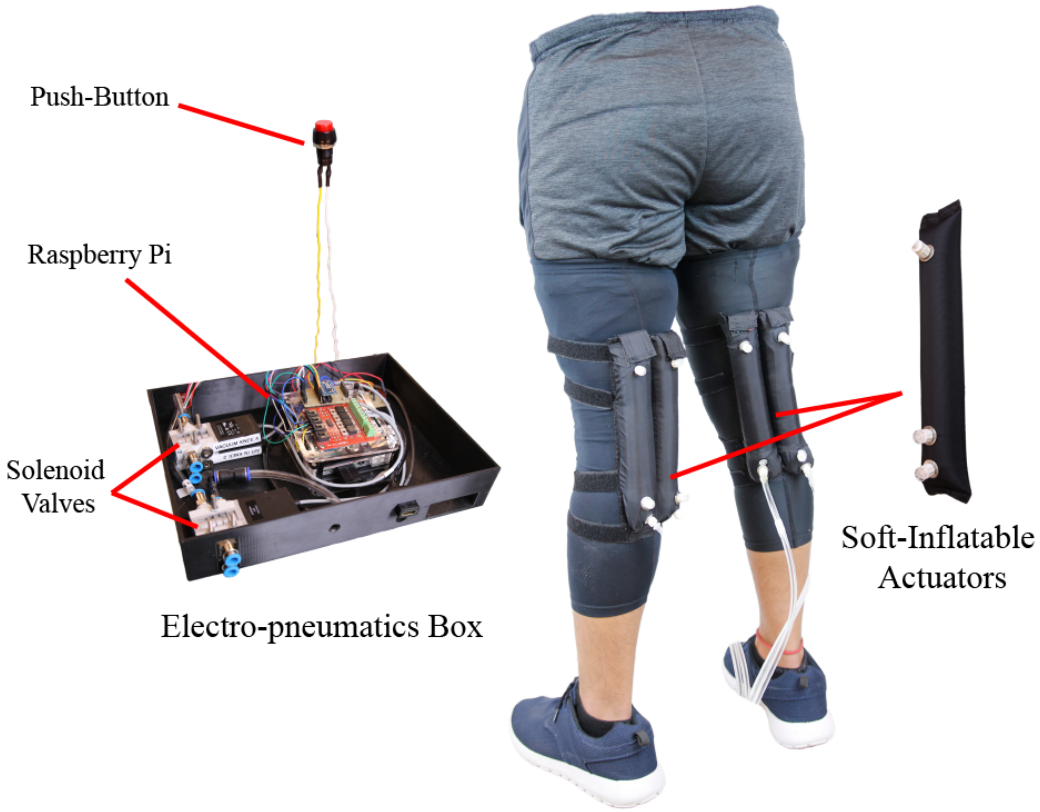

Figure 4.2. The soft-inflatable exosuit system worn by a human subject. The system is composed of two soft-inflatable actuators for each leg, solenoid valves, Raspberry Pi, and a push-button.

inflatable actuator is bent and pressurized, it generates a restoring torque that forces the actuator to the straight position. This mechanical principle was utilized to provide torque to the human joints. More details on the design and development of the soft-inflatable actuators can be seen in (Saivimal Sridar et al. 2018).

An overview of the soft exosuit system is presented in Fig. 4.2. The exosuit consists of an elastic neoprene sleeve that conforms to the thigh and shank at the knee joint. Two pneumatic inflatable actuators are placed at the popliteal fossa to provide extension torque to the knee joint. Nylon fabric pockets were sewn into the sleeve to hold the actuators in place securely. We utilized hook and loop straps to ensure proper transmission of the assistive forces to the lower limbs. The exosuit garment worn by the user weighs 0.13 kg. The soft materials that comprise the exosuit make it lightweight, completely compliant, and transparent to the wearer.

A torque characterization experiment was performed to measure the torque generated by an inflatable actuator. The inflatable actuator was placed on a mechanism that simulates the human knee joint on the sagittal plane. This mechanism, presented in Fig. 4.3, was mounted on a static analog torque sensor (FTA-100NM, Forsentek Co., Limited, China) to measure the torque exerted by the actuator. For the data collection procedure, the analog joint mechanism was fixed at different angles within the knee joint's range of motion, and the actuator was pressurized from 0 to 207 kPa in increments of 34 kPa, and torque was measured at each step. The results of this characterization, presented in Fig. 4.3, exhibit a linear relationship between internal pressure and generated torque at a given angle. This demonstrates the capacity to modulate the assistive torque by controlling the actuator's internal pressure. To satisfy the biological torque requirements for all subjects in Table 4.1, a maximum torque of 19.5 Nm is required. A single inflatable actuator has the capacity to generate 10 Nm

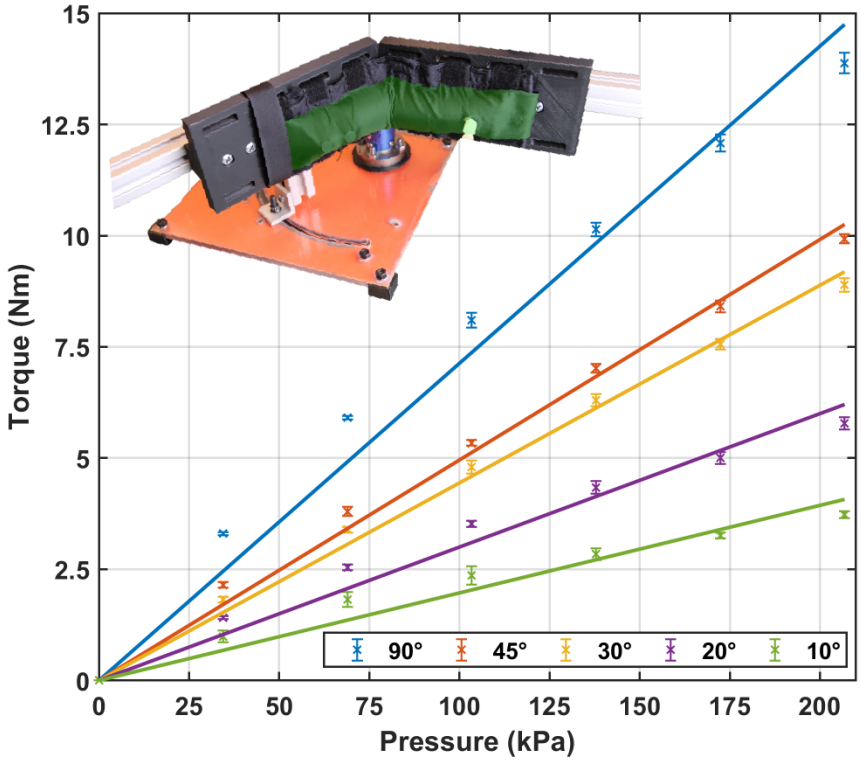

Figure 4.3. Actuator torque characterization results for different operating angles and internal pressure. The characterization platform mounted with the actuator is presented on the top left. The soft-inflatable actuator is highlighted in green, and the torque sensor in blue.

torque inflated at 140 kPa, for joint flexion of at least 90°, which corresponds within the knee joint range of motion during squat lift (Hwang, Kim, and Kim 2009) as indicated in Section 4.3.1. Two inflatable actuators are required for each knee joint to operate the exosuit within safe pressure magnitudes. With this design, the operational pressure will not exceed 140 kPa.

We integrated the electro-pneumatics of the system with a microcontroller (Raspberry Pi). The system consists of solenoid valves (MHE3-MS1H valves, Festo, Hauppauge, NY) to quickly switch between the pressurization and depressurization states of the actuators. A push-button was utilized to send the inflation and deflation commands to the microcontroller. We implemented pressure sensors (ASDXAVX100PGAA5,

Honeywell International Inc., Morris Plains, NJ) to monitor the internal pressure of the inflatable actuators.

4.4 Experimental Protocol

4.4.1 Study Design

For this study, a total of 8 participants (5 male and 3 female) with no history of lower body and back pathologies were recruited. The experimental protocol was approved by the Arizona State University Institutional Review Board (IRB ID#: STUDY00011110). The anthropometric data of the subjects can be seen in Table 4.1. The weight lifted was limited to 10% of their bodyweight to standardize the study across all participants. A plastic box of dimensions $0.40 \times 0.30 \times 0.17$ m^3, contained evenly distributed weights that were adjusted according to each subject's bodyweight. Kinematics and EMG data were collected for three conditions: Baseline (exosuit not worn), Inactive (exosuit worn but not actuated), and Active (exosuit worn and actuated). An independent and identical exosuit was worn on each leg to provide symmetric assistance to the user.

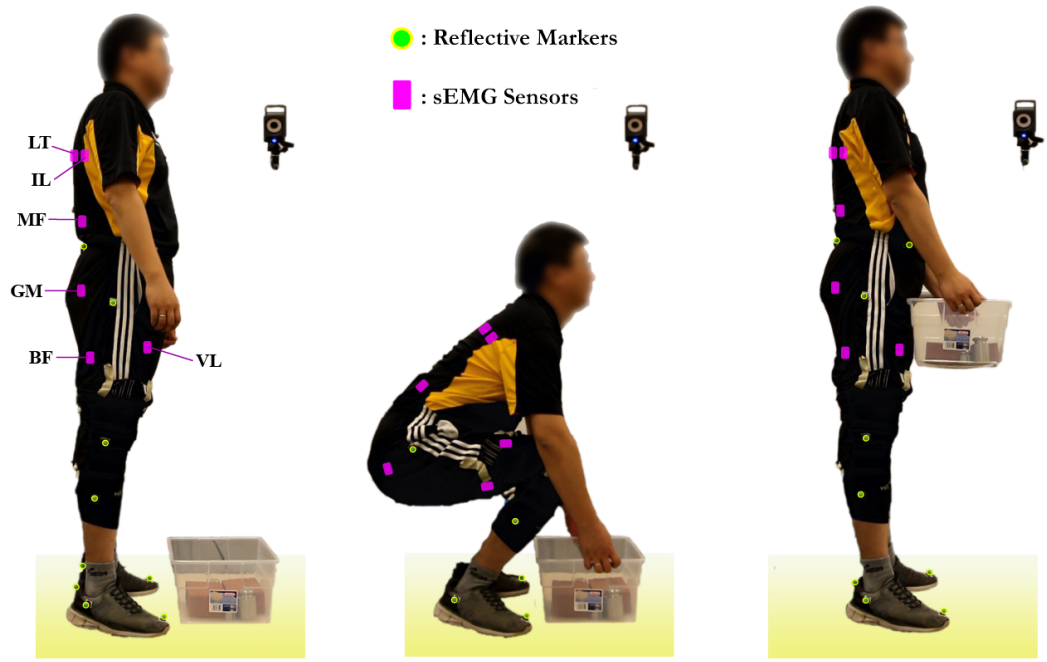

Figure 4.4. Human subject wearing the soft-inflatable exosuit and performing the lifting task. The abbreviations of the muscles investigated are depicted in the left picture. The EMG locations are approximated in the figure as these were placed underneath the clothing. The exosuit is inflated when the participant has reached the lowest position during the squat (middle picture) and assists through the upward lift.

The participants were instructed to start each trial standing upright. Upon a given signal, they would descend, grasp a box, and ascend to the upright position, as illustrated in Fig. 4.4. The ascent and descent for each trial were completed in one second, respectively, controlled using a metronome set at 60 beats per minute. A total of five trials for each condition were performed with each participant. For the active trials, the participants were given a button to inflate the exosuit. The participants were instructed to actuate the exosuit when they reached their lowest position during the squat. By relying on the cognitive skills of the human to choose the ideal timing, the control variables of the exosuit were simplified. The assistive torque from the exosuit was personalized by tuning the actuator pressure according to

the torque requirement in Table 4.1 and the torque characterization results in Fig. 4.3. Between trials, each participant took a 15-min rest to prevent muscle fatigue.

4.4.2 Data Collection

Data collection of kinematics and EMG activity was performed using the experimental setup in Fig. 4.4. The kinematics were collected using a camera-based motion capture system (T40s, VICON Inc., Los Angeles, CA). Passive reflective markers were attached to the lower-body and the torso of each participant according to pre-defined marker sets (Vicon Plug-in Gait) as illustrated in Fig. 4.4. The kinematic data were collected at a sampling frequency of 100 Hz.

The EMG activity of the Vastus Lateralis (VL), Biceps Femoris (BF), Gluteus Maximus (GM), Multifidus (MF), and the erector spinae muscles (Iliocostalis (IL) and Longissimus (LG)) were selected for this study. The aforementioned muscles were investigated since they are highly active during squat lifting. The MF, IL, and LG were investigated in order to study the effects of knee extension assistance on the posterior chain. The EMG data were recorded using a Delsys Trigno (Delsys, Natick, MA) system and sampled at 2000 Hz. The raw EMG data were first de-meaned and band-pass filtered (Butterworth, 4th order, 20 Hz and 450 Hz cutoff frequencies). The profile of the signal was obtained by computing the root-mean-square (RMS) envelope using a moving window of 250 ms. All EMG data were normalized using the maximum EMG values of all collected trials for each respective muscle. The EMG normalization method is valid since all the trials were performed in the same session without sensors being removed. The five lifting cycles for each condition were temporally normalized to percent lift completion and then averaged to determine a

mean and standard deviation of muscle activity. This results in normalized EMG signal as a function of percent lift completion, where 0% corresponds to standing straight right before initiating the squat (Fig. 4.4 left), and 100% corresponds to the finalized lifting of the box (Fig. 4.4 right). The mean and integral of the EMG envelope were computed for five lift cycles, and the statistical significance between each data set was calculated using an independent t-test ($p < 0.05$).

4.5 Results

4.5.1 Kinematic Results

The joint kinematics throughout the lift cycle of two representative subjects are presented in Fig. 4.5. For participant *S1*, the maximum flexion angles of the knee, left hip and right ankle joints increase, indicating an increase in the range of motion for these joints when the exosuit assisted knee extension. This participant squats to the lowest position i.e. the maximum knee flexion angle faster, and stays at this position for a longer duration, as shown in Fig. 4.5a. Participant *S2* shows a similar range of motion and the descending pattern between the two conditions. However, this participant spends less time in the lowest height and completes the lifting earlier when the exosuit is active, as shown in Fig. 4.5b. For both subjects, the maximum joint angles occur close to 40% of the lifting cycle, when the push button was pressed to start inflating the exosuit. This timing matches the initial period when a statistically significant difference in EMG activity is first observed, as discussed in Section 4.5.2.

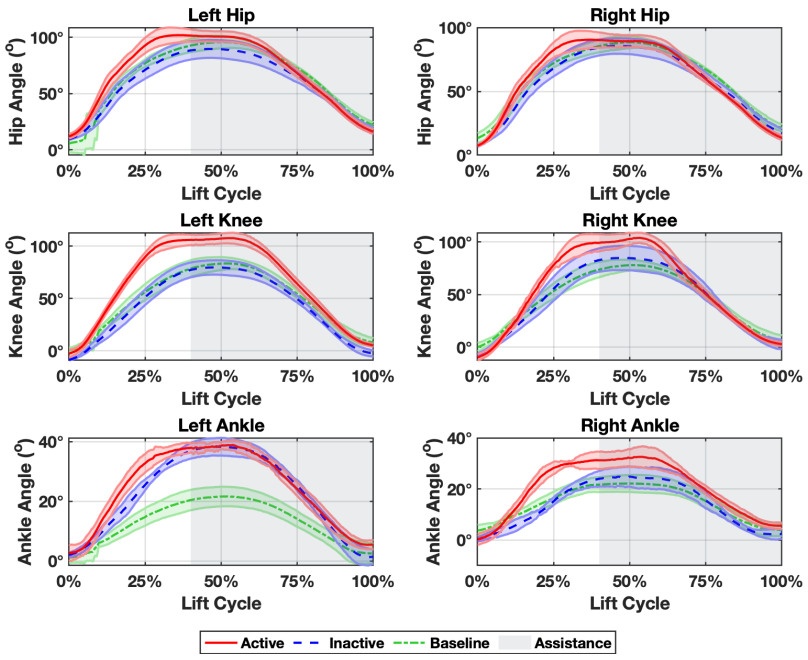

(a) Participant *S1*

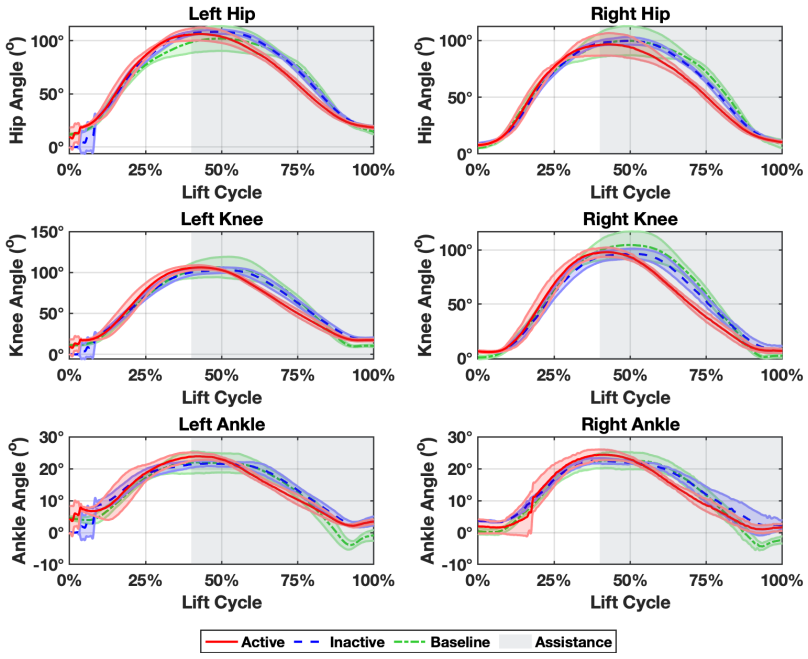

(b) Participant *S2*

Figure 4.5. Sagittal plane joint kinematics of participants *S1* (a) and *S2* (b) through the lifting cycle.

4.5.2 EMG Results

The processed EMG signals throughout the complete lift cycle of participants *S1* and *S2* are presented in Fig. 4.6. The results of the EMG activity for active conditions demonstrated a significant reduction for most muscle groups through the majority of the lift cycle compared to baseline conditions. Participant *S1* demonstrates this reduction in all the back and lower limb muscles through the mid to end of the lift cycle, initiating at approximately 40% of the lift cycle, which corresponds to the assistance onset timing. *S2* also demonstrates a similar reduction of EMG activity for most of the muscles (7 out of 12 muscles). The period when the EMG shows a reduction matches the period when the exosuit assisted the user's knee joints. For both subjects, the greatest reduction was observed in the MF muscles, indicating that the lower back muscles exerted less effort during the lifting task. Furthermore, *S2* demonstrated a shift in the EMG envelope where the active case demonstrated earlier muscular activation levels in the lift cycle, especially from the middle until the end of the cycle. A similar shifted behavior is observed in the joint kinematics profile as discussed in Sec. 4.5.1.

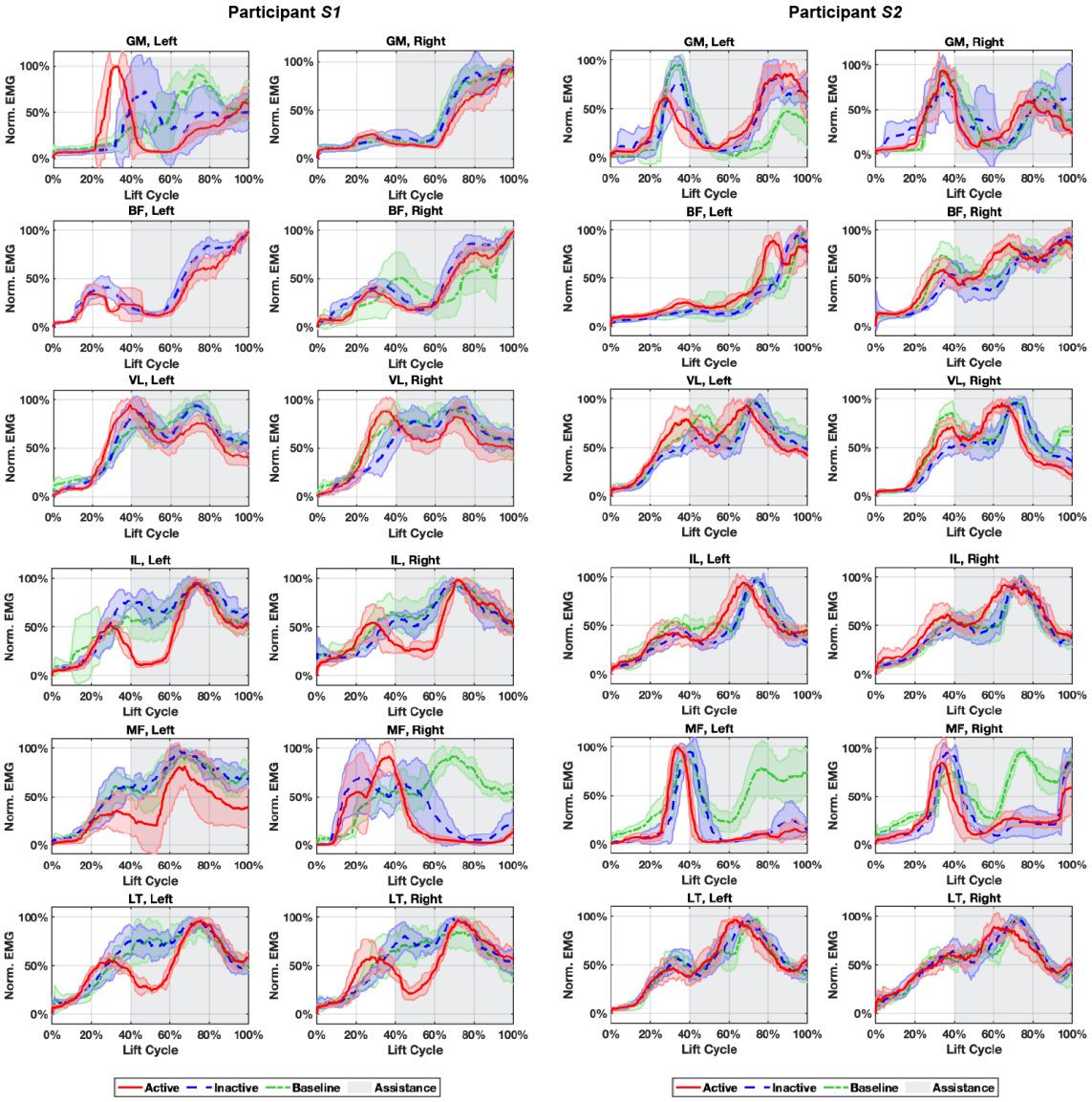

Figure 4.6. EMG activity through the lifting cycle of participant *S1* (left) and participant *S2* (right). The mean and standard deviation for the active case are presented in a solid red line, the inactive case in a blue dashed line and the baseline case in a green dash-dotted line. The period in which the exosuit assisted the knee joints is shaded in gray, approximately from 40% to 100% lift cycle. The baseline data for the left BF of participant *S1* was corrupted and therefore not included.

The integral (area under the curve) of the EMG envelope was computed and is presented in Fig. 4.7. The EMG integral quantifies the total muscular effort through the complete lift cycle. Two types of EMG response patterns were observed in several subjects, shown in Fig. 4.7a-b. The EMG integral of *S1* reveals that all the muscles, except BF, demonstrate a reduced muscular effort when the exosuit supports knee extension compared to the baseline. On the other hand, *S4* demonstrates a reduction in the posterior chain muscles, but an increase in the lower-limbs muscles. It should be noted that the lower-limbs muscles of *S4* also demonstrated an increase when the exosuit was worn but not inactive compared to the baseline, indicating that wearing the exosuit is a possible source of increased muscular activity observed when the exosuit provides extension torque. On average, the subjects demonstrated a significant reduction in the overall effort of the MF muscle when the exosuit provided extension torque (baseline vs. active) as observed in Fig. 4.7c. In addition, an increase in the total muscular effort was observed in a few lower-limb muscles, specifically the VL, left BF and right GM, when the exosuit was worn but inactive (baseline vs. inactive) and when the exosuit provided extension torque (baseline vs. active).

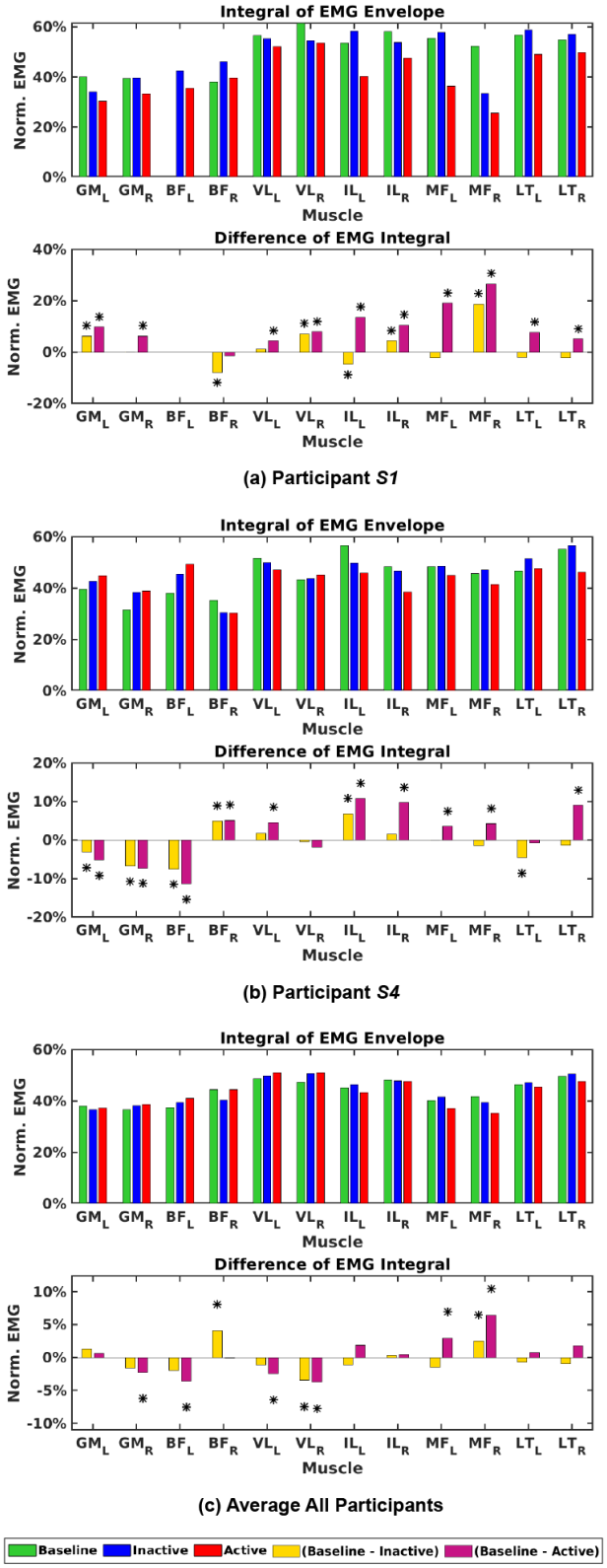

Figure 4.7. Integral of EMG envelope for different conditions (top), and the difference of the EMG integral among conditions (bottom). * indicates statistically significant difference ($p < 0.05$).

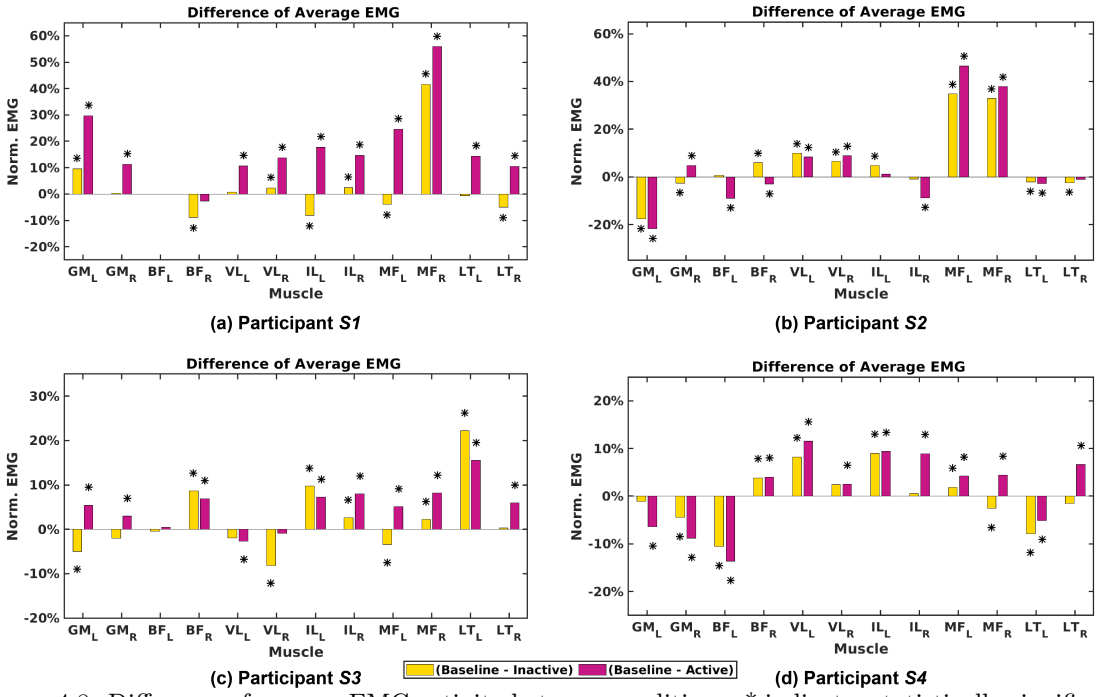

Figure 4.8. Difference of average EMG activity between conditions. * indicates statistically significant difference ($p < 0.05$).

The difference in the average EMG signal between different conditions is presented in Fig. 4.8. This figure illustrates the transparency of the exosuit (baseline vs. inactive) and the mean reduction in EMG activity when the exosuit assists the human's knee extension motion (baseline vs. active). The results reveal that six participants demonstrate a statistically significant reduction in the average muscle activity of both the left and right side of at least one muscle group of the posterior chain when the exosuit provides extension torque to the knee joint (e.g. left and right MF of *S2*). The results of participants *S1*, *S3* and *S4* in Fig. 4.8, show that at least 8 muscles demonstrated a consistent reduction of the average EMG activity when the exosuit provides extension torque. Furthermore, all of the back muscles (IL, MF, and LT) demonstrated a significant reduction in mean EMG activity, with a maximum reduction of 55% for the MF muscle of *S1*. Participants *S2* and *S4* demonstrate an

average increase in the EMG of a few of the lower limb muscles for both cases in Fig. 4.8, which indicates the possibility that the source of increased EMG activity is the exosuit interface.

4.6 Discussion

Knee extension assistance during squat lifting demonstrated minimal alterations to the participants' kinematics. The kinematic profile throughout the lift cycle followed a similar path when the exosuit was active, indicating that the human coordinated with the exosuit assistance to maintain a similar trajectory. This also demonstrates the exosuit's capacity to assist knee extension without significantly altering the natural motion during squat lifting.

The EMG results of all four representative subjects demonstrated the potential for reducing muscular activity during squat lifting tasks when using a soft robotic exosuit that assists the knee extension motion. The results show that the subjects tend to present a significant reduction in EMG activity for both the back and lower-limb muscles (*S1*, *S2*) or at least in one of two muscle groups (*S3*, *S4*). Moreover, the majority of participants (6 out of 8) demonstrated a consistent reduction in the EMG activity of at least one muscle group of the posterior chain. This indicates that when the exosuit provides knee extension torque, the back muscles require less effort to perform the lifting task. Among all muscle groups, the MF shows the greatest reduction in muscular effort, which plays a primary role in lifting tasks as it stabilizes the lower back. A reduction in the effort of the MF muscle group indicates the feasibility of reducing the risk of injury during a lifting task. While some subjects demonstrate an increase in the EMG activity of a few lower-limb muscles, the increase

is present in both the active and inactive cases, indicating that the increase in muscular effort most likely comes from the interaction of the exosuit interface and the human. In fact, the contact of the exosuit with the EMG sensors changes the interaction between the skin and the sensors (e.g. contact area) which could ultimately affect the quality of the measurements. The results from this study show a favorable human interaction to single-joint assistance and the benefit of reducing muscular activity with a soft exosuit, motivating the further development and testing of such soft wearable robots.

In a closed kinetic task, such as object lifting, the required energy will be constant regardless of whether the exosuit is active or inactive. When the exosuit is active, the additional energy supplied by the exosuit contributes to the total energy required for the task and thus the energy required by the human to finish the task is reduced. This study shows that humans can develop diverse but effective strategies to cooperate with exosuit assistance, resulting in an overall reduction of their muscular activities.

Despite the overall reduction in EMG activity with the soft robotic knee exosuit, the magnitude of this benefit varies across subjects. This could be attributed to the high compliance of the exosuit system and its interfacing with the soft tissues of the thigh. Also, another factor could be the high degree of freedom of the human musculoskeletal system that leaves the whole body's muscular response to each individual's different motor adaptation strategy. Moreover, the subjects were asked to determine the timing of inflation of the soft actuators, and this could contribute to inconsistent reductions in muscular activities. Modeling the contact forces between the exosuit and the human body could provide further insight into the transmission of assistive torques to the human body to accurately quantify the exosuit behavior.

4.7 Conclusions

In this paper, we studied the neuromuscular response to knee extension assistance during a lifting task with a novel soft-inflatable exosuit and eight healthy participants. The effects of knee assistance on the joint kinematics and muscle activity of the lower limbs and posterior chain muscles were investigated during squat lifting of weights equivalent to 10% of their bodyweight. Results demonstrated a statistically significant EMG reduction for the great majority of the lower-limb and back muscles, with the Multifidus (MF) showing the maximum average EMG reduction of 55%. Different neuromuscular adaptation mechanisms were observed among subjects that ultimately led to a favorable reduction in lower-limb or posterior chain muscle activity. This study provided early evidence that the soft inflatable exosuit could potentially reduce muscle effort by assisting knee extension during a squat lifting task.

Future work includes the development of a robust controller that detects the optimal timing for autonomous inflation and deflation of the exosuit using real-time wearable sensor data. A more comprehensive human study will be conducted, with a larger number of participants, different tasks to execute, and different control strategies for the exosuit. The exosuit will be expanded to other joints to provide more versatile assistance during different material-handling tasks.

Chapter 5

CONCLUSIONS

Wearable soft robots have successfully addressed inherent design limitations faced by wearable rigid robots. However, they possess a unique set of challenges due to their soft and compliant nature. Some of these challenges are present in the sensing, modeling, control and evaluation of wearable soft robots.

Some of the main challenges addressed in this dissertation are summarized in Fig. 5.1. Machine learning algorithms have shown promising results for sensor fusion with wearable robots, however, they require extensive data for training and retraining models for different users and experimental conditions. Modeling soft sensors and ac-

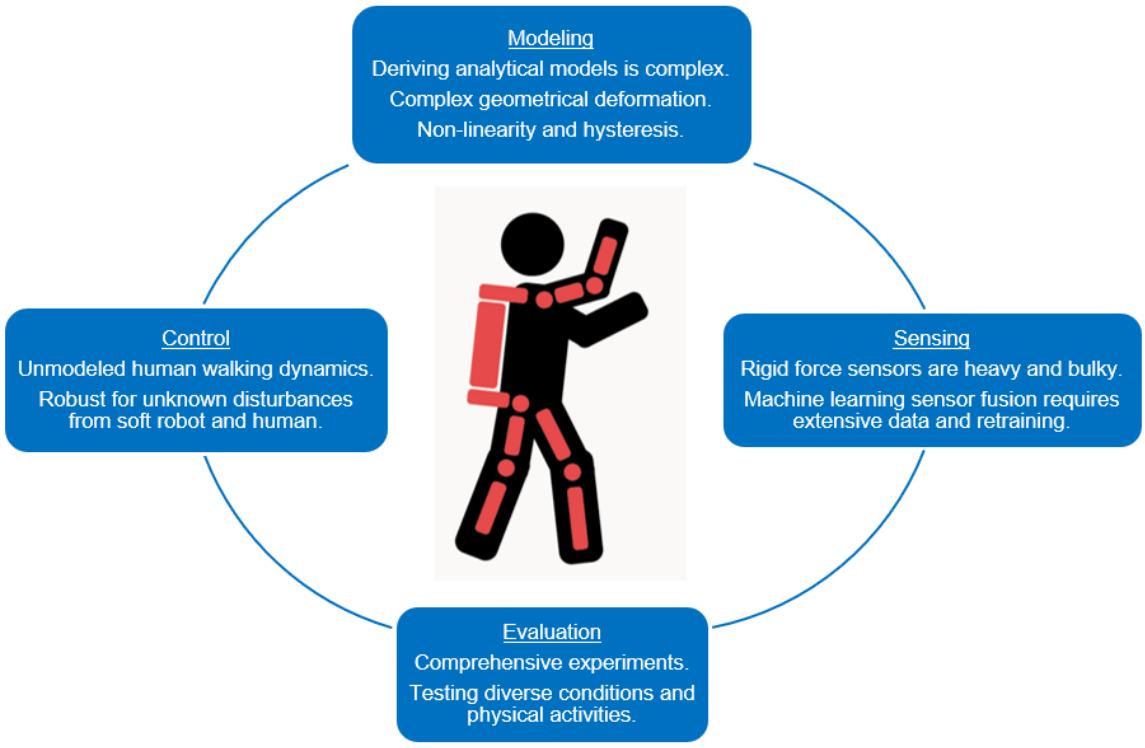

Figure 5.1. Challenges of Wearable Soft Robots.

tuators require characterizing non-linearity and hysteresis, which complicates deriving an analytical model. Experimental characterization can capture the characteristics of non-linearity and hysteresis but requires developing a synthesized model for real-time control. Controllers for wearable soft robots must be robust to compensate for unknown disturbances that arise from the soft robot and its interaction with the user. Since developing dynamic models for soft robots is complex, inaccuracies that arise from the unmodeled dynamics lead to significant disturbances that the controller needs to compensate for. In addition, obtaining a physical model of the human-robot interaction is complex due to unknown human dynamics during walking. Finally, the performance of soft robots for wearable applications requires extensive experimental evaluation to analyze the benefits for the user.

To address these challenges, this dissertation focuses on the sensing, modeling, and evaluation of soft robots for wearable applications. The main contributions of this dissertation are summarized in Fig. 5.2. Chapter 1 introduces an overview of the related works and current challenges in the field of wearable soft robots. Chapter 2 presents the design of a model-based sensor fusion algorithm to improve the estimation of human joint kinematics with a soft flexible robot that requires

Case Study	Modeling	Sensing	Control	Evaluation
Case Study #1: KCKF Sensor Fusion	Mechanical characterization: sensors	Model-based sensor fusion algorithm	x	Human Evaluation of: Joint Kinematics
Case Study #2: Gait Sensing and Haptic Feedback	Mechanical characterization: soft sensors and actuators	Design of soft lightweight sensors with haptic capabilities	Finite State Machine	Human Evaluation of: Gait sensing and haptic feedback
Case Study #3: Lifting with Exosuit	Mechanical characterization: soft actuators	x	User self selected control	Human Evaluation of: EMG (muscle activity) and kinematics

Figure 5.2. Contributions of the Dissertation.

compact and lightweight sensors. Kinematic state constraints were implemented into the sensor fusion algorithm to exploit the kinematic relationships between the robot and the user. To overcome limitations with rigid sensors, Chapter 3 presents the development of an inflatable soft haptic sensor to facilitate mutual gait sensing and haptic feedback. We employ mechanical characterization to address the challenge of developing models for soft sensors and actuators to quantify the external forces and the forces generated by the actuator. Finally, the benefits of soft robots for wearable applications were explored and discussed in Chapter 4 through the evaluation of a wearable soft exosuit. The results of the study demonstrate the benefits of the soft exosuit and its capacity to assist the lifting motion and reduce the human effort to accomplish such tasks. In addition, this study helped identify some challenges in the control and evaluation of soft robots in wearable applications, which will be the focus of future work, such as the development of a robust controller that detects the optimal timing for autonomous inflation and deflation of the exosuit while taking into account the inherent pressurization delays.

REFERENCES

Afzal, Muhammad Raheel, Sanghun Pyo, Min-Kyun Oh, Young Sook Park, Beom-Chan Lee, and Jungwon Yoon. 2016. "Haptic based gait rehabilitation system for stroke patients." In *2016 IEEE/RSJ Int. Conf. Intell. Robots Syst. (IROS),* 3198–3203.

Agarwal, Gunjan, Nicolas Besuchet, Basile Audergon, and Jamie Paik. 2016. "Stretchable Materials for Robust Soft Actuators towards Assistive Wearable Devices." *Sci Rep* 6, no. 1 (September): 34224.

Ahmad, Norhafizan, Raja Ariffin Raja Ghazilla, Nazirah M. Khairi, and Vijayabaskar Kasi. 2013. "Reviews on Various Inertial Measurement Unit (IMU) Sensor Applications." *Int. J. Signal Process. Syst.* 1 (2): 256–262. https://doi.org/10.12720/ijsps.1.2.256-262.

Alemi, Mohammad Mehdi, Jack Geissinger, Athulya A. Simon, S. Emily Chang, and Alan T. Asbeck. 2019. "A passive exoskeleton reduces peak and mean EMG during symmetric and asymmetric lifting." *J. Electromyogr. Kinesiol.* 47:25–34. https://doi.org/https://doi.org/10.1016/j.jelekin.2019.05.003.

Alouani, A.T., W.D. Blair, and G.A. Watson. 1991. "Bias and observability analysis of target tracking filters using a kinematic constraint." In *the 23rd Southeast. Symp. on Syst. Theory,* 229–232. IEEE Comput. Soc. Press. https://doi.org/10.1109/SSST.1991.138554.

Amin, Shreyasee, et al. 2008. "Occupation-related squatting, kneeling, and heavy lifting and the knee joint: a magnetic resonance imaging-based study in men." *J. Rheumatol.* 35 (8): 1645–1649.

Antwi-Afari, M.F., et al. 2017. "Biomechanical analysis of risk factors for work-related musculoskeletal disorders during repetitive lifting task in construction workers." *Autom. Constr.* 83:41–47. https://doi.org/https://doi.org/10.1016/j.autcon.2017.07.007.

Araromi, Oluwaseun A., Sam Castellanos, Conor J. Walsh, and Robert J. Wood. 2018. "Compliant Low Profile Multi-Axis Force Sensors." In *Proc IEEE ICRA,* 187–192. IEEE, May.

Araromi, Oluwaseun A., Conor J. Walsh, and Robert J. Wood. 2017. "Hybrid carbon fiber-textile compliant force sensors for high-load sensing in soft exosuits." In *Proc IEEE IROS,* vol. 2017-Septe, 1798–1803. IEEE, September.

Asbeck, Alan T, Stefano MM De Rossi, Kenneth G Holt, and Conor J Walsh. 2015. "A biologically inspired soft exosuit for walking assistance." *IJRR* 34 (6): 744–762.

Asbeck, Alan T., Stefano M.M. De Rossi, Ignacio Galiana, Ye Ding, and Conor J. Walsh. 2014. "Stronger, Smarter, Softer: Next-Generation Wearable Robots." *IEEE Robotics Automation Magazine* 21 (4): 22–33. https://doi.org/10.1109/MRA.2014.2360283.

El-Atab, Nazek, Rishabh B. Mishra, Fhad Al-Modaf, Lana Joharji, Aljohara A. Alsharif, Haneen Alamoudi, Marlon Diaz, Nadeem Qaiser, and Muhammad Mustafa Hussain. 2020. "Soft Actuators for Soft Robotic Applications: A Review." *Adv Intell Syst* 2, no. 10 (October): 2000128.

Atalay, Asli, Vanessa Sanchez, Ozgur Atalay, Daniel M. Vogt, Florian Haufe, Robert J. Wood, and Conor J. Walsh. 2017. "Batch Fabrication of Customizable Silicone-Textile Composite Capacitive Strain Sensors for Human Motion Tracking." *Adv Mater Technol* 2, no. 9 (September): 1700136.

Atalay, Ozgur, Asli Atalay, Joshua Gafford, and Conor Walsh. 2018. "A Highly Sensitive Capacitive-Based Soft Pressure Sensor Based on a Conductive Fabric and a Microporous Dielectric Layer." *Adv Mater Technol* 3, no. 1 (January): 1700237.

Atalay, Ozgur, Asli Atalay, Joshua Gafford, Hongqiang Wang, Robert Wood, and Conor Walsh. 2017. "A Highly Stretchable Capacitive-Based Strain Sensor Based on Metal Deposition and Laser Rastering." *Adv Mater Technol* 2, no. 9 (September): 1700081.

Awad, Louis N, Alberto Esquenazi, Gerard E Francisco, Karen J Nolan, and Arun Jayaraman. 2020. "The ReWalk ReStore™ soft robotic exosuit: a multi-site clinical trial of the safety, reliability, and feasibility of exosuit-augmented post-stroke gait rehabilitation." *J Neuroeng Rehabil* 17 (1): 1–11.

Awad, Louis N, Pawel Kudzia, Dheepak Arumukhom Revi, Terry D Ellis, and Conor J Walsh. 2020. "Walking faster and farther with a soft robotic exosuit: implications for post-stroke gait assistance and rehabilitation." *IEEE Open J Eng Med Biol* 1:108–115.

Balaban, Birol, and Fatih Tok. 2014. "Gait Disturbances in Patients With Stroke." *PM&R* 6 (7): 635–642.

Baltrusch, SJ, JH Van Dieën, CAM Van Bennekom, and H Houdijk. 2018. "The effect of a passive trunk exoskeleton on functional performance in healthy individuals." *Appl. Ergon.* 72:94–106.

Banerjee, Hritwick, Zion Tsz Ho Tse, and Hongliang Ren. 2018. "Soft robotics with compliance and adaptation for biomedical applications and forthcoming challenges." *Int J Robot Autom* 33, no. 1 (January): 69–80.

Bhattacharya, Anasua. 2014. "Costs of occupational musculoskeletal disorders (MSDs) in the United States." *Int. J. Ind. Ergon.* 44 (3): 448–454.

Cao, Wujing, Chunjie Chen, Hongyue Hu, Kai Fang, and Xinyu Wu. 2020. "Effect of hip assistance modes on metabolic cost of walking with a soft exoskeleton." *IEEE Trans Autom Sci Eng.*

Channa, Asma, Nirvana Popescu, and Vlad Ciobanu. 2020. "Wearable Solutions for Patients with Parkinson's Disease and Neurocognitive Disorder: A Systematic Review." *Sensors* 20, no. 9 (May): 2713.

Chen, Bing, Hao Ma, Lai-Yin Qin, Fei Gao, Kai-Ming Chan, Sheung-Wai Law, Ling Qin, and Wei-Hsin Liao. 2016. "Recent developments and challenges of lower extremity exoskeletons." *J Orthop Translat* 5 (April): 26–37.

Chen, Daniel K.Y., Markus Haller, and Thor F. Besier. 2017. "Wearable lower limb haptic feedback device for retraining Foot Progression Angle and Step Width." *Gait & Posture* 55:177–183.

Chen, Jun-Liang, Yan-Ning Dai, Nicolas S. Grimaldi, Jing-Jing Lin, Bo-Yi Hu, Yin-Feng Wu, and Shuo Gao. 2022. "Plantar Pressure-Based Insole Gait Monitoring Techniques for Diseases Monitoring and Analysis: A Review." *Adv. Mater. Technol.* 7 (1): 2100566.

Chen, Yang, Shaofei Guo, Cunfeng Li, Hui Yang, and Lina Hao. 2018. "Size recognition and adaptive grasping using an integration of actuating and sensing soft pneumatic gripper." *Robot. Auton. Syst.* 104:14–24.

Chen, Zhiyong, Ronghui Wu, Shihui Guo, Xiangyang Liu, Hongbo Fu, Xiaogang Jin, and Minghong Liao. 2020. "3D Upper Body Reconstruction with Sparse Soft Sensors." *Soft Robotics* (July): soro.2019.0187.

Chiaradia, Domenico, Michele Xiloyannis, Massimiliano Solazzi, Lorenzo Masia, and Antonio Frisoli. 2018. "Comparison of a soft exosuit and a rigid exoskeleton in an assistive task." In *WeRob,* 415–419. Springer.

Choi, Hyunjin, and Kyoungchul Kong. 2019. "A Soft Three-Axis Force Sensor Based on Radially Symmetric Pneumatic Chambers." *IEEE Sens J* 19, no. 13 (July): 5229–5238.

Chossat, Jean-Baptiste, Yong-Lae Park, Robert J. Wood, and Vincent Duchaine. 2013. "A Soft Strain Sensor Based on Ionic and Metal Liquids." *IEEE Sens J* 13, no. 9 (September): 3405–3414.

Chossat, Jean-Baptiste, Yiwei Tao, Vincent Duchaine, and Yong-Lae Park. 2015. "Wearable soft artificial skin for hand motion detection with embedded microfluidic strain sensing." In *Proc IEEE ICRA,* 2568–2573. IEEE, May.

Cirstea, Carmen M. 2019. "Are Wearable Robots Effective for Gait Recovery After Stroke?" *Stroke* 50, no. 12 (December): 3337–3338.

Ciullo, Andrea S, Janne M Veerbeek, Eveline Temperli, Andreas R Luft, Frederik J Tonis, Claudia JW Haarman, Arash Ajoudani, Manuel G Catalano, Jeremia PO Held, and Antonio Bicchi. 2020. "A novel soft robotic supernumerary hand for severely affected stroke patients." *IEEE Trans Neural Syst Rehabil Eng* 28 (5): 1168–1177.

Della Santina, Cosimo, Christian Duriez, and Daniela Rus. 2023. "Model-Based Control of Soft Robots: A Survey of the State of the Art and Open Challenges." *IEEE Control Systems Magazine* 43 (3): 30–65. https://doi.org/10.1109/MCS.2023.3253419.

Ding, Ye, Ignacio Galiana, Christopher Siviy, Fausto A Panizzolo, and Conor Walsh. 2016. "IMU-based iterative control for hip extension assistance with a soft exosuit." In *Proc IEEE ICRA,* 3501–3508.

Elevate Ski, Roam Robotics. https://www.roamrobotics.com/elevate.

Esquenazi, Alberto, Mukul Talaty, Andrew Packel, and Michael Saulino. 2012. "The ReWalk Powered Exoskeleton to Restore Ambulatory Function to Individuals with Thoracic-Level Motor-Complete Spinal Cord Injury." *Am. J. Phys. Med. Rehabil.* 91 (11): 911–921. https://doi.org/10.1097/PHM.0b013e318269d9a3.

Al-Fahaam, Hassanin, Steve Davis, Samia Nefti-Meziani, and Theo Theodoridis. 2018. "Novel soft bending actuator-based power augmentation hand exoskeleton controlled by human intention." *Intell Serv Robot* 11 (3): 247–268.

Filippeschi, Alessandro, Norbert Schmitz, Markus Miezal, Gabriele Bleser, Emanuele Ruffaldi, and Didier Stricker. 2017. "Survey of Motion Tracking Methods Based

on Inertial Sensors: A Focus on Upper Limb Human Motion." *Sensors* 17 (6): 1257. https://doi.org/10.3390/s17061257.

Frisoli, Antonio. 2019. "Wearable Robots." In *Encyclopedia of Robotics,* edited by Marcelo H Ang, Oussama Khatib, and Bruno Siciliano, 1–8. Berlin, Heidelberg: Springer.

Frutiger, Andreas, Joseph T. Muth, Daniel M. Vogt, Yiğit Mengüç, Alexandre Campo, Alexander D. Valentine, Conor J. Walsh, and Jennifer A. Lewis. 2015. "Capacitive Soft Strain Sensors via Multicore-Shell Fiber Printing." *Adv Mater* 27, no. 15 (April): 2440–2446.

González, Iván, Jesús Fontecha, Ramón Hervás, and José Bravo. 2015. "An Ambulatory System for Gait Monitoring Based on Wireless Sensorized Insoles." *Sensors* 15, no. 7 (July): 16589–16613.

Graven-Nielsen, Thomas, Siegfried Mense, and Lars Arendt-Nielsen. 2004. "Painful and non-painful pressure sensations from human skeletal muscle." *Exp. Brain Res.* 159, no. 3 (December): 273–283. https://doi.org/10.1007/s00221-004-1937-7.

Greff, Klaus, Rupesh K. Srivastava, Jan Koutnik, Bas R. Steunebrink, and Jurgen Schmidhuber. 2017. "LSTM: A Search Space Odyssey." *IEEE Trans Neural Networks Learn Syst* 28, no. 10 (October): 2222–2232.

Gurari, Netta, Kathryn Smith, Manu Madhav, and Allison M. Okamura. 2009. "Environment discrimination with vibration feedback to the foot, arm, and fingertip." In *2009 IEEE Int. Conf. Rehabil. Robot.* 343–348.

Harnett, Cindy K., Huichan Zhao, and Robert F. Shepherd. 2017. "Stretchable Optical Fibers: Threads for Strain-Sensitive Textiles." *Adv Mater Technol* 2, no. 9 (September): 1700087.

Heikenfeld, J., A. Jajack, J. Rogers, P. Gutruf, L. Tian, T. Pan, R. Li, et al. 2018. "Wearable sensors: modalities, challenges, and prospects." *Lab on a Chip* 18, no. 2 (January): 217–248.

HeroWear. https://herowearexo.com/.

Holleczek, Thomas, Alex Ru, Holger Harms, and Gerhard Tro. 2010. "Textile pressure sensors for sports applications." In *2010 IEEE Sensors,* 732–737. IEEE, November.

Hubertsson, Jenny, et al. 2014. "Sick leave patterns in common musculoskeletal disorders–a study of doctor prescribed sick leave." *BMC Musculoskelet. Disord.* 15 (1): 1–9.

Hussain, Irfan, Leonardo Meli, Claudio Pacchierotti, and Domenico Prattichizzo. 2017. "A soft robotic supernumerary finger and a wearable cutaneous finger interface to compensate the missing grasping capabilities in chronic stroke patients." In *Proc World Haptics Conference,* 183–188.

Hussain, Irfan, Giovanni Spagnoletti, Gionata Salvietti, and Domenico Prattichizzo. 2016. "An EMG interface for the control of motion and compliance of a supernumerary robotic finger." *Front Neurorobot* 10:18.

Hwang, Seonhong, Youngeun Kim, and Youngho Kim. 2009. "Lower extremity joint kinetics and lumbar curvature during squat and stoop lifting." *BMC Musculoskeletal Disorders* 10, no. 1 (December): 15. https://doi.org/10.1186/1471-2474-10-15.

Jeon, Soo, Masayoshi Tomizuka, and Tetsuaki Katou. 2009. "Kinematic Kalman Filter (KKF) for Robot End-Effector Sensing." *J. Dyn. Syst. Meas. Contr.* 131 (2): 1–8. https://doi.org/10.1115/1.3023124.

Jeong, Mingoo, Hanseung Woo, and Kyoungchul Kong. 2020. "A study on weight support and balance control method for assisting squat movement with a wearable robot, angel-suit." *Int. J. Control. Autom. Syst.* 18 (1): 114–123.

Jin, Yichu, Christina M. Glover, Haedo Cho, Oluwaseun A. Araromi, Moritz A. Graule, Na Li, Robert J. Wood, and Conor J. Walsh. 2020. "Soft Sensing Shirt for Shoulder Kinematics Estimation," 4863–4869. IEEE, May. https://doi.org/10.1109/ICRA40945.2020.9196586.

Kanjanapas, Smita, Cara M. Nunez, Sophia R. Williams, Allison M. Okamura, and Ming Luo. 2019. "Design and analysis of pneumatic 2-DoF soft haptic devices for shear display." *IEEE RA-L* 4 (2): 1365–1371.

Kim, DongWook, Junghan Kwon, Byungjun Jeon, and Yong-Lae Park. 2020. "Adaptive Calibration of Soft Sensors Using Optimal Transportation Transfer Learning for Mass Production and Long-Term Usage." *Adv Intell Syst* 2, no. 6 (June): 1900178.

Kim, Dooyoung, Min Kim, Junghan Kwon, Yong-Lae Park, and Sungho Jo. 2019. "Semi-Supervised Gait Generation With Two Microfluidic Soft Sensors." *IEEE RA-L* 4, no. 3 (July): 2501–2507.

Kim, Dooyoung, Junghan Kwon, Seunghyun Han, Yong-Lae Park, and Sungho Jo. 2019. "Deep Full-Body Motion Network for a Soft Wearable Motion Sensing Suit." *IEEE ASME Trans Mechatron* 24, no. 1 (February): 56–66.

Kim, Kanghyun, Sungwon Shin, and Kyoungchul Kong. 2018. "An Air-Filled Pad With Elastomeric Pillar Array Designed for a Force-Sensing Insole." *IEEE Sens J* 18, no. 10 (May): 3968–3976.

Kim, Taekyoung, Sudong Lee, Taehwa Hong, Gyowook Shin, Taehwan Kim, and Yong-Lae Park. 2020. "Heterogeneous sensing in a multifunctional soft sensor for human-robot interfaces." *Sci Robot* 5, no. 49 (December): eabc6878.

Kim, Wansoo, Pietro Balatti, Edoardo Lamon, and Arash Ajoudani. 2020. "MOCA-MAN: A MObile and reconfigurable Collaborative Robot Assistant for conjoined huMAN-robot actions." In *Proc IEEE ICRA,* 10191–10197.

Koizumi, Shoichiro, Te-Hsin Chang, Hiroyuki Nabae, Gen Endo, Koichi Suzumori, Motoki Mita, Kimio Saitoh, Kazutoshi Hatakeyama, Satoaki Chida, and Yoichi Shimada. 2020. "Soft Robotic Gloves with Thin McKibben Muscles for Hand Assist and Rehabilitation." In *Proc IEEE/SICE SII,* 93–98.

Kong, Kyoungchul, and Masayoshi Tomizuka. 2009. "A gait monitoring system based on air pressure sensors embedded in a shoe." *IEEE/ASME Trans. Mechatron.* 14 (3): 358–370.

Kramer, R. K., C. Majidi, R. Sahai, and R. J. Wood. 2011. "Soft curvature sensors for joint angle proprioception." In *Proc IEEE IROS,* 1919–1926. IEEE, September.

Kubota, Shigeki, Yoshio Nakata, Kiyoshi Eguchi, Hiroaki Kawamoto, Kiyotaka Kamibayashi, Masataka Sakane, Yoshiyuki Sankai, and Naoyuki Ochiai. 2013. "Feasibility of rehabilitation training with a newly developed wearable robot for patients with limited mobility." *Arch Phys Med Rehabil* 94 (6): 1080–1087.

Kyoungchul Kong and Masayoshi Tomizuka. 2009. "A Gait Monitoring System Based on Air Pressure Sensors Embedded in a Shoe." *IEEE ASME Trans Mechatron* 14, no. 3 (June): 358–370.

Lamers, Erik P, Aaron J Yang, and Karl E Zelik. 2017. "Feasibility of a biomechanically-assistive garment to reduce low back loading during leaning and lifting." *IEEE Trans. Biomed. Eng.* 65 (8): 1674–1680.

Leal-Junior, Arnaldo G., Anselmo Frizera, Laura Vargas-Valencia, Wilian M. dos Santos, Antonio P. L. Bo, Adriano A. G. Siqueira, and Maria Jose Pontes. 2018.

"Polymer Optical Fiber Sensors in Wearable Devices: Toward Novel Instrumentation Approaches for Gait Assistance Devices." *IEEE Sens J* 18, no. 17 (September): 7085–7092.

Leal-Junior, Arnaldo G., Laura Vargas-Valencia, Wilian M. dos Santos, Felipe B.A. Schneider, Adriano A.G. Siqueira, Maria José Pontes, and Anselmo Frizera. 2018. "POF-IMU sensor system: A fusion between inertial measurement units and POF sensors for low-cost and highly reliable systems." *Opt Fiber Technol* 43 (July): 82–89.

Lee, Chiwon, Myungjoon Kim, Yoon Jae Kim, Nhayoung Hong, Seungwan Ryu, H. Jin Kim, and Sungwan Kim. 2017. "Soft robot review." *Int J Control Autom Syst* 15, no. 1 (February): 3–15.

Lee, Jung Keun, and Mi Jin Choi. 2019. "Robust Inertial Measurement Unit-Based Attitude Determination Kalman Filter for Kinematically Constrained Links." *Sensors* 19 (4): 768. https://doi.org/10.3390/s19040768.

Li, Dongting, Emiliano Quinones Yumbla, Alyssa Olivas, Thomas Sugar, Heni Ben Amor, Hyunglae Lee, Wenlong Zhang, and Daniel M. Aukes. 2023. "Origami-Inspired Wearable Robot for Trunk Support." *IEEE/ASME Transactions on Mechatronics* 28 (3): 1466–1476. https://doi.org/10.1109/TMECH.2022.3220136.

Li, Yi, and Minoru Hashimoto. 2017. "PVC gel soft actuator-based wearable assist wear for hip joint support during walking." *Smart Mater Struct* 26 (12): 125003.

Liu, Shanliangzi, Dylan S. Shah, and Rebecca Kramer-Bottiglio. 2021. "Highly stretchable multilayer electronic circuits using biphasic gallium-indium." *Nat Mater* (February).

Lu, Sitong, Diansheng Chen, Che Liu, Yongkang Jiang, and Min Wang. 2019. "A 3-D finger motion measurement system via soft strain sensors for hand rehabilitation." *Sens Actuator A Phys* 285:700–711.

Lurie, Kristen L., Pete B. Shull, Karen F. Nesbitt, and Mark R. Cutkosky. 2011. "Informing haptic feedback design for gait retraining." In *2011 IEEE World Haptics Conf.* 19–24.

Majidi, C., R. Kramer, and R. J. Wood. 2011. "A non-differential elastomer curvature sensor for softer-than-skin electronics." *Smart Mater Struct* 20, no. 10 (October): 105017.

Masia, Lorenzo, Irfan Hussain, Michele Xiloyannis, Claudio Pacchierotti, Leonardo Cappello, Monica Malvezzi, Giovanni Spagnoletti, et al. 2018. "Soft wearable assistive robotics: exosuits and supernumerary limbs." In *Wearable Exoskeleton Systems: Design, control and applications,* 219–254. Institution of Engineering / Technology.

Maurice, Pauline, et al. 2019. "Evaluation of PAEXO, a novel passive exoskeleton for overhead work." *Comput. Methods Biomech. Biomed. Engin.* 22 (sup1): S448–S450.

Mishra, Vigyanshu, and Asimina Kiourti. 2019. "Wrap-Around Wearable Coils for Seamless Monitoring of Joint Flexion." *IEEE Transactions on Biomedical Engineering* 66 (10): 2753–2760. https://doi.org/10.1109/TBME.2019.2895293.

Mohammed, Samer, Allou Samé, Latifa Oukhellou, Kyoungchul Kong, Weiguang Huo, and Yacine Amirat. 2016. "Recognition of gait cycle phases using wearable sensors." *Rob Auton Syst* 75 (January): 50–59.

Mohri, Shun, et al. 2016. "Development of endoskeleton type knee auxiliary power assist suit using pneumatic artificial muscles." In *2016 IEEE Int. Conf. Adv. Intell. Mechatron. (AIM),* 107–112. IEEE.

Navarro, Stefan Escaida, Olivier Goury, Gang Zheng, Thor Morales Bieze, and Christian Duriez. 2019. "Modeling Novel Soft Mechanosensors based on Air-Flow Measurements." *IEEE Robot. Autom. Lett.* 4 (4): 4338–4345.

Nesler, Christopher R, Tim A Swift, and Elliott J Rouse. 2018. "Initial design and experimental evaluation of a pneumatic interference actuator." *Soft Robotics* 5 (2): 138–148.

Nguyen, Pham H, IB Imran Mohd, Curtis Sparks, Francisco L Arellano, Wenlong Zhang, and Panagiotis Polygerinos. 2019. "Fabric soft poly-limbs for physical assistance of daily living tasks." In *Proc IEEE ICRA,* 8429–8435.

Nguyen, Pham H, Saivimal Sridar, Sunny Amatya, Carly M Thalman, and Panagiotis Polygerinos. 2019. "Fabric-Based Soft Grippers Capable of Selective Distributed Bending for Assistance of Daily Living Tasks." In *2019 2nd IEEE International Conference on Soft Robotics (RoboSoft),* 404–409. IEEE.

Nguyen, Pham Huy, and Wenlong Zhang. 2020. "Design and Computational Modeling of Fabric Soft Pneumatic Actuators for Wearable Assistive Devices." *Sci Rep,* 1–13.

O'Neill, Ciarán T., Connor M. McCann, Cameron J. Hohimer, Katia Bertoldi, and Conor J. Walsh. 2022. "Unfolding Textile-Based Pneumatic Actuators for Wearable Applications." *Soft Robotics* 9 (1): 163–172. https://doi.org/10.1089/soro.2020.0064.

Pang, Gaoyang, Geng Yang, Wenzheng Heng, Zhiqiu Ye, Xiaoyan Huang, Hua-Yong Yang, and Zhibo Pang. 2020. "CoboSkin: Soft robot skin with variable stiffness for safer human–robot collaboration." *IEEE Trans Ind Electron* 68 (4): 3303–3314.

Park, Myungsun, Bomin Jeong, and Yong-Lae Park. 2021. "Hybrid System Analysis and Control of a Soft Robotic Gripper with Embedded Proprioceptive Sensing for Enhanced Gripping Performance." *Adv Intell Syst,* 2000061.

Park, Yong-Lae, Carmel Majidi, Rebecca Kramer, Phillipe Bérard, and Robert J. Wood. 2010. "Hyperelastic pressure sensing with a liquid-embedded elastomer." *J Micromech Microeng* 20, no. 12 (December): 125029.

Pollard, JP, LP Le Quesne, and JW Tappin. 1983. "Forces under the foot." *J. Biomed. Eng.* 5 (1): 37–40.

Ponraj, Godwin, and Hongliang Ren. 2018. "Sensor Fusion of Leap Motion Controller and Flex Sensors Using Kalman Filter for Human Finger Tracking." *IEEE Sens. J.* 18 (5): 2042–2049. https://doi.org/10.1109/JSEN.2018.2790801.

Pons, José L. 2008. *Wearable robots: biomechatronic exoskeletons.* John Wiley & Sons.

Prado, Antonio, Xiya Cao, Xiangzhuo Ding, and Sunil K. Agrawal. 2020. "Prediction of Gait Cycle Percentage Using Instrumented Shoes with Artificial Neural Networks." In *Proc IEEE ICRA,* 2834–2840. Institute of Electrical / Electronics Engineers Inc., May.

Qiu, Ye, Ye Tian, Shenshen Sun, Jiahui Hu, Youyan Wang, Zheng Zhang, Aiping Liu, et al. 2020. "Bioinspired, multifunctional dual-mode pressure sensors as electronic skin for decoding complex loading processes and human motions." *Nano Energy* 78 (December): 105337.

ReStore, ReWalk Robotics. https://rewalk.com/restore-exo-suit/.

Roam Robotics. https://www.roamrobotics.com/.

Roozbazar, A. 1974. "Biomechanics of lifting." In *Biomechanics IV,* 37–43. Springer.

Roveda, Loris, Luca Savani, Sara Arlati, Tito Dinon, Giovanni Legnani, and Lorenzo Molinari Tosatti. 2020. "Design methodology of an active back-support exoskeleton

with adaptable backbone-based kinematics." *Int. J. Ind. Ergon.* 79:102991. https://doi.org/https://doi.org/10.1016/j.ergon.2020.102991.

Russo, Stefania, Tommaso Ranzani, Hongbin Liu, Samia Nefti-Meziani, Kaspar Althoefer, and Arianna Menciassi. 2015. "Soft and Stretchable Sensor Using Biocompatible Electrodes and Liquid for Medical Applications." *Soft Robotics* 2, no. 4 (December): 146–154.

Sabri, Naseer, S. A. Aljunid, M. S. Salim, and S. Fouad. 2015. "Fiber Optic Sensors: Short Review and Applications." In *Springer Series in Materials Science,* 204:299–311. Springer Verlag.

Sado, Fatai, Hwa Jen Yap, Raja Ariffin Raja Ghazilla, and Norhafizan Ahmad. 2019. "Design and control of a wearable lower-body exoskeleton for squatting and walking assistance in manual handling works." *Mechatronics* 63:102272.

Saggio, Giovanni, Francesco Riillo, Laura Sbernini, and Lucia Rita Quitadamo. 2016. "Resistive flex sensors: a survey." *Smart Mater Struct* 25, no. 1 (January): 013001.

Shull, Pete B., Kristen L. Lurie, Mark R. Cutkosky, and Thor F. Besier. 2011. "Training multi-parameter gaits to reduce the knee adduction moment with data-driven models and haptic feedback." *J. Biomech.* 44 (8): 1605–1609.

Siviy, Christopher, Jaehyun Bae, Lauren Baker, Franchino Porciuncula, Teresa Baker, Terry D Ellis, Louis N Awad, and Conor James Walsh. 2020. "Offline assistance optimization of a soft exosuit for augmenting ankle power of stroke survivors during walking." *IEEE RA-L* 5 (2): 828–835.

Song, Jiyuan, Aibin Zhu, Yao Tu, and Jiajun Zou. 2021. "Multijoint passive elastic spine exoskeleton for stoop lifting assistance." *Int. J. Adv. Robot. Syst.* 18 (6). https://doi.org/10.1177/17298814211062033.

Souri, Hamid, Hritwick Banerjee, Ardian Jusufi, Norbert Radacsi, Adam A. Stokes, Inkyu Park, Metin Sitti, and Morteza Amjadi. 2020. "Wearable and Stretchable Strain Sensors: Materials, Sensing Mechanisms, and Applications." *Adv Intell Syst.* 2, no. 8 (August): 2000039.

Southall, B, B F Buxton, and J A Marchant. 1998. "Controllability and Observability: Tools for Kalman Filter Design." In *Proc. BMVC,* 17.1–17.10. BMVA Press.

Sridar, S., et al. 2020. "Evaluating Immediate Benefits of Assisting Knee Extension With a Soft Inflatable Exosuit." *IEEE Trans. Med. Robot. Bionics* 2 (2): 216–225. https://doi.org/10.1109/TMRB.2020.2988305.

Sridar, Saivimal, Zhi Qiao, Niveditha Muthukrishnan, Wenlong Zhang, and Panagiotis Polygerinos. 2018. "A soft-inflatable exosuit for knee rehabilitation: Assisting swing phase during walking." *Front. Robot. AI* 5:44.

Sun, Xu, Samuel M. Felton, Robert J. Wood, and Sangbae Kim. 2015. "Printing angle sensors for foldable robots." In *Proc IEEE IROS,* vol. 2015-Decem, 1725–1731. IEEE, September.

Tang, Zhi Qiang, Ho Lam Heung, Kai Yu Tong, and Zheng Li. 2019. "Model-based online learning and adaptive control for a "human-wearable soft robot" integrated system." *IJRR,* 0278364919873379.

Tavassolian, Mohammad, Tyler J. Cuthbert, Christopher Napier, JingYang Peng, and Carlo Menon. 2020. "Textile-Based Inductive Soft Strain Sensors for Fast Frequency Movement and Their Application in Wearable Devices Measuring Multiaxial Hip Joint Angles during Running." *Adv Intell Syst* 2, no. 4 (April): 1900165.

Thalman, Carly, and Panagiotis Artemiadis. 2020. "A review of soft wearable robots that provide active assistance: Trends, common actuation methods, fabrication, and applications." *Wearable Technol* 1 (September): e3.

Theurel, Jean, and Kevin Desbrosses. 2019. "Occupational Exoskeletons: Overview of Their Benefits and Limitations in Preventing Work-Related Musculoskeletal Disorders." *IISE Trans Occup Ergon Hum Factors* 7, nos. 3-4 (October): 264–280.

Theurel, Jean, Kevin Desbrosses, Terence Roux, and Adriana Savescu. 2018. "Physiological consequences of using an upper limb exoskeleton during manual handling tasks." *Applied ergonomics* 67:211–217.

Tiboni, Monica, Alberto Borboni, Fabien Vérité, Chiara Bregoli, and Cinzia Amici. 2022. "Sensors and Actuation Technologies in Exoskeletons: A Review." *Sensors* 22 (3). https://doi.org/10.3390/s22030884.

To, Celeste, Tess Hellebrekers, Jaewoong Jung, Sohee John Yoon, and Yong-Lae Park. 2018. "A Soft Optical Waveguide Coupled With Fiber Optics for Dynamic Pressure and Strain Sensing." *IEEE RA-L* 3, no. 4 (October): 3821–3827.

Tognetti, Alessandro, Federico Lorussi, Nicola Carbonaro, and Danilo de Rossi. 2015. "Wearable Goniometer and Accelerometer Sensory Fusion for Knee Joint Angle Measurement in Daily Life." *Sensors* 15, no. 11 (November): 28435–28455.

Toxiri, Stefano, et al. 2019. "Back-support exoskeletons for occupational use: an overview of technological advances and trends." *IISE Trans. Occup. Ergon. Hum. Factors* 7 (3-4): 237–249.

Tsukahara, Atsushi, Ryota Kawanishi, Yasuhisa Hasegawa, and Yoshiyuki Sankai. 2010. "Sit-to-Stand and Stand-to-Sit Transfer Support for Complete Paraplegic Patients with Robot Suit HAL." *Adv. Robot.* 24 (11): 1615–1638. https://doi.org/10.1163/016918610X512622.

Vakos, JP, AJ Nitz, AJ Threlkeld, R Shapiro, and T Horn. 1994. "Electromyographic activity of selected trunk and hip muscles during a squat lift. Effect of varying the lumbar posture." *Spine* 19 (6): 687–695.

Van Meerbeek, I. M., C. M. De Sa, and R. F. Shepherd. 2018. "Soft optoelectronic sensory foams with proprioception." *Sci Robot* 3, no. 24 (November): eaau2489.

Vargas-Valencia, Laura Susana, Felipe B. A. Schneider, Arnaldo G. Leal-Junior, Pablo Caicedo-Rodriguez, Wilson A. Sierra-Arevalo, Luis E. Rodriguez-Cheu, Teodiano Bastos-Filho, and Anselmo Frizera-Neto. 2021. "Sleeve for Knee Angle Monitoring: An IMU-POF Sensor Fusion System." *IEEE J. Biomed. Health Inform.* 25 (2): 465–474. https://doi.org/10.1109/JBHI.2020.2988360.

Vogt, Daniel M., Yong-Lae Park, and Robert J. Wood. 2013. "Design and Characterization of a Soft Multi-Axis Force Sensor Using Embedded Microfluidic Channels." *IEEE Sens J* 13, no. 10 (October): 4056–4064.

Wittmann, Frieder, Olivier Lambercy, and Roger Gassert. 2019. "Magnetometer-Based Drift Correction During Rest in IMU Arm Motion Tracking." *Sensors* 19 (6). https://doi.org/10.3390/s19061312.

Xavier, Matheus S., Charbel D. Tawk, Ali Zolfagharian, Joshua Pinskier, David Howard, Taylor Young, Jiewen Lai, et al. 2022. "Soft Pneumatic Actuators: A Review of Design, Fabrication, Modeling, Sensing, Control and Applications." *IEEE Access* 10:59442–59485. https://doi.org/10.1109/ACCESS.2022.3179589.

Xu, Cheng, Jie He, Xiaotong Zhang, Cui Yao, and Po-Hsuan Tseng. 2018. "Geometrical kinematic modeling on human motion using method of multi-sensor fusion." *Inf. Fusion* 41:243–254. https://doi.org/10.1016/j.inffus.2017.09.014.

Yang, Hui, Yang Chen, Yao Sun, and Lina Hao. 2017. "A novel pneumatic soft sensor for measuring contact force and curvature of a soft gripper." *Sens. Actuators A: Phys.* 266:318–327.

Yang, Jiantao, and Yuehong Yin. 2021. "Novel Soft Smart Shoes for Motion Intent Learning of Lower Limbs Using LSTM with a Convolutional Autoencoder." *IEEE Sens J* 21, no. 2 (January): 1906–1917.

Yang, Xiaolong, Tzu-Hao Huang, Hang Hu, Shuangyue Yu, Sainan Zhang, Xianlian Zhou, Alessandra Carriero, Guang Yue, and Hao Su. 2019. "Spine-inspired continuum soft exoskeleton for stoop lifting assistance." *IEEE RA-L* 4 (4): 4547–4554. https://doi.org/10.1109/LRA.2019.2935351.

Yao, Z., C. Linnenberg, R. Weidner, and J. Wulfsberg. 2019. "Development of A Soft Power Suit for Lower Back Assistance*." In *2019 IEEE Int. Conf. Robot. Autom. (ICRA),* 5103–5109. https://doi.org/10.1109/ICRA.2019.8794026.

Yong-Lae Park, Bor-Rong Chen, and Robert J. Wood. 2012. "Design and Fabrication of Soft Artificial Skin Using Embedded Microchannels and Liquid Conductors." *IEEE Sens J* 12, no. 8 (August): 2711–2718.

Yu, S., et al. 2019. "Design and Control of a High-Torque and Highly Backdrivable Hybrid Soft Exoskeleton for Knee Injury Prevention During Squatting." *IEEE Robot. Autom. Lett.* 4 (4): 4579–4586. https://doi.org/10.1109/LRA.2019.2931427.

Yu, Shuangyue, Tzu-Hao Huang, Dianpeng Wang, Brian Lynn, Dina Sayd, Viktor Silivanov, Young Soo Park, Yingli Tian, and Hao Su. 2019. "Design and control of a high-torque and highly backdrivable hybrid soft exoskeleton for knee injury prevention during squatting." *IEEE RA-L* 4 (4): 4579–4586.

Yumbla, Emiliano Quinones, Zhi Qiao, Weijia Tao, and Wenlong Zhang. 2021. "Human Assistance and Augmentation with Wearable Soft Robotics: a Literature Review and Perspectives." *Curr. Robot. Rep.* 2 (December): 399–413. https://doi.org/10.1007/s43154-021-00067-0.

Yumbla, Francisco, Wendy Yumbla, Emiliano Quiñones Yumbla, and Hyungpil Moon. 2022. "OobSoft Gripper: A Reconfigurable Soft Gripper Using Oobleck for Versatile and Delicate Grasping." In *2022 IEEE 5th Int. Conf. on Soft Robot. (RoboSoft),* 512–517. https://doi.org/10.1109/RoboSoft54090.2022.9762097.

Zanotto, Damiano, Yasuhiro Akiyama, Paul Stegall, and Sunil K. Agrawal. 2015. "Knee Joint Misalignment in Exoskeletons for the Lower Extremities: Effects on User's Gait." *IEEE Trans Robot* 31, no. 4 (August): 978–987.

Zhou, Yu Meng, Diana Wagner, Kristin Nuckols, Roman Heimgartner, Carolina Correia, Megan Clarke, Dorothy Orzel, Ciarán O'Neill, Ryan Solinsky, Sabrina

Paganoni, et al. 2019. “Soft robotic glove with integrated sensing for intuitive grasping assistance post spinal cord injury.” In *Proc IEEE ICRA,* 9059–9065.

Zoss, A.B., H. Kazerooni, and A. Chu. 2006. “Biomechanical design of the Berkeley lower extremity exoskeleton (BLEEX).” *IEEE/ASME Trans. Mechatron.* 11 (2): 128–138. https://doi.org/10.1109/TMECH.2006.871087.

APPENDIX A

STATEMENT FOR AUTHORSHIP

This is to certify that all co-authors have granted their permission to include the collaborative works in this dissertation.